LEIBNIZ –INFORMATIONSZENTRUM
TECHNIK UND NATURWISSENSCHAFTEN
UNIVERSITÄTSBIBLIOTHEK

Development of hybrid optical simulation concepts for polymer waveguides

Von der Fakultät für Mathematik und Physik
der Gottfried Wilhelm Leibniz Universität Hannover

zur Erlangung des akademischen Grades
Doktorin der Naturwissenschaften
Dr. rer. nat.

genehmigte Dissertation von

M.Sc. Monali Suar

2021

Referent: Prof. Dr. Bernhard Roth
Hannoversches Zentrum für optische Technologien,
Gottfried Wilhelm Leibniz Universität Hannover

Ko-Referent: Prof. Dr. Dag Heinemann
Institut für Gartenbauliche Produktionssysteme (IPGS)/
Hannoversches Zentrum für optische Technologien,
Gottfried Wilhelm Leibniz Universität Hannover

Ko-Referent: Prof. Dr. - Ing. Maik Rahlves
Institut für Biomedizinische Optik,
Universität zu Lübeck

Tag der Promotion : 16 July 2021

Declaration

All sentences or passages quoted in this document from other people's work have been specifically acknowledged by clear cross-referencing to author, work and page(s). Any illustrations that are not the work of the author of this report have been used with the explicit permission of the originator and are specifically acknowledged. I understand that failure to do this amounts to plagiarism and will be considered grounds for failure.

Name: _____

Signature: _____

Date: _____

Acknowledgement

I would like to thank my first supervisor Prof. Bernhard Roth for the feedback, guidance and support, he provided during this research. His guidance helped me during the time of research and writing of this thesis. His timely advice, meticulous scrutiny and overwhelming attitude to help his students have helped me to very great extent to complete this work. I wish to express my deep gratitude to Prof. Dr. Dag Heinemann who cared about my work and agreed to become the second supervisor. It is great sense of pleasure to thank my third supervisor Prof. Maik Rahlves for his intellectual comments and recommendations. I would also like to thank Dr. Oliver Melchert for helpful scientific discussions, co-operation through out my study period and feedback. Some of the experimental works were not possible without initial guidance from Dr. Axel Guenther. Last but not least, I would like to thank my parents, husband and late brother for their love, kindness and continuous support during my entire PhD .

Abstract

There is a need to the development of hybrid simulation concepts to describe the light interactions with polymers. Usually, in order to develop comprehensive a description, a multi physics approach is required, i.e., to take into account all relevant parameters such as polymerization, mechanical properties and temperature. The aim of this thesis was to develop a multi-scale and multi-physics simulation approach to simulate the formation of polymer-based photonic components and their optical properties as function of ambient parameters such as temperature. In particular, the case of self-written waveguides which are the interconnects written by light itself was examined. The material interaction with light, the induced polymerization process in monomer/polymer material sample and the influence of temperature on the optical properties was investigated.

The research activities presented in the thesis involved optical simulations, parameter studies, experimental validations and thermo-mechanical simulations of polymer based optical waveguides to be used as interconnects in integrated photonic circuits. The motivation behind confining the research to polymer class material is its processability, high flexibility and ultimately lower cost than corresponding glass counterparts. A very simple and reliable technique by means of self-written waveguides was applied to fabricate and simulate such couplers. Initially, a custom research code for the optical simulation of polymer self-written waveguides (SWWs) was developed. A Crank-Nicholson(CN) based finite difference scheme beam propagation method (BPM) in conjunction with transparent boundary conditions (TBCs) was implemented by applying paraxial approximations to the Helmholtz equation. Other bench-marking photonic components, such as, Y-branch, straight waveguide, bent waveguide and Mach-Zehnder interferometer were simulated using the CN-BPM approach. Furthermore, the photonic components were simulated using the commercial tool RSOFT and the obtained results are compared to the CN-BPM approach for validation purposes. The parameter study was carried out for bench-marking the calculation of insertion loss, mode-mismatch loss, effective refractive indices

and the number of guided modes. Two kinds of material models, named as phenomenological model and diffusion model, were implemented to exactly describe the refractive index modulation within the material sample. These material models are further linked with the CN-BPM scheme to obtain the evolution of SWWs during their writing mechanism.

A comparative study on the theoretical predictions from two kinds of material models for simulating straight and bent SWWs was carried out. Further, a series of numerical investigations were performed on a bent coupler using the diffusion based material model. The temporal dynamics of refractive index modulation along with the corresponding intensity distributions during the curing mechanism of bent couplers are reported. Apart from this, the possibility of misalignment compensation with the increase in length of the bent coupler, regulation of the curvature and curing time of a coupler by controlling specific model parameters in the simulation are presented.

Another interesting aspect of the research involved the validation of the obtained experimental results from the one polymer approach with the theoretical predictions from the diffusion material model. Optical interconnects of various length scales between two multi-mode fibers were fabricated. Their corresponding attenuation coefficient was calculated and compared with the theoretically predicted attenuation coefficient. In general, a good agreement between the attenuation coefficients was observed which demonstrated a successful application of the diffusion material model to the epoxy based acrylate SWW. The transmittance from an SWW interconnect during the writing process was recorded from both simulation and experiment. The evolution of the shape of the SWW at different time steps during simulation and experiment were compared. Also, attenuation measurements between optical fibers with SWWs as interconnects and one without SWW, i.e. with an air gap in between, were performed.

Finally, the research activity was focused on combining the thermo-mechanical and optical simulations and to carry out a comprehensive analysis of planar polymer waveguides. The finite element approach was followed for stress/deformation and thermal simulations. The results of the finite element analysis were coupled back to the CN-BPM results, so the optical simulation as a function of temperature was obtained for polymer waveguides.

This thesis is organized as follows: Chap. 1 presents the introduction and motivation that emphasizes the adaption of optical interconnections in various domains and then signifies the growth of the emerging photonic market. Chap. 2 addresses waveguiding fundamentals to describe the function of optical waveguides. The classifications of optical waveguide, waveguiding design methodology and their propagation techniques are reported. Furthermore,

polymer waveguides are introduced as the research work presented in the thesis revolves around the polymer material class system. In Chap. 3, the implemented numerical method, Crank-Nicolson (CN-BPM) finite difference scheme in conjunction with transparent boundary condition, to carry out optical simulations of various photonic structure is described. The obtained simulation results were validated against a commercial software RSOFT by comparing the simulations results of benchmarking photonic structures. Chap. 4 investigates two implemented material models named phenomenological model and diffusion material model. It introduces the concept of self-written wave-guides. Further details on coupling material models equations with the CN-BPM scheme to demonstrate the change the SWW formations is described. The theoretical predictions by simulating a straight and bent SWW from two kinds of material models are presented. In Chap. 5, the employed diffusion material model to perform various numerical investigations on bent SWW couplers is presented. The investigations are carried out to find an adequate temporal dynamics of refractive index modulation that supports the movement of maximum focus points of intensity. Further investigations on the increased misalignment compensation with respect to coupling or gap length, and the influence of propagation distance on bending and width of a bent SWW are reported. Chap. 6 examines various experimental as well as theoretical studies of polymer base SWWs with respect to the evolution of intensity profiles of SWWs and their transmittance during the writing mechanism. Furthermore, the attenuation was calculated for many fabricated polymer waveguides in experiment and then compared with the predicted attenuation from simulation models. A combined simulation approach that focuses on the thermo-mechanical and optical study of planar polymer waveguide structures is employed. First, two waveguide models are designed with implanted polysilicon microheater to report the impact of induced temperature gradients on refractive index modulation. The optical simulations as a function temperature gradients and the deformation analysis to find corresponding elongations in waveguide dimensions are discussed. Finally, in Chap. 7, the results obtained in this thesis are briefly summarized and an outlook towards future directions is given.

Keywords: Polymer waveguides, Multi-physics simulations and Photo-polymerization

Contents

1 Introduction and Motivation **1**

2 Background **7**
2.1 Guided wave optics 7
2.2 Classification of optical waveguides 8
2.2.1 Single-mode and Multi-mode waveguides 10
2.2.2 Attenuation 10
2.3 Fundamental theory of waveguiding 11
2.3.1 Ray Optics Approach 11
2.3.2 Wave Optics Approach 12
2.4 Waveguide design methodology 14
2.5 Polymer Waveguides 15

3 Numerical Method for Optical Simulation **19**
3.1 SVE approximation and Beam propagation method 19
3.2 Scalar beam propagation 22
3.2.1 Finite Difference (FD) approach on BPM 22
3.2.2 Crank-Nicolson(CN) Scheme 24
3.3 Transparent boundary condition (TBC) 26
3.4 Validation of CN-BPM implementations with commercial software RSoft 27
3.4.1 Design and simulation of LWL structure - Straight Waveguide 28
3.4.2 Design and simulation of bent waveguides 31
3.4.3 Design and simulation of Y branches 35
3.4.4 Design and simulation of Mach-Zehnder interferometers 39
3.5 Parametrized study on bench-marking optical interconnects . . 40
3.5.1 Mode mismatch loss 41
3.5.2 Power attenuation 41
3.5.3 Effective refractive index and number of guided modes 43

4 Development of Material Models 44
4.1 Self-Written Waveguides(SWWs) 44
4.2 Material model 1: Phenomenological model 46
4.3 Material Model 2: Diffusion model 48
4.4 Model Comparison 52
4.4.1 Numerical parameters 52
4.4.2 Comparison of the evolution of a bent SWW for the two models 54
4.4.3 Comparison for the evolution of a straight SWW for different models 57
4.5 Simulation of the beam splitting effect 59
4.6 Simulation of multi-beam propagation 60

5 Numerical Investigations on a bent SWW 63
5.1 Numerical model and parameters 65
5.2 Temporal dynamics of refractive index and beam intensity . . 67
5.3 Investigation for offset tolerance 70
5.4 Curvature of bent couplers 73
5.5 Impact of component concentrations on the curing time 74
5.6 Impact of rate constant on curing time 75

6 Experimental and theoretical analysis 77
6.1 One polymer-approach 77
6.2 Experimental set-up 78
6.3 Theoretical simulations and numerical parameters 83
6.4 Evolution of straight SWWs in experiment and simulation . . 84
6.5 Transmittance comparison during the writing process of an SWW 85
6.6 Attenuation in experiment and simulation 87

7 Combined thermo-mechanical and optical simulations 91
7.1 Thermo-mechanical simulations 93
7.2 Model design 94
7.3 Thermal analysis of polymer waveguides 99
7.4 Multi-physics thermo-optical simulations 102
7.5 Stress and deformation analysis 105

8 Summary and Outlook 108
8.1 Summary 108
8.2 Outlook 111

Chapter 1

Introduction and Motivation

The next generation data transmission depends on the potential improvement of optical interconnects to accommodate the increase in aggregate data bandwidth as well as the speed over the link. Now-a-days, the traditional electric metallic wire data transition is substituted by optical waveguides ranging from short distance to ultra short distance transmission and also in the telecommunications over long distances transmission as these optical interconnects are not susceptible to cross talks or radio frequency interference [1, 2, 3, 4, 5]. It is not the purpose of the thesis to argue the difference between electrical and optical interconnections. Such scenarios are well reviewed in [6]. The research community has placed great interest for the optical circuit components because optics solves most of the physical problem that is limited by the electrical interconnections. Now-a-days optics play a vital role in communication computing network as well. One such adaptation over the years in IBM supercomputers is demonstrated in the Fig. 1.1 [2]. In the year 2008, the photonic was exclusively used at the card age in the IBM's former supercomputer ROADRUNNER. After three years, photonics was brought onto the board for the first time in POWER 775 supercomputer in which many optical transceiver modules were connected to board edge by MM optical fibers, see Fig. 1.1(b) [2]. Now the research is more focused to improve the density of optical interconnects massively and to minimize the assembly cost.

The global photonic market has witnessed significant growth due to the wide range application of photonics to various domains such as automotive, lighting, medical science, manufacturing and information technology. There is continuous demand for various photonic products and a forecast for this emerging photonic market by products is shown in the Fig. 1.2. The optical waveguides are the fundamental elements to transmit the light. SWWs are a special occurrence of optical waveguides that provide a mean for interconnections between various

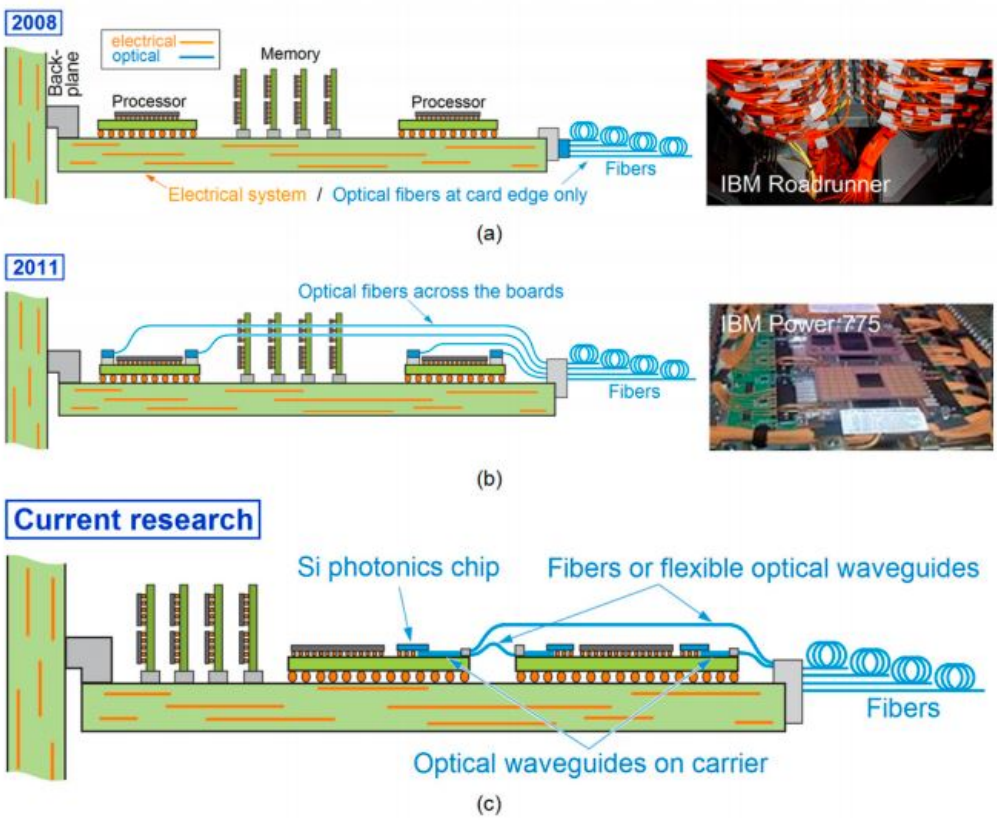

Figure 1.1: *Photonics integration: (a) In 2008: IBM's former No. 1 supercomputer ROADRUNNER with optics (AOCs) at the board edge only. (b) In 2011: IBM's HPC system POWER 775 with many optical transceivers assembled on carriers and a huge number of fibers connected with the board edge. (c) Current research: optical polymer waveguides connecting photonics chips assembled on carriers with the carrier edge, other carriers, and board edge. [2]*

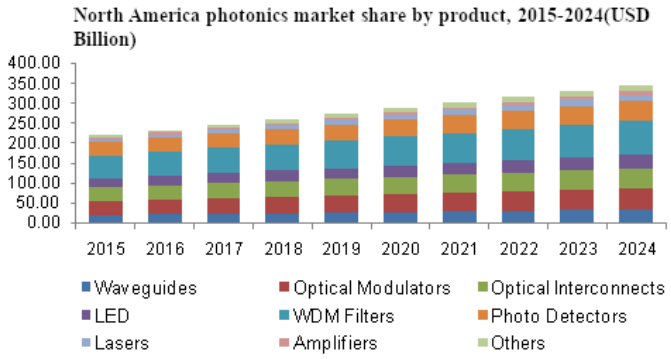

Figure 1.2: *Emerging photonic market by products over a forecast period, see Ref. [7]*

elements (waveguides, laser diodes and other optoelectronic devices) in the integrated photonic circuits. Optical interconnection refers to the kind of data transmission where the data is transmitted by modulating the optical carrier wave and then propagating the light through a transparent media such as optical waveguides. These optical interconnects have received very much attention in recent times as they are used to improve the performance of data transmission on the PCB and chip. The optical interconnects are often realized through guided wave optics. The light source is generally generated from a laser diode (LDs) and the optical signal is then transmitted after the modulation, which at a later stage is converted back to electrical domain by using a photo-detector. While introducing the optical interconnects to commercial applications, there is always a prerequisite to emphasize on the cost per interconnect capacity and the required PCB area, those should be competitive of equivalent copper solutions [8]. The success of the broadband communication in optical networking and computing is of course relying on the advancement of many optical interconnects, such as, multiplexer, demultiplexer, tunable filters, amplifiers, variable optical attenuators, splitters and combiners [9].

A fully embedded board level optical interconnection system is shown in the Fig. 1.3. All the optoelectronics components including the vertical-cavity surface-emitting laser (VCSEL) array, p-i-n photodiode array, total internal reflection coupling mirror, and the planar polymer waveguides were integrated within three-dimensional (3-D) interconnection layers during the conventional PCB fabrication processes [10]. In Fig. 1.3 (b), the electrical signal is converted into an optical signal by 1×12 VCSELs, which is then transmitted through a 12 channel polymer waveguides and afterwards converted back to electrical

signals by a 12 channel p-i-n photo diode. The schematics of various photonics components which are inevitable parts of a conventional photonic integrated circuit are shown in Fig. 1.4.

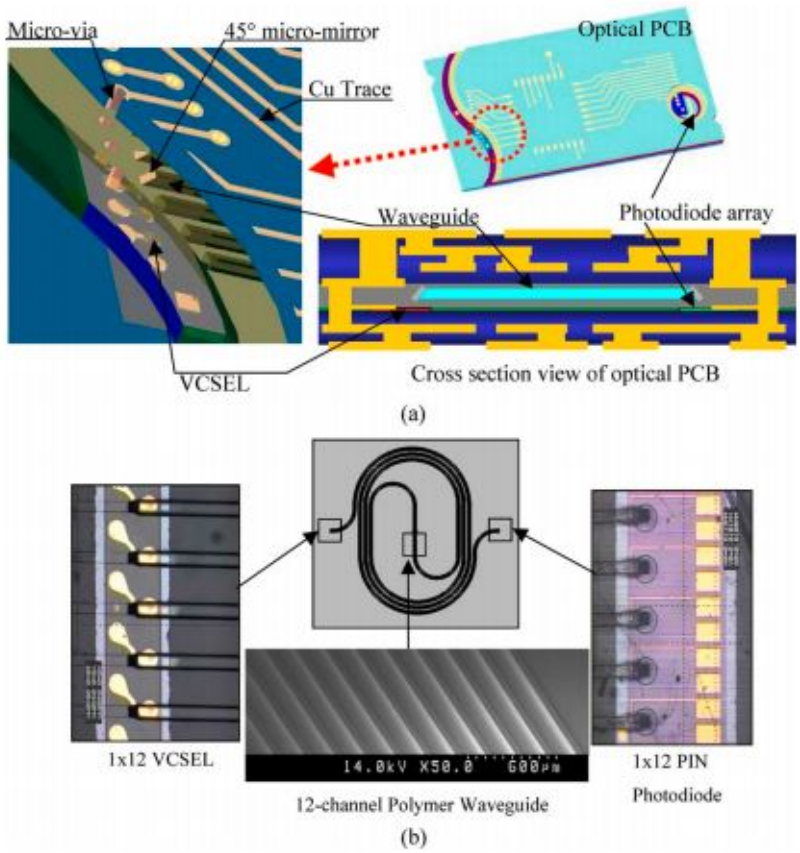

Figure 1.3: *Schematic diagrams of the fully embedded board-level optical interconnection system. (a) 3-D cross-sectional view of an optical layer-interposed PCB. (b) 12-channel optical waveguide film layer with an integrated thin-film VCSEL and p-i-n photodiode arrays. [10]*

The research work presented in the thesis is based on polymer material optical waveguides because the combination of optics and polymer benefit many applications. Polymer interconnects have received much attention in recent times because of their potential applications in integrated photonic circuits or telecommunication network sectors. The main reason behind this is that these polymer interconnects are highly flexible, light weight, easy to process and ultimately low cost. The mentioned properties provide some major advantages

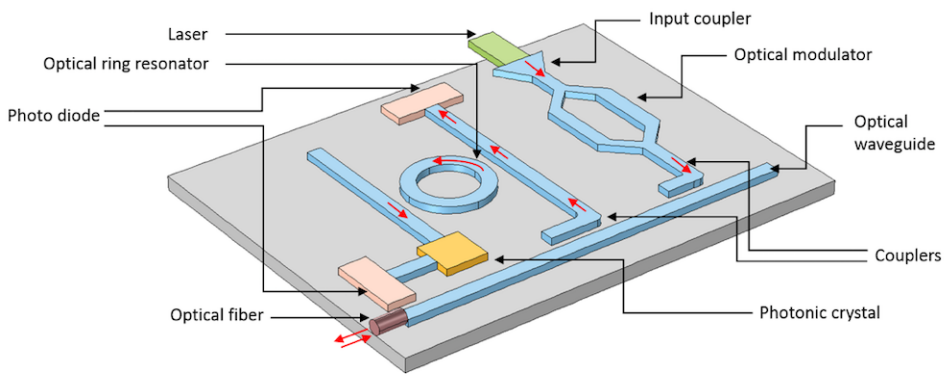

Figure 1.4: *Schematic of different photonic components, used in photonic integrated circuits. For more information, see Ref. [11]*

compared to silicon counterparts. A very high expectation is placed over polymer material to be used in applications ranging from polymer backplanes to complex photonic devices or sensors. The study is focused on the optical interconnects or waveguides on polymer basis those can be used as light weight interconnects in integrated photonic circuits or telecommunication networks.

To fabricate polymer based interconnects, various approaches such as femtosecond laser writing [12], photolithograpy [13], direct laser ablation [14] and hot embossing [15] were proposed. As previously explained, self-writing technique is is one of the simple and reliable approach to fabricate optical interconnects in polymer which was first proposed by Frisken [16]. The SWWs(self written waveguides) are created by the self-action of light where the excitation beam is focused and trapped within the material medium due to self-induced change in the refractive index along the direction of beam propagation. The photo-polymerization process is local in space, however non local in time. The refractive index modulation is larger in the higher intensity regions and also it depends upon the history of electromagnetic fields in earlier times. This is very much similar to the Kerr effect. In comparison to the later, the photo-polymerization mechanism provided the possibility to write SWWs by using low intensity laser beams [17]. Already various theoretical and experimental studies were performed to understand the underlying self-writing mechanism of light within photo-polymer as well as in photosensitive materials [18, 19, 20, 21, 22, 23].

As a part of the collaborative research project Hybrid Numerical Optical Simulation (HYMNOS) and the Cluster of Excellence PhoenixD, this work

aims at developing customized simulation concepts of light matter interactions for polymer material. In this context, a Crank-Nicolson (CN) based finite difference scheme in conjunction with transparent boundary conditions (TBCs) was implemented for the two-dimensional beam propagation equation that accurately describes the interaction between light and polymer by taking all relevant effects into account. Two material models were implemented to describe the refractive index evolution in the polymer material sample when light beams propagated through them.

Apart from this, in-house experiments on polymer SWWs were carried out in the HOT laboratory to validate experimental measurement results with the simulated predictions. The study involved the demonstrations of transmittance, temporal dynamics of beam intensities and attenuation of SWW during the writing mechanism by using a one polymer material approach. Next, a combined thermal, mechanical and optical simulation and analysis approach was developed. The environmental stability is the key issue for optical polymers. Heat and stress could eventually lead to deformations in them. A slightly change in thermally induced refractive index significantly changes the light intensity distribution significantly. The optical simulation results from the CN-BPM scheme were coupled with the thermo-mechanical simulation results. The thermo-mechanical simulations were conducted by finite element simulation in the FEA Toolbox. The established feedback helped to determine the optical simulation as a function of temperature gradient for planar polymer PMMA waveguide. Other optical properties such numerical aperture (NA) and beam intensity profiles were studied further with respect to temperature gradient influence.

Chapter 2

Background

The following chapter first describes the optical waveguides which are the key components in this work and provide the mean for interconnections between various element in integrated photonic circuits. The basic waveguiding theory such as ray-optics and wave-optics approaches are presented. Various wave propagation techniques are considered. Furthermore, the reason behind taking into account the Crank-Nicholson beam propagation method (CN-BPM) to compute the beam intensities within waveguides is emphasized. The details about the implementation process of the equations for the CN-BPM scheme are described in the chapter 3. The current research work is based on the polymer material system. So, a brief introduction to polymer material waveguides is provided at the end.

2.1 Guided wave optics

The advancement of broadband telecommunications will rely on the advancement of optical and other photonic components. The optical waveguides are fundamental elements and they provide the mean for interconnections between various element in integrated photonic circuits. The concept of guided wave optics depends on the phenomenon of total internal reflections that confines the light signal within the optical waveguides. Mostly, the size of optical waveguides are on the order of the magnitude of propagating wavelength in integrated optical circuits. The concept of integrated optics was constructed in the year 1960 that relied on the advancement of many planar optical waveguides as well as many other planar circuitry components. A typical integrated optical circuit was designed to have certain function by incorporating and integrating a laser diode as the source, switches/modulators as functional components,

interconnection waveguides, and then the photo diodes as detectors. Waveguide devices in photonic integrated circuits generally come in different shape with various function and providing the connection between various optical devices and components for splitting, focusing, generating, coupling and modulation light source. The advancement of fabrication of planar optical components and their integration to the planar optical circuits exhibit many advantages over the traditional electronic circuits. The invention of laser and coherent optics enabled the long distance transmission by optical fiber at all frequencies up to the microwave range.

2.2 Classification of optical waveguides

According to the mode structure, refractive index distribution, geometry and the material, various classifications were proposed for optical waveguides. They are classified into single-mode or multi-mode depending on the mode structure of the propagating electromagnetic field. Each mode in the propagating field is identified by its specific frequency, effective refractive index, power distribution and polarization [24]. According to their geometry, waveguides are classified as strip, planar or fiber waveguides. Furthermore, the optical waveguides are separated into gradient index or step index waveguides by considering the refractive index distributions. In one recent study, the hybrid index profile for high power amplification was reported by combining graded index and step index waveguides [25].

Various materials are appropriate for their fabrication, such as glass, polymer and semiconductor. Many current waveguides are based on polymer, silicon or silica, lithium niobate and III-IV compounds materials. According to Saleh and Teich waveguides devices are classified as active devices or passive devices [26]. Passive devices show a static characteristic for the optical waves. Some examples include 3D bent waveguides with a change in the path direction, bent or s-shaped waveguides, tapered waveguides, cross waveguides and directional waveguide couplers for combining or dividing the optical power. The active devices are functional devices to control the optical wave.

In such devices, the guided waves are controlled by external input signal such as magneto-optic, thermo-optic, electro-optic and nonlinear optic effects to achieve amplitude modulation, phase modulation, polarization-state rotation, and frequency shift [26]. A dielectric waveguide comprised of a high index medium called core which is surrounded transversely by a low index medium called the cladding. The most widely used optical waveguides are broadly designed as 2D planar slab waveguides or 3D channel waveguides [27]. A

schematic of the planar 2D optical waveguide is shown in the Fig. 2.1(a). Here the optical confinement goes only in one transverse x direction with index profile $n(x)$ and the core is sandwiched between the claddings layers. They are primarily used for high power waveguide laser and amplifiers [28]. The schematic of non-planar 3D channel optical waveguides is shown in the Fig. 2.1(b). It is comprised of 2D transverse optical confinement and the core is surrounded by a cladding in all transverse directions. $n(x, y)$ is the refractive index that is a function of both x and y coordinates. The channel waveguide could be raised, embedded strip or buried, as shown in the Fig. 2.2.

The schematics of various basic optical components using modified channel waveguides such as Mach-Zehnder, directional coupler, branching, crossing and intersection waveguide configurations, are shown in the Fig. 2.3. Many studies presented in later chapters are based on the planar slab waveguides because of our interest in simplifications which confines the propagation of light in one dimension. [9].

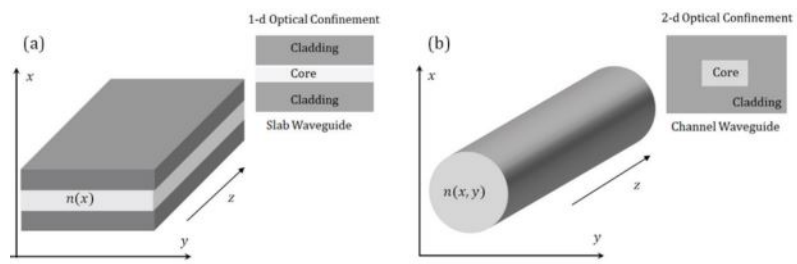

Figure 2.1: *(a) Planar optical 2D waveguide, 1d transverse optical confinement (b) channel waveguide 3D with 2-d transverse x, y confinement, taken from Ref. [28].*

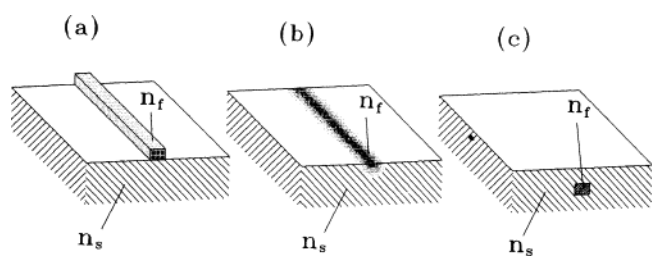

Figure 2.2: *Some types of channel waveguides (a) raised, (b) graded-index embedded, and (c) buried. [29]*

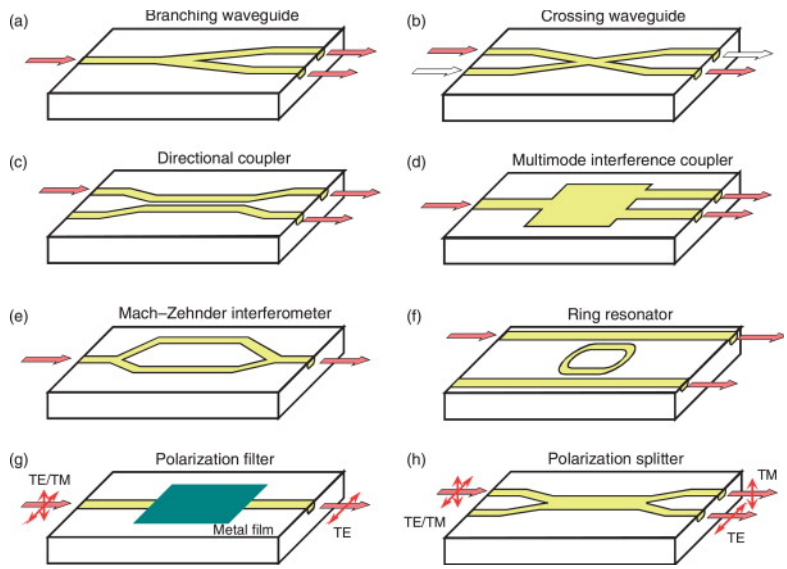

Figure 2.3: *Various optical components using modified channel waveguides. TE, transverse electric; TM, transverse magnetic. [30]*

2.2.1 Single-mode and Multi-mode waveguides

The number of modes propagating in waveguides is generally determined by the V number. The V parameter is calculated by knowing the core-radius of the waveguide a, the light wavelength λ and the numerical aperture NA, $V = \frac{2 \cdot \pi \cdot a}{\lambda} \times$ NA. Only one mode propagates when the V number is smaller than 2.405. Otherwise, the waveguide is called multimode. The number of modes is approximated as: $N = V^2/2$ for the step index profile and $N = V^2/4$ for the graded index profile. There are always two propagation states in orthogonal polarization directions, even in singlemode fibers. The number of mode always depend on the wavelength. The number of modes in relation to different optical fibers and profile types is provided in [31].

2.2.2 Attenuation

When the light propagates through a fiber of length L, the power of the light is decreased. According to Beer-Lambert's law, the optical power is obtained via $P_L = P_0 \cdot e^{-\alpha' . L}$, where P_L is the power of the light after passing through a fiber of length L in km and P_0 is the power at the front end. The linear attenuation coefficient is α'. Generally the attenuation coefficient is expressed logarithmically as α in dB/km, i.e. $\alpha = 10/L \cdot log \frac{P_0}{P_L} = 4.343 \cdot \alpha'$. The normal

attenuation a value is a dimensionless variable, expressed in dB. It is obtained by the product $\alpha \cdot L$. Very often a clear distinction between the attenuation coefficient α and attenuation factor a is not mentioned in technical literature. They both are practically always represented as positive numbers.

2.3 Fundamental theory of waveguiding

It is necessary to completely understand electromagnetic waves to further study the light propagation in optical waveguide channels. The basic waveguiding theory is comprised of the ray-optics and wave-optics approach. They both are applied to the waveguide structures with proper boundary conditions and help understand the wide variety of optical components and systems.

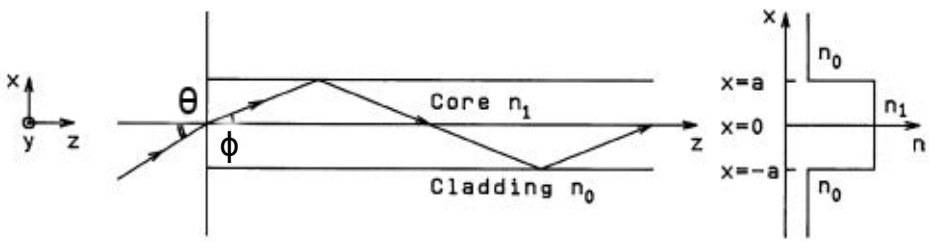

Figure 2.4: *The basic structure and refractive index profile of a optical planar step-index waveguide [32].*

2.3.1 Ray Optics Approach

The optical ray model is one easy way to describe the propagation of guided waves in a medium without considering the Maxwell equations [33]. The light is described by ray beams that travel between different media by obeying a set of geometrical rules. The Snell's law, also known as the law of refraction explains the behaviour of the wave propagation between these two dielectric media having different refractive indices of n_1 and n_0, respectively. The basic refractive index structure of a planar optical waveguide is shown in the Fig. 2.4. The light can either refract towards or away from the normal while crossing the boundary between the two media. An interesting case of refraction happens when the light travels from the medium with higher refractive index n_1 to a lighter medium with lower refractive index n_0, Fig. 2.4. The light beam that is coupled to the waveguide will confine to the core by a phenomenon called total internal reflection. At the core-cladding interface, the condition for total

internal reflection is given by $n_1 \sin(\pi/2 - \phi) \geqslant n_0$. The incident angle θ is related to the refracted angle ϕ by $\sin\theta = n_1 \sin\phi \leqslant \sqrt{{n_1}^2 - {n_0}^2}$. The critical condition for the total internal reflection is obtained by Eq. 2.1 [32]. One could demonstrate that when the angle of incidence is greater than the critical angle, no light will be transmitted to the surrounding medium and total internal reflection (TIR) occurs.

$$\theta = \sin^{-1} \sqrt{{n_1}^2 - {n_0}^2} \equiv \theta_{max} \tag{2.1}$$

As the refractive index difference between the core and cladding $n_1 - n_0$ is of order 0.01 or 0.001, Eq. (2.1) is approximated to $\theta_{max} \cong \sqrt{{n_1}^2 - {n_0}^2}$. Here, θ_{max} is the numerical aperture (NA) or the maximum light acceptance angle of the waveguide. The relative refractive index distribution is expressed as the refractive index difference between the core and cladding for weakly guided media, as $\Delta n = \frac{n_1 - n_0}{n_1}$. A symmetrical waveguide has got the same boundary conditions for the upper and lower claddings, however, in case of different layers such as a substrate and a upper cladding, the waveguide is called asymmetrical.

2.3.2 Wave Optics Approach

In classical theory, the behaviour of light is described by waves of electromagnetic (EM) fields that propagate in form of two mutually perpendicular and coupled electric and magnetic fields. One should derive the wave equations to understand the propagation of light within the waveguides. The EM wave equations are derived from the Maxwell equation by holding a few assumptions that we are operating in a source free ($\rho = 0, \vec{J} = 0$), linear (ϵ, μ are independent of E and H) region in an isotropic medium. The time dependent behaviour of the optical fields are fully described by using the set of Maxwell's equations. In a source free region ($\rho = 0, \jmath = 0$), the Maxwell equations are expressed as Eq. 2.2 [34] [11].

$$\nabla \times \vec{E} = -\frac{\partial \vec{B}}{\partial t} \tag{2.2a}$$

$$\nabla \times \vec{H} = \vec{J} - \frac{\partial \vec{D}}{\partial t} \tag{2.2b}$$

$$\nabla \cdot \vec{B} = 0 \tag{2.2c}$$

$$\nabla \cdot \vec{D} = \rho \tag{2.2d}$$

$$\tag{2.2e}$$

Here, $\vec{D}$ and $\vec{B}$ are electric and magnetic fluxes, respectively. The Eqs. 2.2(a) and 2.2(b) are vector equations relating the space and time derivatives of the

fields whereas Eqs. 2.2(c) and 2.2(d) are scalar equations providing information about the outflow of electric and magnetic fields. $\vec{B}$ and $\vec{D}$ are defined as $\vec{B} = \mu\vec{H}$ and $\vec{D} = \epsilon\vec{E}$, [32]. The electromagnetic properties are described by ϵ and μ which are the dielectric permittivity and magnetic permeability of the medium, respectively. The wave equations are obtained from the Maxwell equations by applying the vector identity of the form $\bigtriangledown \times \bigtriangledown \times \vec{V} = \bigtriangledown(\bigtriangledown \cdot \vec{V}) - \bigtriangledown^2\vec{V}$ to Eqs. 2.2(a) and 2.2(b). Then the obtained vector wave equation is provided in Eq. (2.3).

$$\nabla^2\vec{E} - \mu\epsilon\frac{\partial^2 E}{\partial t^2} = -\nabla(\vec{E} - \frac{\nabla\epsilon}{\epsilon}) \tag{2.3}$$

However, the right side term is neglected for the guided wave medium as it has have graded permittivity. In graded permittivity, various layers of dielectrics are used and the relative permittivity is inversely proportional to its radius of distance from the center. So, the final wave equations for electric and magnetic field amplitudes are obtained as Eqs. (2.4) and (2.5).

$$\nabla^2\vec{E} - \mu\epsilon\frac{\partial^2\vec{E}}{\partial t^2} = 0 \tag{2.4}$$

$$\nabla^2\vec{H} - \mu\epsilon\frac{\partial^2\vec{H}}{\partial t^2} = 0 \tag{2.5}$$

The wave solutions are commonly classified into transverse electromagnetic (TEM), transverse electric (TE) and transverse magnetic depending on their state of polarization that is defined by the direction of field oscillations in uniform waveguides [9]. The time harmonic EM wave equations with angular frequency ω and propagating through a medium (μ, ϵ) must satisfy the Maxwell's equations [35]. The general time harmonic EM wave equations are described below in Eq. (2.6) and Eq. (2.7).

$$\nabla \times \vec{E} = -i\omega\mu\vec{H} \tag{2.6}$$

$$\nabla \times \vec{H} = i\omega\mu\vec{E} \tag{2.7}$$

The above Eq. (2.6) and Eq. (2.7) are manipulated to obtain the Helmholtz equations for electric and magnetic fields, provided in Eq. (2.8) and Eq. (2.9).

$$\nabla \times \vec{E} + (k^2 - n^2)\vec{E} = 0 \tag{2.8}$$

$$\nabla \times \vec{H} + (k^2 - n^2)\vec{H} = 0 \tag{2.9}$$

Here, $k = \omega\sqrt{\mu\epsilon}$ is the wave number which is complex valued for lossy media and real valued for lossless media. The general plane wave equations, Eq. (2.10),

Eq. (2.11), propagating through an arbitrary medium in $+z$ direction with an propagation constant β are obtained from the solutions of the Helmholtz equations. The propagation constant is one significant parameter in determining the quality of the waveguide that is used to identify the number of individual modes. It is also defined as the eigenvector of the mode.

$$\vec{E} = \vec{E}e^{i(\omega t - \beta z)} \tag{2.10}$$

$$\vec{H} = \vec{H}e^{i(\omega t - \beta z)} \tag{2.11}$$

By substituting Eq. (2.10) and Eq. (2.11) in Eq. (2.8) and Eq. (2.9), the time independent scalar form of the wave equations for the electric and magnetic fields are obtained [34]. The scalar form of the TE mode, where the $\vec{E}$ field is polarized along the y axis can be brought to the following form:

$$\frac{\partial^2 \vec{E}_y}{\partial x^2} + (k_0^2 n_i^2 - \beta^2)\vec{E}_y = 0 \tag{2.12}$$

The TM modes are the other set with $\vec{H}$ in the y direction. The entire magnetic field is along the transverse plane, i.e perpendicular to the beam propagation axis. The derivation for TM mode equations could be referred from [36]. In scope of the thesis work, only the TE mode as the operating mode in various waveguides is considered.

2.4 Waveguide design methodology

The design of optical waveguides or photonic components relies on the wave propagation techniques. Any arbitrary launch technique is possible to monitor the evolution of light beam at any point location inside the structures during the simulation of these components. Various propagation techniques were already proposed for time domain as well as for the frequency domain analysis. Some of the popular waveguide design techniques include the FDTD method, split-step method (SSM), finite element method (FEM), beam propagation method (BPM) and eigenmode expansion method (EME) etc. A large number of commercial packages are also available (not listed here) and they allow the optical path optimizations. Generally, rigorous time-domain methods are adapted for these commercial packages/tools. The FDTD (finite difference time domain) method is based on the discretization of the time dependent Maxwell equations where the grid spacing goes to zero. The FDTD method can become computationally exhaustive specially for 3-dimensional case and is therefore not practical to model very long photonic devices or waveguides

[37]. The SSM is a straightforward technique that allows the modelling of all major effects occurring in an optical fiber. It is used to solve nonlinear partial differential equations like the nonlinear Schrodinger equation. The solution is computed in small steps by taking linear and nonlinear steps separately. However, the method is widely used to study the nonlinear pulse propagation in optical fibers. The FEM technique is able to handle complex geometries such as waveguides with complex arbitrary cross-sections. The field region was discretized into elements of various shapes, such as rectangles or triangles and it allowed the modelling of an irregular grid. The analytical function is applied to each element and the final solution is computed by summing up the results to create a eigenvalue matrix equation [38]. The FEM technique is used for propagation problems and mode solving in case of optical waveguides. However, the FEM method is used to obtain the approximate solution of a PDE (partial differential equation) by supplying an equivalent ordinary differential equation. The obtained solution also varies with change in shape and size of the discretized element. The EME method is relatively simple and generally used to model grating structures.

The works carried out during this thesis adapted the BPM technique for the designing of the optical waveguides. The BPM is very well developed and widely used method to solve the wave propagation problems. Many different and advanced techniques were developed such as vectorial and semi-vectorial implementations, bidirectional and wide angle BPM. It is used to analyse the light propagation in slowly varying guiding medium, such as couplers, bends and tapers. Various approaches were applied to compute the derivatives that generated FD(finite difference)-BPM, FFT (fast fourier transform)-BPM and FE (finite element)-BPM. Earlier, FFT-BPM was widely used until the FD-BPM came out. The Crank-Nicholson method is the standard implementation for the FD-BPM scheme that solves the Helmholtz equation in paraxial approximation. This provided the BPM method to be used to analyse much longer structures than using FDTD method and is a more realistic approach. Although low index contrast optical waveguides are designed using the BPM method, it can also be used to model high contrast structures. A detailed analysis of the implemented CN-BPM method is provided in the sub-chapter 3.

2.5 Polymer Waveguides

Many great material classes were developed for the optical waveguides because of their unique certain advantages. The glass optical fibers are frequently used

as the optical signal can be conveniently carried over for long distance through them. However, their usage is limited for highly dense circuits with many ports because the glass material tends to be sensitive to vibration as well as highly fragile. The semiconductor based optoelectronic components and waveguides are also widely employed because they offer easy integration with the active devices operating at 1550 nm.

The silica-on-silicon waveguides exhibit low loss and high thermal stability [39]. However, the processing of the semiconductor material is always remained expensive and complex. There were certain drawbacks that paved the way for more research into polymer material system where the chosen polymer materials provided advantages [40, 41]. A very high expectation is placed for the polymer as they offered rapid processability, high yield or performance at low cost. Polymer waveguide have got potential application in broadband telecommunication connections, i.e. for computing systems, optical networks and sensor networks. All these systems rely on the advancement of optical waveguide manufacturing technology to produce low-loss waveguides and interconnects as well as methods for their comprehensive analysis taking into account all relevant physical effects. Various photonic devices were fabricated by using the polymer based waveguides, e.g., thermal optical switches (TOS) [42, 43], optical couplers/splitters [44, 45, 46], variable optical attenuators (VOA) [47, 48] and arrayed waveguide gratings (AWG) [49, 50]. The fabrication and design of a polymer transition path for sensing and communication applications is demonstrated in [51]. Also, a study was carried out by Felipe et al. to review the integration of the polymer based photonic components to photonic circuits for the next generation data center systems [52]. Many fabrication techniques are already proposed earlier for optical interconnects. One of the very simple and reliable technique is already explained in the previous chapters that exploits the self-writing concept of the laser beam in the photosensitive and photopolymer media. Another simple and cost efficient fabrication technique for the planar polymer optical waveguide through doctor blading and hot embossing technique was investigated by Rezem et al. [53, 54]. An interesting fabrication method by the dip floating technique for the waveguide biosensors was demonstrated in [55]. Using the femtosecond laser writing technique the PMMA grating structures are realized in [56].

The bifringence and loss produced by the polymer material is also less compared silica. The polymer material offers high tunability in terms of larger thermo-optic coefficient and environmental stability. Polymer material could play a key role in the broadband communication, thus various classes of polymer material are engineered in laboratories worldwide. Most commonly used polymers for the integrated photonic circuits include acrylate, polycarbonate,

olefins (e.g. cyclobutene) and polymides [13]. The polymers are then categorized into photosensitive and non-photosensitive types which followed alternate fabrication techniques to realize the optical components. The photosensitive polymers exhibit distinctively different properties from non-photosensitive polymers when exposed to light in UV or visible spectrum as a result of cross linking between monomer molecules. For waveguide design, the core part of the polymer waveguide must have higher refractive index than the cladding polymer part. The wavelength of the light source and the waveguide dimension strongly impact the refractive index between core and cladding for singlemode or multimode waveguides.

The bifringence is an important parameter in accessing the material sustainability and optical anisotropy. Birfringence is also related to stress build-up in isotropic material during material processing or thermal treatments. It is often measured as the difference in refractive indices for the two rays which is controlled in polymer materials to have extreme low birfringence ($10^{-5}, 10^{-16}$, the limit of measurement) close to zero. They show very little disorientation during processing mostly in 3D cross-linked polymers [57, 24]. Tagaya et al. demonstrated various kinds of bifringence (orientations, photo-elastic and intrinsic) graphs for polymer materials in [58]. The refractive index of the polymer material varies more rapidly with temperature which is one of the fundamental difference between polymer and other optical material. This refractive index variation with temperature ($\frac{\mathrm{d}n}{\mathrm{d}T}$) at a constant pressure is known as TO (thermo-optic) coefficient. The refractive index of the polymer change happens at a rate of $10^{-4}/^{\circ}\mathrm{C}$ with temperature which is one order magnitude larger than for glasses. The thermo-optic switches based on the adiabatic waveguide transitions could be realized for polymers as they have low thermal conductivity and large thermo-optic coefficient. Another important aspect is polymer optical materials shall have low optical losses. One normally observes two major types of losses in such materials, i.e, scattering and absorption losses. Norwood et al. have demonstrated that optical polymer materials can be processed in many ways to reduce all these kind of losses [59]. The scattering loss in the polymer material is reduced by adopting the right fabrication technique including the process control [60]. It was also seen that optical polymer material possess low absorption loss below 0.1 dB/cm at key communication wavelengths (840 nm, 1310 nm and 1550 nm) [61]. The environmental stability is a key issue for the optical polymers. The optical as well as the mechanical properties get influenced by environmental conditions such as temperature and humidity, which make them not so suitable for operation in communication. However, extensive research was carried out to yield polymers that show environmental stability [62]. The table 2.1 summarizes the advantages and disadvantages of

glass and polymer waveguides.

Material	Advantages	Disadvantages	Losses
Polymer waveguides (Acrylate, PMMA, Polycarbonate etc.)	Flexible light weight low cost self-aligning rigid mechanical link easy to process	influenced by thermal and mechanical loads	≈ 0.1 dB/cm
Glass waveguides (SiO_2), silica on silicon SiO_2/Si	higher refractive index contrast low temperature influence low loss	fragile difficult alignment only cost effective for large series	≈ 0.1 dB/cm

Table 2.1: *Comparison between polymer and glass waveguides*

Various active and passive photonic components are fabricated by using different polymer materials with many different approaches, e.g., hot embossing [15], femtosecond laser writing [12], photolithograpy [13] and direct laser ablation [14]. The self written waveguide (SWW) in polymer material is one of the reliable and simple technique to fabricate the optical interconnections between the active and passive components in integrated photonic circuits. The concept of SWW was first proposed by Frisken [16]. It is based on the self action effect of a light beam that occured when the beam induced a change in the refractive index of the material. A steerable self-induced SWW is created that propagates the light beams of different wavelength and polarization. The physics of SWWs could be compared with the physics of spatial solitons where the photosensitive material goes for a long lasting change in refractive index by illuminating the material with certain wavelength. Initially, diffraction is observed in the plane of waveguide, later a region of raised refractive index is generated along the propagation axis of the light beam [63, 64, 19, 65].

Such waveguides reduce or completely compensate the beam diffraction and the beam subsequently stays within the material sample for long time. A channel like structure is created after the light confinement which is uniform in nature for refractive index distribution. As the name signifies, this is SWW because the light beam that creates the waveguide is subsequently guided by it. The technique could be applied to write multiple waveguides or other photonic components such as X- and Y-junctions by the intersection of two or more self-written waveguides. The phenomenon is well observed in various photosensitive optical material including photopolymers and photopolymerizable resins.

Chapter 3

Numerical Method for Optical Simulation

The following chapter describes the implemented numerical method to carry out optical simulations on various benchmarking photonic structures, such as, a straight optical waveguide, y-branches, bent waveguides, and Mach-Zehnder interferometers. In this scope, a Crank-Nicolson (CN) based finite difference scheme in conjunction with transparent boundary conditions (TBCs) was applied to the two-dimensional beam propagation equation. The obtained results from the custom optical simulation tool were then compared with the results from the commercial tool (RSOFT) for benchmarking the optical simulations for the above photonic structures and, thus, to verify the validation for implementation.

3.1 SVE approximation and Beam propagation method

The optimization of integrated photonic devices requires the numerical solution to wave propagation techniques of light along the optical structures. Many powerful techniques were already developed to solve the Maxwell's equations and to calculate the electromagnetic field distributions for such devices when subjected to boundary conditions with source distributions. One of the very popular algorithms used is the finite difference time domain (FDTD) method. When the FDTD technique is applied to optical waveguiding structures, they suffer from low computational efficiency. The reason behind this is, that optical waveguides have transversal dimensions on the order of the wavelength of light and their longitudinal dimension is many orders of magnitude larger than the

operating wavelength. Therefore, dealing with optical waveguides, a special numerical technique is required which has the advantage of a preferred direction of propagation (along z axis) and this is referred to as paraxial propagation [66].

The major optical power is transported along the z direction whereas the power flow along the transverse x direction is assumed to be small. This is a direct consequence of the fact that optical integrated photonic circuits vary slowly along z direction. The assumption also holds for the dielectric constant $\epsilon(x, y, z)$ or the refractive index $n(x, y, z)$, i.e $\frac{\partial \epsilon}{\partial z} \approx 0$. It is convenient to introduce the so called slowly varying envelope (SVE) field for the light propagation along optical structures and most of the EM field (electromagnetic) variation is calculated by defining a suitable propagation constant.

The wave equation that governs the electromagnetic field in the slowly varying envelope approximation (SVEA) is the starting point for the beam propagation method (BPM) [66]. Many BPM algorithms were proposed. The first one was based on fast Fourier transformation (FFT-BPM) which was successful to simulate the light propagation in optical fibers [67]. However, the FFT-BPM is suitable only for weakly guiding waveguides and also requires long computation time. The other BPM analogies based on finite differences (FD-BPM) and finite elements (FE-BPM) were also developed to overcome the disadvantages of FFT-BPM [68, 69]. The FE-BPM is superior in terms of discretization to structures. However, FD-BPM is much easier to implement using a rectangular grid. The light propagation in non-linear anisotropic media can be successfully simulated by using the BPM algorithm [70, 71].

The finite difference approach to simulate the light propagation for the photonic components was adapted for this work. The finite difference schemes for scalar propagation in two dimension was the simplest and also the most efficient one that is based on the slowly varying envelope approximation (SVEA) along the z direction. The transverse electric field and the associated SVE fields are related by the Eq. (3.1),

$$E_t = \psi_t e^{-in_0 k_0 z}, \tag{3.1}$$

where E_t is the transverse electric field and ψ_t is the SVE field. n_0 is the reference refractive index and k_0 is the wave number. The SVE field vector is defined by Eq. (3.2)

$$\psi_t = \begin{bmatrix} \psi_x \\ \psi_y \end{bmatrix} \tag{3.2}$$

The electric field components along the x and z axes are expressed in terms of

SVEA fields as Eqs. (3.3) and (3.4)

$$\frac{\partial^2 E_x}{\partial z^2} = \left[\frac{\partial^2 \psi_x}{\partial z^2} - 2in_0k_0z\frac{\partial \psi_x}{\partial z} - n_0^2k_0^2\psi_x\right] e^{-in_0k_0z} \tag{3.3}$$

$$\frac{\partial^2 E_y}{\partial z^2} = \left[\frac{\partial^2 \psi_y}{\partial z^2} - 2in_0k_0z\frac{\partial \psi_y}{\partial z} - n_0^2k_0^2\psi_y\right] e^{-in_0k_0z} \tag{3.4}$$

The equations for slowly varying fields ψ_x and ψ_y are obtained by introducing the above expansions Eqs. (3.3) and (3.4) into the Maxwell's equation.

$$\frac{\partial^2\psi_x}{\partial x^2}+\frac{\partial^2\psi_x}{\partial y^2}+\frac{\partial^2\psi_x}{\partial z^2}-2in_0k_0z\frac{\partial\psi_x}{\partial z}+\frac{\partial}{\partial x}\left[\frac{1}{n^2}\frac{\partial n^2}{\partial x}\psi_x+\frac{1}{n^2}\frac{\partial n^2}{\partial y}\psi_y\right]+k_0^2(n^2-n_0^2)\psi_x=0 \tag{3.5}$$

$$\frac{\partial^2\psi_y}{\partial x^2}+\frac{\partial^2\psi_y}{\partial y^2}+\frac{\partial^2\psi_y}{\partial z^2}-2in_0k_0z\frac{\partial\psi_y}{\partial z}+\frac{\partial}{\partial x}\left[\frac{1}{n^2}\frac{\partial n^2}{\partial x}\psi_x+\frac{1}{n^2}\frac{\partial n^2}{\partial y}\psi_y\right]+k_0^2(n^2-n_0^2)\psi_y=0 \tag{3.6}$$

Eqs. (3.5) and (3.6) are expressed in terms of slowly varying fields ψ_x and ψ_y instead of E_x and E_y. The slowly varying envelope approximation neglects the second order derivative of ψ_x and ψ_y for the z coordinate, i.e.:

$$\left|\frac{\partial^2\psi_x}{\partial z^2}\right| \ll 2n_0k_0\frac{\partial\psi_x}{\partial z} \tag{3.7}$$

$$\left|\frac{\partial^2\psi_y}{\partial z^2}\right| \ll 2n_0k_0\frac{\partial\psi_y}{\partial z} \tag{3.8}$$

The physical meaning of the SVE approximation is shown in the Fig. 3.1 where the oscillation of the optical field is very fast as a function of the propagation distance z axis whereas the amplitude of the envelope varies very slowly. The full vectorial BPM equations (also known as the paraxial wave equations) are obtained by applying the SVEA to Eq. (3.5) and Eq. (3.6). The basic full vectorial BPM equations are provided by the Eqs (3.9) and (3.10).

$$2in_0k_0\frac{\partial\psi_x}{\partial z} = \frac{\partial^2\psi_x}{\partial x^2}+\frac{\partial^2\psi_x}{\partial y^2}+\frac{\partial}{\partial x}\left[\frac{1}{n^2}\frac{\partial n^2}{\partial x}\psi_x+\frac{1}{n^2}\frac{\partial n^2}{\partial y}\psi_y\right]+k_0^2(n^2-n_0^2)\psi_x \tag{3.9}$$

$$2in_0k_0\frac{\partial\psi_y}{\partial z} = \frac{\partial^2\psi_y}{\partial x^2}+\frac{\partial^2\psi_y}{\partial y^2}+\frac{\partial}{\partial y}\left[\frac{1}{n^2}\frac{\partial n^2}{\partial x}\psi_x+\frac{1}{n^2}\frac{\partial n^2}{\partial y}\psi_y\right]+k_0^2(n^2-n_0^2)\psi_{y\eta} \tag{3.10}$$

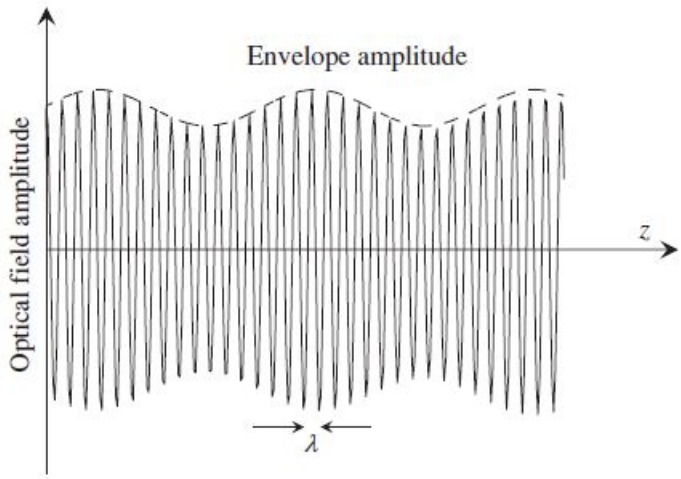

Figure 3.1: *Fast optical field amplitude variation along the propagation z axis and slowly varying envelope amplitude (dashed line), taken from [66]*

3.2 Scalar beam propagation

The scalar beam propagation equation is derived from the full vectorial beam propagation equations. Here, the refractive index gradient along the transverse direction was neglected because of the small contrast, i.e.,

$$\frac{\partial n^2}{\partial x} \approx 0 \tag{3.11}$$

$$\frac{\partial n^2}{\partial y} \approx 0 \tag{3.12}$$

The obtained scalar beam propagation equation is provided in Eq. (3.13).

$$2in_0k_0\frac{\partial u}{\partial z} = \frac{\partial u^2}{\partial x^2} + \frac{\partial u^2}{\partial y^2} + k_0^2(n^2 - n_0^2)u \tag{3.13}$$

where u is the transverse optical field which could either be electric or magnetic. The scalar approach is suitable for weakly guiding waveguiding structures, where the derivative of the optical field is assumed to be continuous at all the boundaries.

3.2.1 Finite Difference (FD) approach on BPM

In the FD approach, the spatial domain of the transverse plane $L_x \times L_y$ is discretized into a mesh region having $N_x \times N_y$ discrete points. The mesh has a

grid spacing of Δx and Δy, where $\Delta x = L_x/(N_x - 1)$ and $\Delta y = L_y/(N_y - 1)$. A coordinate point $(x_j), (y_j)$ is a generic point (i, j) in the transverse plane where $x_i = i\Delta x = iL_x/(N_x - 1)$ and $y_j = j\Delta y = jL_y/N_y - 1$. The computational domain should be wide enough to describe all the propagating modes within the photonic device. The longitudinal dimension is also discretized with the spacing of Δz, where $z = m\Delta z$. The transversal field in the (x, y) plane is known at

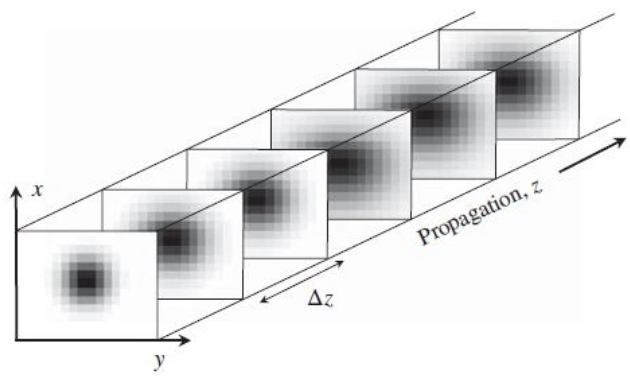

Figure 3.2: *The BPM algorithm is applied to determine the field at the $z + \Delta z$ plane when the discretized field at the transversal plane at position z is known already [66].*

one z plane for the 3 dimensional FD-BPM case. The goal is to determine the optical field in the next z plane at $z+dz$, as shown in Fig. 3.2 when the field at z is already known. The process is then repeated for the whole photonic structure and the calculation of the optical filed and the BPM were realized through several discrete steps. In the scope of this research work, the 2-dimensional scalar FD-BPM was adopted which was the simplest scenario that allowed us to simulate planar optical waveguides in two coordinates in (x, z) directions. Only one field component was used to describe the light distribution within the structure. Here, the computation grid along the transverse x direction was divided into N discrete points. The field at a point location z is defined by one 1 dimensional array of N elements, as shown in Fig. 3.3. The scalar wave equation for 2D structures is provided in Eq. (3.14).

$$2in_0k_0\frac{\partial u(x,z)}{\partial z} = \frac{\partial u(x,z)^2}{\partial x^2} + k_0^2(n^2 - n_0^2)u(x,z) \tag{3.14}$$

$u(x, z)$ is the optical field whose derivative was assumed to be continuous at all boundaries.

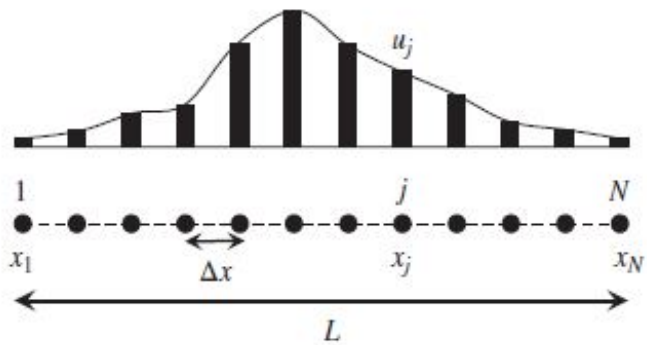

Figure 3.3: *The field along the transverse direction (x), for a fixed longitudinal coordinate z on a linear grid for the 2D FD-BPM. u_j is the optical field at position x_j. The x-axis is discretized into N discrete points and Δx is the step size.*

3.2.2 Crank-Nicolson(CN) Scheme

The Crank-Nicolson scheme is based on the finite difference approach that is unconditionally stable and also provides more accurate solutions. This scheme is a linear combination of the forward difference method and the backward difference method. In the FD approach, the partial derivative with respect to z can be written in the discretized domain as in Eq. (3.15).

$$\frac{\partial u}{\partial z} = \frac{u_j^{m+1} - u_j^m}{\Delta z} \tag{3.15}$$

u_j^m is the optical field at position $(j\Delta x, m\Delta z)$ with the j value ranging from $j = 1, 2, 3, ...N$. The second derivative of the optical field is denoted by

$$\frac{\partial u^2}{\partial x^2} = \frac{u_j^{m+1} - u_j^m}{\Delta z} \tag{3.16}$$

The scalar paraxial equation, Eq. (3.17), was obtained by inserting the Eq. (3.15) and Eq. (3.16) in the Eq. (3.14).

$$2in_0k_0\frac{u_j^{m+1} - u_j^m}{\Delta z} = \frac{u_{j-1}^m - 2u_j^m + u_{j+1}^m}{\Delta x^2} + k_0^2((n_j^m)^2 - n_0^2)u_j^m \tag{3.17}$$

The field value u_j^{m+1} at the position $z + \Delta z$ is calculated by knowing the field values from the earlier position z in the forward difference method that is also known as the explicit scheme. The stability condition for the explicit scheme

is mentioned below in Eq. (3.18). One of the drawbacks of the explicit scheme is that the value of Δz should be very small to confirm the numerical stability.

$$\Delta z \leqslant (\Delta x)^2 n_0 \pi / \lambda \tag{3.18}$$

The implicit or the backward finite difference scheme evaluates the field at the previous grid point by using the field values from the next step at $z + \Delta z$. The scalar paraxial wave equation in the backward difference scheme is expressed in Eq. (3.19).

$$2in_0k_0 \frac{u_j^{m+1} - u_j^m}{\Delta z} = \frac{u_{j-1}^{m+1} - 2u_j^{m+1} + u_{j+1}^{m+1}}{\Delta x^2} + k_0^2((n_j^{m+1})^2 - n_0^2)u_j^{m+1} \tag{3.19}$$

This implicit scheme allows longer propagation steps Δz during the field computation. However, there was a compromise on the numerical accuracy due to more dissipation. As already mentioned, the Crank Nicolson scheme is derived both from the forward difference scheme and backward difference scheme. So, The finite difference Crank Nicolson paraxial scalar wave equation Eq. (3.20) was obtained by multiplying $(1-\alpha)$ to Eq. (3.17) and α to Eq. (3.19) and finally adding them both. α is the contribution factor from both forward and backward scheme whose value is always considered between $0 \leq \alpha \leq 1$.

$$\begin{aligned} u_j^{m+1} \times \frac{2in_0k_0}{\Delta z} - u_j^m \times \frac{2in_0k_0}{\Delta z} - \frac{1-\alpha}{\Delta x^2}\left[u_{j-1}^m - 2u_j^m + u_{j+1}^m\right] \\ -\frac{\alpha}{\Delta x^2}\left[u_{j-1}^{m+1} - 2u_j^{m+1} + u_{j+1}^{m+1}\right] - k_0^2(1-\alpha)\left[(n_j^m)^2 - n_0^2\right]u_j^m \\ -\alpha k_0^2\left[(n_j^{m+1})^2 - n_0^2\right]u_j^{m+1} = 0 \end{aligned} \tag{3.20}$$

The Eq. (3.20) can be re-arranged as below:

$$\begin{aligned} -\frac{\alpha}{\Delta x^2}u_{j-1}^{m+1} + \left[\frac{2\alpha}{\Delta x^2} + \frac{2in_0k_0}{\Delta z} - \alpha k_0^2\left(n_j^{m+1})^2 - n_0^2\right)\right]u_j^{m+1} - \frac{\alpha}{\Delta x^2}u_{j+1}^{m+1} \\ = \frac{1-\alpha}{\Delta x^2}\left[u_{j-1}^m + u_{j+1}^m\right] + \left[\frac{2in_0k_0}{\Delta z} - \frac{2(1-\alpha)}{\Delta x^2} + k_0^2(1-\alpha)(n_j^m)^2 - n_0^2\right]u_j^m \end{aligned} \tag{3.21}$$

The new derived Eq. (3.21) is now compared to the standardized form in the Eq. (3.22).

$$a_j u_{j-1}^{m+1} + b_j u_j^{m+1} + c_j u_{j+1}^{m+1} = r_j \tag{3.22}$$

So, the coefficients from the Eq. (3.22) are expressed for the 2 dimensional

CN BPM scheme in the Eq. (3.23).

$$a_j = -\frac{\alpha}{\Delta x^2} \tag{3.23a}$$

$$b_j = \frac{2\alpha}{\Delta x^2} + \frac{2in_0k_0}{\Delta z} - \alpha k_0^2\left(n_j^{m+1})^2 - n_0^2\right) \tag{3.23b}$$

$$c_j = -\frac{\alpha}{\Delta x^2} \tag{3.23c}$$

$$r_j = \frac{1-\alpha}{\Delta x^2}\left[u_{j-1}^m + u_{j+1}^m\right] + \left[(1-\alpha)k_0^2((n_j^m)^2 - n_0^2) - \frac{2(1-\alpha)}{\Delta x^2} + \frac{2in_0k_0}{\Delta z}\right]u_j^m \tag{3.23d}$$

The set of Eqs. (3.23) form a tridiagonal system of N linear equations, where $N = 0, 1, 2, 3, ...j$. The set of equations in Eq. (3.23) were implemented in MATLAB to obtain the field values along 2D waveguides by using special finite difference based CN scheme. The CN-BPM is unconditionally stable for value $\alpha > 0.5$ and provides the most valid solution in adverse conditions of refractive index variation. The propagation of the field is stable even for large propagation steps.

3.3 Transparent boundary condition (TBC)

A reasonable boundary condition is essential for the BPM algorithm to optimally describe the optical propagation. The CN BPM scheme requires the field values u_0, u_{N+1}, those are outside the computational domain at the boundaries when $j = 1$ and $j = N$. To obtain the solutions from the CN-BPM scheme, the coefficients mentioned in the Eq. (3.23) need to calculated. For example, the value of the coefficients at a boundary, b_j and r_j when $j = N$ required the field value u^{N+1} in order to obtain solution. The field values are not known at these points, however it is essential to calculate the fields at these interior points. There are other popular boundary conditions, such as the Dirichlet and the Neumann. When these boundary conditions were applied along the CN-BPM method to photonic devices, optical reflections are induced from the surrounding boundaries. They imposed a condition such as null field at the boundaries which is not a realistic approach for our model. A fringe pattern was observed in the simulation due to interference between the reflected field from the boundaries with the propagating field. For this reason, a special boundary condition as the transparent boundary condition known was required for the CN-BPM scheme to carry out the optical simulation [72]. The TBC algorithm simulates a non-existent boundary condition, i.e., it effectively allows

the radiation to pass freely through the computational window walls without any back reflections from them. Basically, the implementation of the TBC is problem independent as it does not involve any adjustable parameter. It is very well applied to waveguide photonic structures and can be easily coupled with the Crank-Nicolson finite difference scheme in both 2D and 3D. This was the first known algorithm applied to the parabolic beam propagation equation. TBC was based on the assumption of the exponential behaviour of the field near the boundary. The field at the boundary u_N^m should fulfill the following condition before the start of next $m+1$ simulation step.

$$\frac{u_N^m}{u_{N-1}^m} = \frac{u_{N-1}^m}{u_{N-2}^m} = e^{ik_x\Delta x} \tag{3.24}$$

One could determine the value of k_x after the mth step by using two interior points near the boundary. This value of k_x will be used to fix the boundary condition at the $m+1$ propagation step, Eq. (3.25) .

$$u_N^{m+1} = u_{N-1}^{m+1} \times e^{ik_x\Delta x} \tag{3.25}$$

In this case, the real part of the k_x was restricted to be positive which will ensure only the outflow but no back-reflection from the computation window walls.

When the real part of k_x was negative, its value was reset to zero and the boundary field was re-calculated by using the corrected k_x value. The TBC condition was implemented for lower boundaries of the simulation domain as well. The field at the lower boundary u_1^m should fulfill the following condition before the start of $m+1$ simulation step.

$$\frac{u_2^m}{u_1^m} = \frac{u_1^m}{u_0^m} = e^{ik_x\Delta x} \tag{3.26}$$

The value of k_x after the mth step is determined by using two interior points near the boundary. Then its value of k_x is used to fix the boundary condition at the $m+1$ propagation step, Eq. (3.27). We observed accurate, robust and efficient simulations by using the TBC boundary condition for CN-BPM scheme in 2 dimension.

$$u_1^{m+1} = u_2^{m+1} \times e^{ik_x 2\Delta x} \tag{3.27}$$

3.4 Validation of CN-BPM implementations with commercial software RSoft

Various LWL structures, such as straight waveguides, Y-branches, bent waveguides and Mach-Zehnder interferometers were modelled in MATLAB. Similar

LWL structures having the exact dimensions as the MATLAB models were designed in the commercial tool RSOFT. RSOFT allows the design and simulation of waveguides, other active or passive photonic or optoelectronic devices for optical integrated circuits, accurately and quickly. They enable various innovations in the field of sensing, optical data communications, imaging and silicon photonics. The optical simulations were carried out by using the implemented research tool comprising the CN-BPM algorithm with the transparent boundary condition. Also, the optical simulations were performed by using the RSOFT software. The obtained propagated beam intensities from the CN-BPM scheme and the commercial software RSOFT were compared for each and every LWL structure to validate the implementations.

3.4.1 Design and simulation of LWL structure - Straight Waveguide

In an initial step, a straight waveguide was modelled both in MATLAB and the commercial tool RSOFT. The dimensions of the waveguide along the transverse x and propagation z directions were fixed to the same value 39.95 µm. Then the x axis was discretized to $N_x = 800$ points. The number of discretized points along the propagation z direction was set to $N_z = 800$. Other two important parameters, wave number $k_0 = 5.636$ and effective refractive index $n_{eff} = 2.1514$ were considered for the simulations. One initial input Gaussian beam excitation was provided to the middle point in the computation domain along the x axis and then the BPM simulation was carried out, as shown in Fig. 3.4.

A gradient refractive index distribution was considered where the difference in refractive index between the core and cladding part of the waveguide was $\Delta n = 0.03$. The refractive index profile of the straight waveguide is provided in the Fig. 3.5. A gradual variation in the refractive index value from the core part $n_{core} = 2.153$ to the cladding part $n_{clad} = 2.15$ was achieved. The input inlet of the 1D Gaussian excitation beam was fixed at the point $x = 20$ µm. Then the beam was propagated and the beam intensity profile was obtained after the simulation, as shown in the Fig. 3.6. The model was then replicated in the RSOFT tool by keeping all dimensions equal as the Matlab model. The intensity profile was obtained by simulating the propagating beam through it. The obtained result is shown in the Fig. 3.7. The normalized power was monitored during the simulation for later comparison. The output beam intensity profiles from the exit port of the straight waveguide are extracted from the CN-BPM scheme and then compared with the obtained output beam

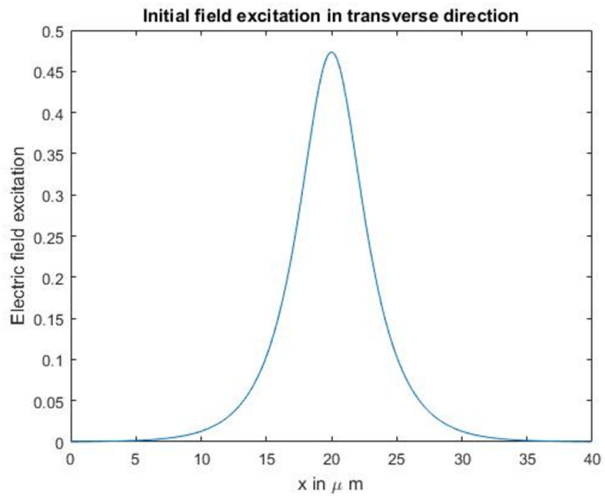

Figure 3.4: *Input Gaussian beam excitation to the straight waveguide.*

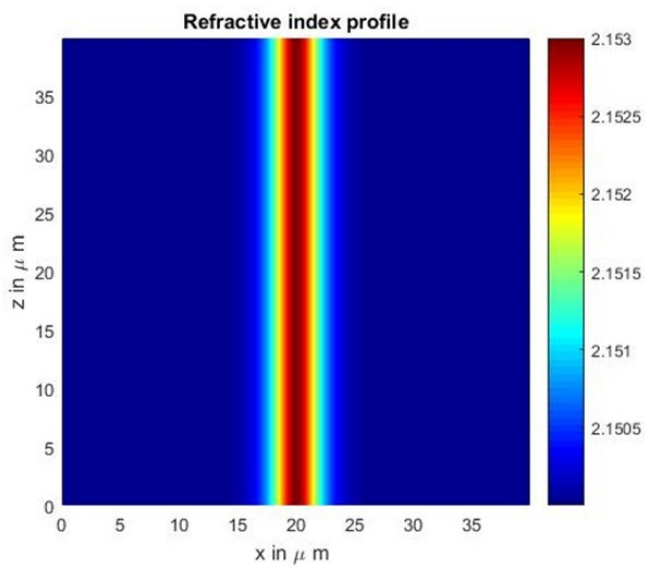

Figure 3.5: *Gradient refractive index profile of the straight waveguide.*

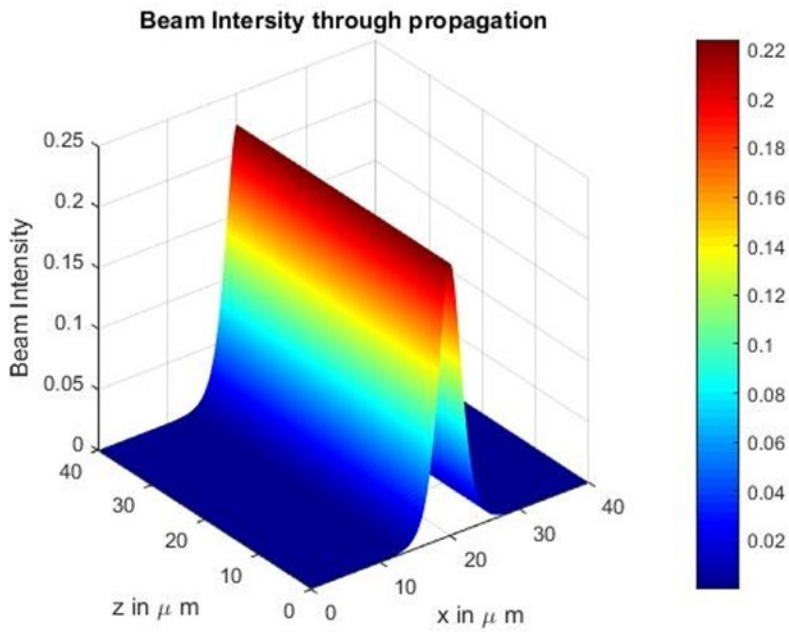

Figure 3.6: *Beam intensity while propagating the Gaussian beam through the straight waveguide using CN-BPM scheme.*

intensity profile from the RSOFT tool. The comparison result is provided in the Fig. 3.8, which showns a very god agreement between the intensity profiles (follow the same pattern) although different simulation mechanisms were adapted for them.

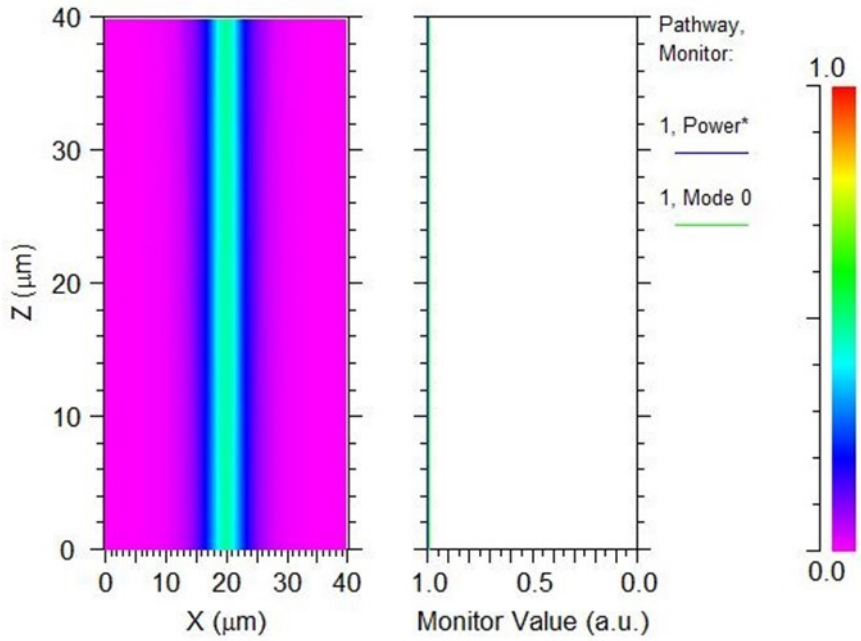

Figure 3.7: *Beam intensity profile while propagating a Gaussian beam through the straight waveguide in RSOFT.*

3.4.2 Design and simulation of bent waveguides

A cosine bent waveguide was designed both in Matlab and in the commercial tool RSOFT. The size of the x-window was fixed to $0 - 39.95\,\mu\text{m}$. A similar z window length was considered between $0 - 39.95\,\mu\text{m}$. The transverse and propagation window domains were represented by discretized points in such a way, that $N_x = 800$ and $N_z = 800$. Other important parameters $k_0 = 4.05$ and $n_{eff} = 3.3576$ were considered to perform the CN-BPM simulation. Two guided modes were propagated within the cosine bent and the input beam profile of the excitation Gaussian beam is shown in the Fig. 3.9. The refractive index for the cosine bent had a step index profile where the core part had a refractive index value of $n_{core} = 3.36$ and the refractive index of the cladding part was fixed to $n_{clad} = 3.3$. The corresponding refractive index profile and

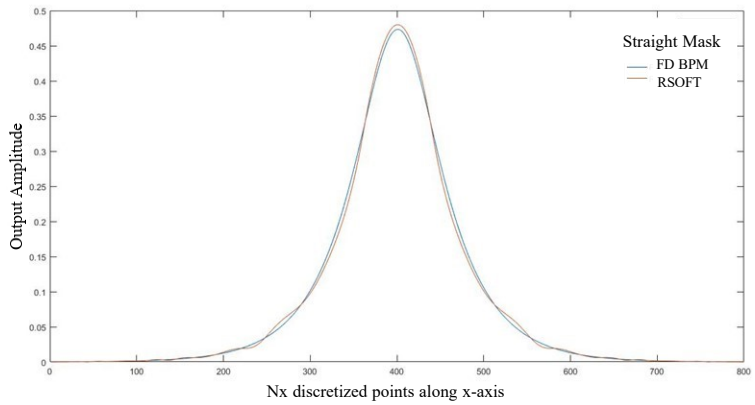

Figure 3.8: *Output intensity amplitudes are compared between CN-BPM scheme and RSOFT tool for simulating of a straight waveguide.*

the obtained beam intensity profile for the cosine bent waveguide design model is provided in the Fig. 3.10.

A cosine bent with the same dimension as the Matlab model was designed and simulated using the RSOFT tool. The obtained beam intensity profile and the corresponding monitored normalized power is shown in the Fig. 3.11. The output beam intensity profile from the CN-BPM simulation was compared with the output intensity profile obtained from the RSOFT simulation, shown in Fig. 3.12. The output beams from the two simulations follow nearly the same trend. However, one could observe some kind of fine tuning to the output beam profile in the RSOFT simulation which could be from a smoothing algorithm applied to the RSOFT simulation results, as seen the Fig. 3.12. The output amplitude of the beam from RSOFT simulation is smoother. The monitored normalized power when the beam was propagating through the cosine bent from the CN-BPM simulation is shown in the Fig. 3.13. Here, the normalized power was obtained by dividing the actual power at a particular z slice by the maximum input power. At the bending position, the amplitude of the propagating beam intensity is reduced both in the CN-BPM simulation and RSOFT simulation. The overall power of the beam is reduced at the output port after it was propgated through the cosine bent. However, the shape of the beam amplitudes at the output looks asymmetrical both in the CN BPM as well as in the RSOFT simulation. This could be due to change in beam profiles due to the presence of the bent and loss of propagating beam intensity in these cosine bents, in Fig. 3.12.

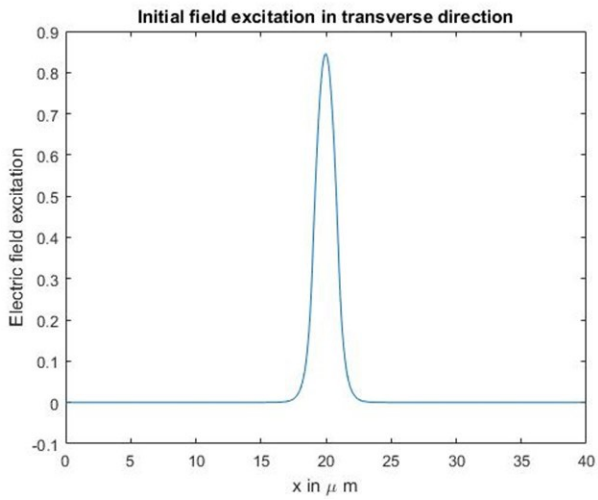

Figure 3.9: *The input Gaussian beam excitation to the bent waveguide.*

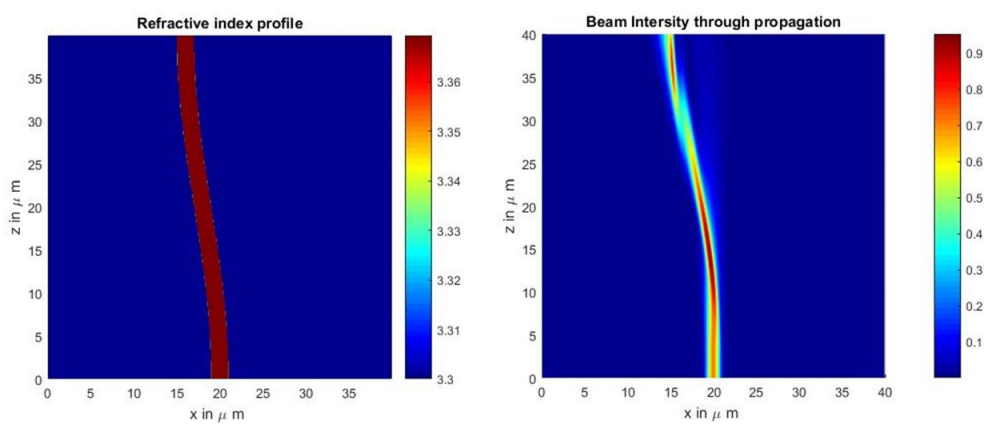

Figure 3.10: *The refractive index profile for the cosine bent and the corresponding beam intensity profile while propagating the Gaussian beam by using the CN-BPM scheme.*

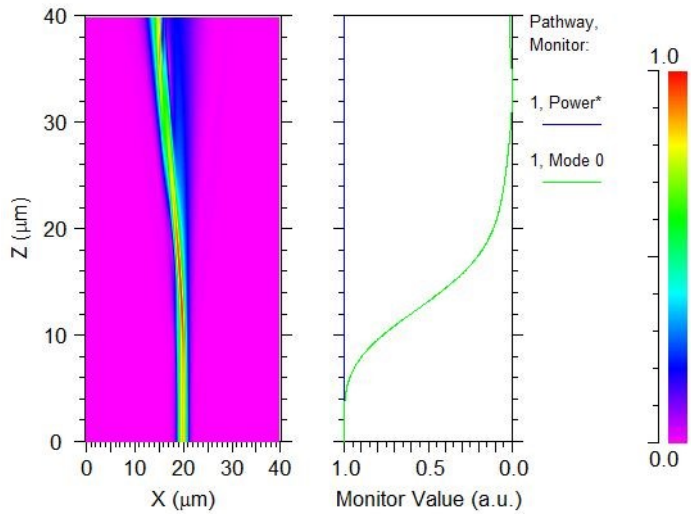

Figure 3.11: *Beam intensity profile while propagating a Gaussian beam through the cosine bent waveguide in RSOFT. The panel on the right side is the pathway monitor in RSOFT that shows the compressive calculation of monitored transmitted power of the propagating mode (green line). The normalized power is 1, shown by the blue line.*

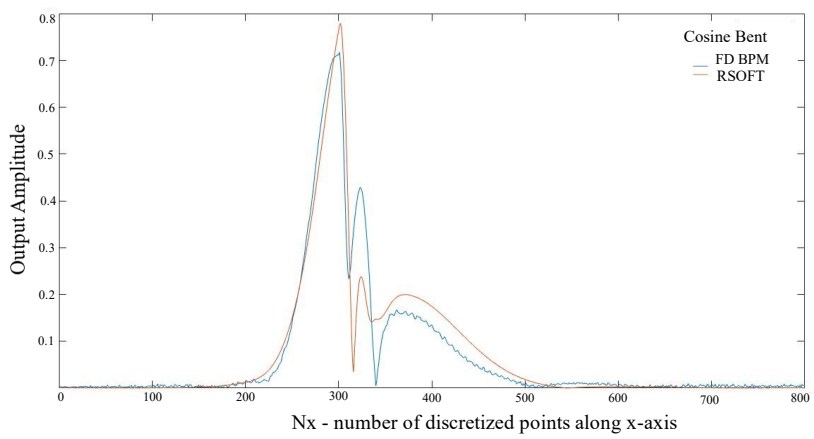

Figure 3.12: *Output intensity amplitudes are compared between the CN-BPM scheme and RSOFT tool while simulating a cosine bent waveguide.*

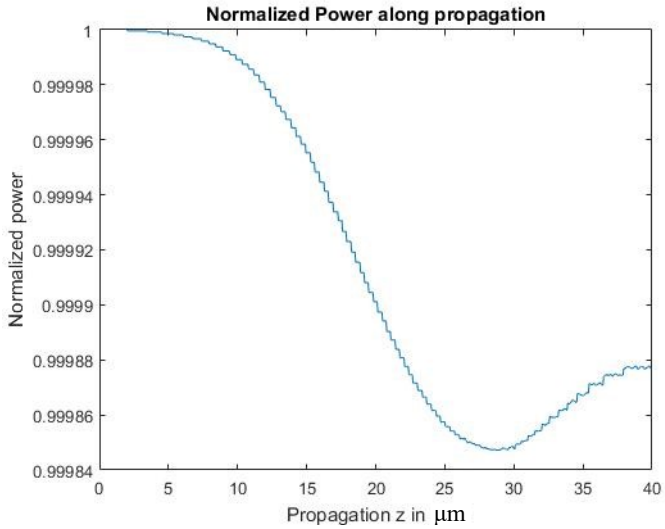

Figure 3.13: *The monitored normalized power by propagating a Gaussian beam through the bent waveguide from the CN-BPM simulations.*

3.4.3 Design and simulation of Y branches

Next, one Y-branch was modelled both in Matlab and RSOFT. The x window was kept smaller compared to the propagation z window in the computational space, i.e. $x = 0$ to 19.975 and $z = 0$ to 799.466. The discretized step size along x axis and z axis were fixed to $\Delta x = 0.025$ and $\Delta z = 0.533$, respectively. The discretization steps were determined in a way to obey the stability criteria for the CN-BPM scheme. The number of discretized points along the x, z windows were $N_x = 800$, $N_z = 1500$, respectively. The refractive indices of the Y-branch core and cladding were kept as $n_{core} = 3.36$, $n_{clad} = 3.3$. All the parameters are set only for the purpose to carry out simulations using CN-BPM scheme and RSOFT. Then, to compare their outcomes to validate the implementation for the beam propagation code. It is of course possible to consider other values for refractive indices, step size and computational domain size. The refractive index profile of the Y-branch is shown in the Fig. 3.14. The input excitation as a 1D Gaussian beam with two modes was provided to the Y-branch, see Fig. 3.15. The optical field intensity profile within the Y-branch after simulating by using the CN-BPM scheme in Matlab is shown in Fig. 3.16. Here, an oscillation in the amplitude of the transmitted beam is observed during simulation. The oscillations are generated due to the interactions of propagating modes within the Y-branch. Then the Y-branch

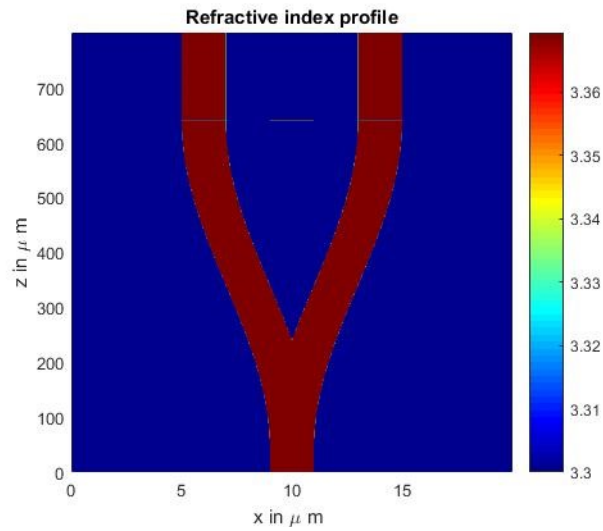

Figure 3.14: *The refractive index profile of the Y-branch.*

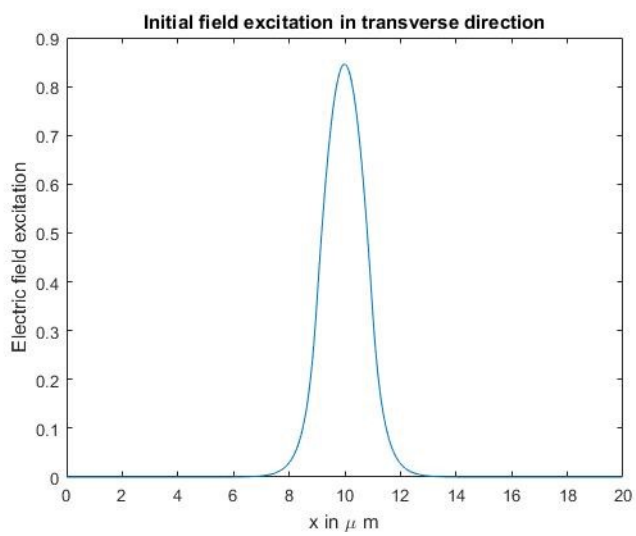

Figure 3.15: *The input Gaussian beam excitation along the transverse x-axis to the Y-branch.*

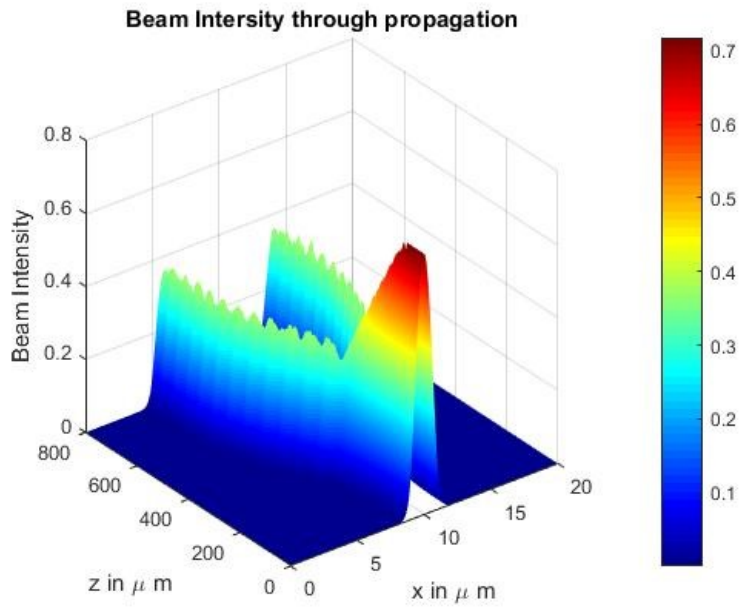

Figure 3.16: *The beam intensity profile of the Y-branch from the CN-BPM simulation.*

was modelled in RSOFT having the same dimension as the CN-BPM case. The simulation was performed by providing beam excitation to the middle core part of the Y-branch. The obtained beam intensity profile along with the monitored normalized power from RSOFT is depicted in the Fig. 3.17. The output beam intensity profiles were compared between BPM and RSOFT simulations, as in Fig. 3.18. The input fundamental mode was partitioned into two modes in the output branches. The output beam profiles which contains two mode was obtained both CN-BPM and RSOFT simulations. A comparison between the output beam intensity profiles was performed which is shown in the Fig. 3.18. The output modes from the CN-BPM simulation very well match with output modes from the RSOFT tool, and thus, validating the implementation of the CN-BPM algorithms with a commercial software RSOFT. The oscillation in the amplitude of the transmitted beam is also observed in RSOFT simulation which could be again due to mode field interactions during propagation. Although, the simulations match well with each other in Fig. 3.18, one could observe noise around the edges for CN-BPM simulation. Generally, the commercial tools tend to apply other algorithms to cancel out the noise to generate good visuals. The graph generated from RSOFT simulation has no noise around the edges of the output amplitude of beams.

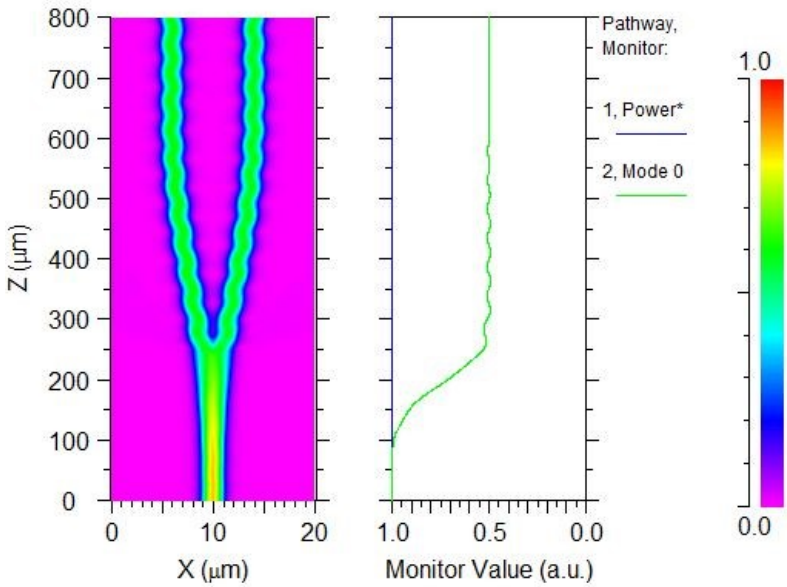

Figure 3.17: *The RSOFT simulation results for the Y-branch. The intensity beam profile and the corresponding monitored normalized power during simulation. The panel on the right side is the pathway monitor in RSOFT that shows the compressive calculation of monitored transmitted power of the propagating mode (green line). The normalized power is 1, shown by the blue line.*

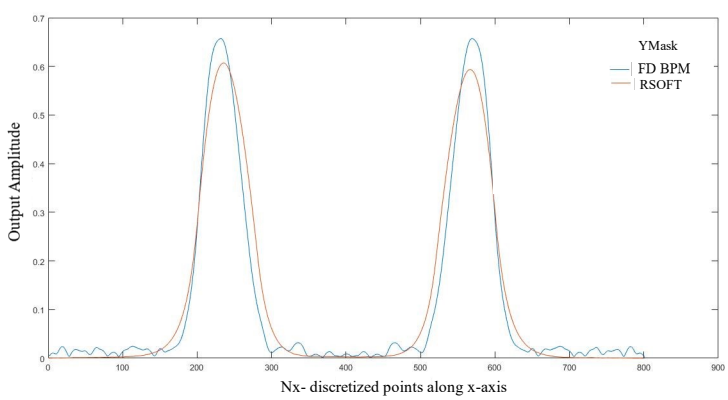

Figure 3.18: *The comparison between the obtained output modes in the beam intensity profiles from the CN-BPM and RSOFT simulations for the Y-branch.*

3.4.4 Design and simulation of Mach-Zehnder interferometers

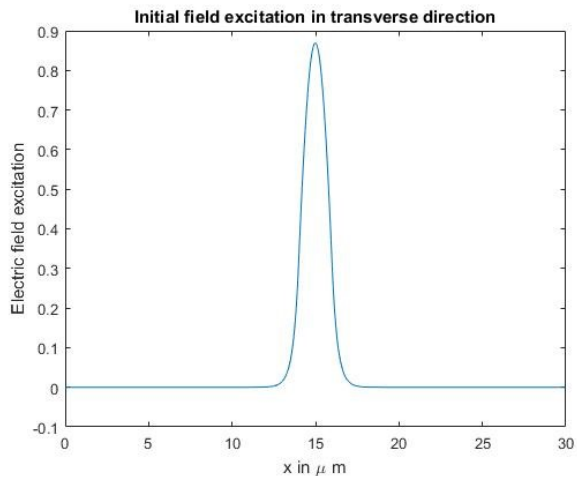

Figure 3.19: *The 1D Gaussian input beam excitation along the transverse x axis to the Mach-Zehnder interferometer.*

To validate further, a Mach-zehnder interferometer was modelled in Matlab and then simulated using the CN-BPM scheme. The fundamental mode was split and propagated in two arms and then merged into one source for the output in the Mach-zehnder interferometer. The device is generally used to determine the phase shift between two collimated beams. Here, the dimension of the x-window was fixed from 0 to 29.975 µm, that is then discretized into $N_x = 1200$ points. The dimension of the z-window was fixed from 0 to 2000 µm, where the total length along z-axis was discretized into $N_z = 4000$ points. $k_0 = 4.0537$ and $n_{eff} = 3.38$ were selected for the simulation. The values of the parameter were set to equal for RSOFT and CN-BPM simulations and then to compare the obtained simulation results. One could consider other values as well for initial assessment of CN-BPM implementation. Three guided modes were propagated within the Mach-Zehnder interferometer and an input 1 dimensional Gaussian excitation was applied at the centre point of the x-window at $z = 0$. The input Gaussian beam profile to the Mach-Zehnder interferometer is provided in the Fig. 3.19. A step index refractive index profile was selected for the interferometer. The refractive index difference between the core and the cladding part was kept at $\Delta n = 0.01$. The corresponding index distribution for it is shown in the Fig. 3.20. The beam intensity profile after simulation using the CN-BPM scheme is shown in the Fig. 3.21.

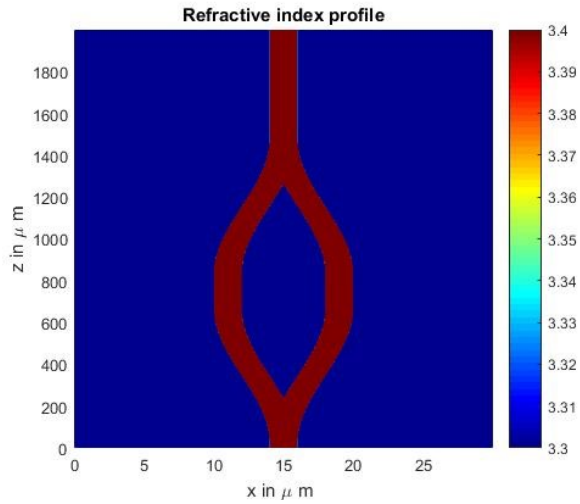

Figure 3.20: *The refractive index profile of the Mach-Zehnder interferometer in the (x, z) plane.*

The model was exactly replicated in the RSOFT tool. The dimensions as well as other parameters were kept the same as earlier CN-BPM simulation. The optical simulation was then carried out by the RSOFT. The field intensity profile and the monitor value of the normalized power during the propagation is shown in the Fig. 3.22. The oscillations in the amplitude of the transmitted beam are visible both in RSOFT and CN-BPM simulation results due to the interactions between the propagating mode fields, in Figs. 3.22 and 3.21. The output beam profiles after the completion of the simulations were compared between RSOFT and Matlab CN-BPM simulations and they also found to agree well with each other.

After modelling various photonic LWL structures both in RSOFT and Matlab and comparing their simulation results, the implemented CN-BPM scheme in Matlab was validated.

3.5 Parametrized study on bench-marking optical interconnects

Various scripts were implemented in Matlab to carry on a parametrized study on photonic components in this work. The mode mismatch loss, power attenuation, effective refractive index and number of guided modes were computed for them by using smaller code samples.

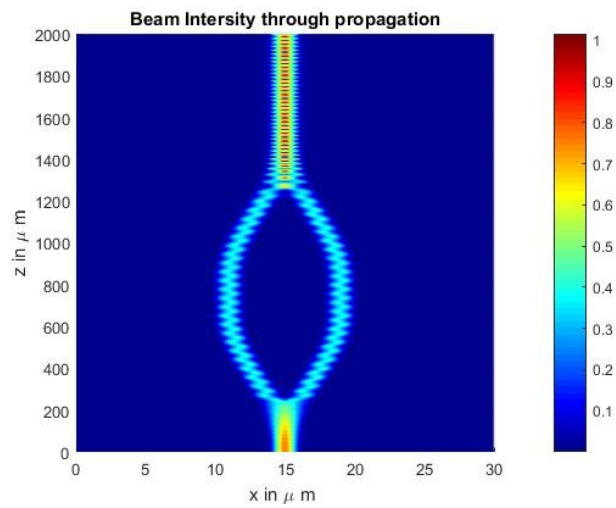

Figure 3.21: *The obtained intensity distribution after simulating the Mach-Zehnder interferometer using the CN-BPM scheme.*

3.5.1 Mode mismatch loss

The correlation function between the input optical field E_0 and the propagating field E_1 was computed by integrating the product of the input field E_0 component with the complex conjugate of the propagating field component E_1, i.e., correlation $= \int E_0 * \bar{E}_1$. The mode mismatch loss is often the coupling loss between the propagating modes with in the waveguide. This is based on the correlation function calculation. The mode mismatch loss between two propagating mode fields is calculated by using the equation $-10log\frac{\left|\int E_0 * \bar{E}_1\right|^2}{\left|\int E_0\right|^2}$. The equation was scripted in Matlab and for various different LWL photonic components the mode mismatch losses were calculated.

3.5.2 Power attenuation

The power attenuation is one important parameter needed to be calculated for LWL structures, such as bent waveguide, straight waveguide, Y-branch and Mach-zehnder interferometer. The input power $P(input)$ to the LWL structure was obtained by integrating the square of the input field, i.e., $P(input) = \int E_0^2$, where E_0 is the input optical field. The output power from the LWL structures were calculated by extracting the field value from the last slice at $z = nz$ and then integrating the square of that field value from the output. The output

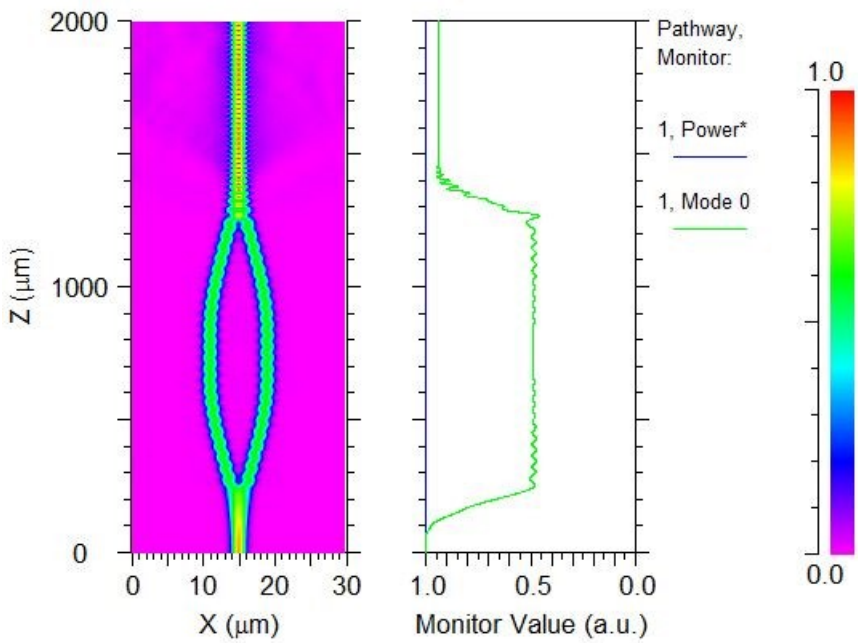

Figure 3.22: *The Mach-Zehnder interferometer was simulated using the RSOFT tool. The left side panel shows the beam intensity profile. The panel on the right side is the pathway monitor in RSOFT that shows the compressive calculation of monitored transmitted power of the propagating mode (green line). The normalized power is 1, shown by the blue line.*

power $P(output)$ is obtained via $P(output) = \int E_{nz}^2$, where E_{nz} is the optical field at the last slice at $z = nz$. Then, the power attenuation is calculated by $-10 \times log_{10} P(output)/P(input)$.

3.5.3 Effective refractive index and number of guided modes

Further scripts were implemented from Hertel [73] to calculate the effective refractive index n_{eff} and the number of guided modes within the waveguides. The mode parameter L was set up after computing two 1D components. The L parameter is a diagonal square matrix with the elements of vector components from two 1D components [73]. The eigenvalues and eigenvectors of the mode parameter L was computed. The obtained eigenvalue provided the effective refractive index value, n_{eff}. Only the eigenvectors with the eigenvalues $n_{eff} > n_b$ generated the number of guided modes propagating through the waveguide [73]. Here n_b is the base refractive index value. The script is used to obtain n_{eff} and guided modes for various photonic components. Ex. the Mach-zehnder interferometer shown in Fig. 3.21 has $n_{eff} = 3.38$ and 3 number of guided modes.

The above simulations of the photonic components using RSOFT and CN-BPM were carried out to confirm the validations of the implemented CN-BPM method, which was then further used to perform realistic other simulations of polymer waveguides to obtain the intensity distributions of beam profiles.

Chapter 4

Development of Material Models

The following chapter introduces the concept of self-written waveguides created by the combined self-focusing and self-trapping effects of a propagating beam within a material sample. A further discussion carried out to mark the various forms of SWWs, such as straight or bent SWW. Two different material models are presented that account for the refractive index modulation of the material sample. The material models are coupled with the CN-BPM scheme to demonstrate the change the SWW formations. Finally, the results obtained from both material models were compared by simulating a straight and bent SWW in them.

4.1 Self-Written Waveguides(SWWs)

A combined outcome of self-focusing and self-trapping effects of the light results in the creation of self-written waveguides. One of the very first reports of the self-writing process was in 1992, although the dynamics of the SWW was not completely understood at that point [74]. Later, Frisken et al. has performed a self-writing experiment in UV-cured epoxy and provided a profound understanding on SWWs [16]. Since then, many other experimental and theoretical studies have already been performed to understand the underlying self-writing phenomenon of light in photo-monomer as well as in photosensitive material media [63, 64, 19, 65, 75, 21].

An induced change in the refractive index occured when a laser beam propagates through the photo-monomer or photo-polymer material mixture. At the beginning, the laser beam diffracts freely which is then compensated at a later stage due to the induced increase in the refractive index along the beam propagation axis. The change in refractive index is greatly influenced

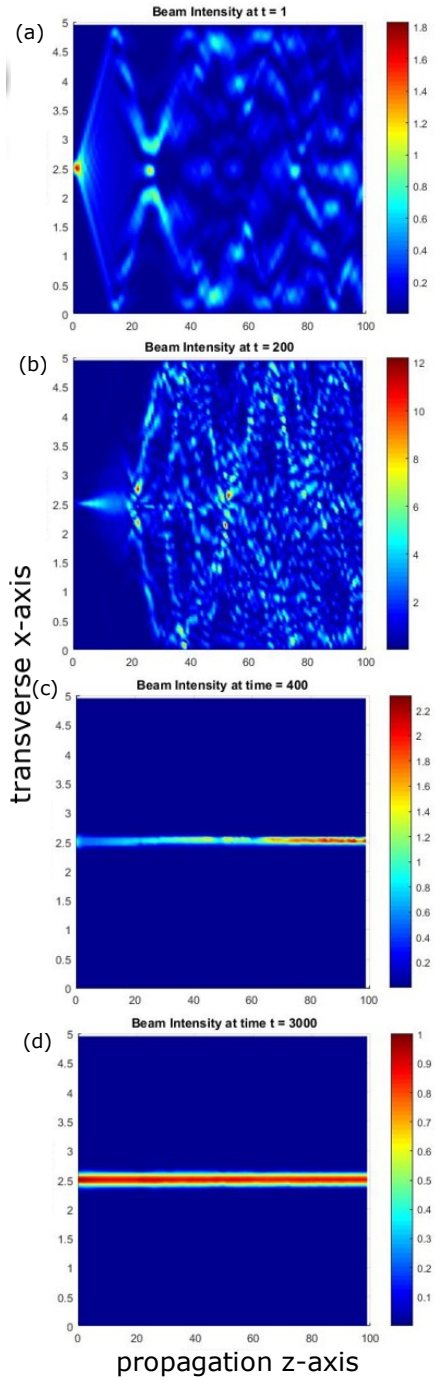

Figure 4.1: *The beam self clean-up in long distance propagation by using the phenomenological model. A Gaussian beam with a diameter of 250 μm propagated for a distance of 100 mm. (a) Input beam excitation, (b) A lot of diffraction with slight refractive index modulation at the beginning, (c) self-focusing of the beam, (d) complete beam self clean up happened and a permanent SWW is evolved.*

by the change in the intensity of the laser beam, i.e., the maxima of the refractive indices were located near the entry port of the Gaussian beam to the photo-monomer mixture resin, Fig. 4.1 (a). A lot of free diffraction of the beam is observed in Fig. 4.1 (b). The induced change in refractive index at a later stage becomes sufficient to completely self-trap and self-focus the optical beam, in Fig. 4.1 (c). Finally, a permanent optical channel is established, see Fig. 4.1 (d) . Once the channel is created, it remains within the medium even after the laser beam excitation is removed. It is then possible to propagate any optical beam of different wavelengths. This resulting optical channels are called self-written waveguides(SWWs) as they are created by the self-action of the light.

A single optical channel is created when one Gaussian beam is illuminated and propagated through the material. The single optical channel is often referred as a straight self-written waveguide [76, 77]. When two laser beams with misalignment or tilt along the transverse x or y direction are propagated into the material mixture, the two optical channels still merge and create a bent optical channel which is referred to as the bent self-written waveguide [65, 22]. The misalignment in bent SWWs is often referred to as the offset or gap between the two counter propagating laser beams. Such SWWs interconnects have potential applications in integrated photonic circuits as couplers. In our current case study, the photo-polymer mixture comprised of a monomer and a photoinitiator. Two material models were implemented for simulating the material properties for the evolving photo-polymer mixture. The monomer is polymerized in the exposed region that leads to the formation of a virtual core and cladding part of the SWW. The material models were then linked with the CN-BPM scheme to obtain the light distributions within the SWWs. The temporal dynamics of refractive index of the core and cladding part of the SWW was found by solving the material model equations. Then this new refractive index distribution profile is passed down to the CN-BPM scheme to compute the new field distribution for each time iteration.

4.2 Material model 1: Phenomenological model

The simple phenomenological model is already used by many groups to describe the self-writing phenomena in different material systems [76] [22] [75] [78] [23] [18]. It is also used in this thesis and adapted for our material case. In this material model, the refractive index directly changes with the change in the intensity of the laser beam where the evolution of refractive index of the material mixture approaches saturation. The analytical model was described by

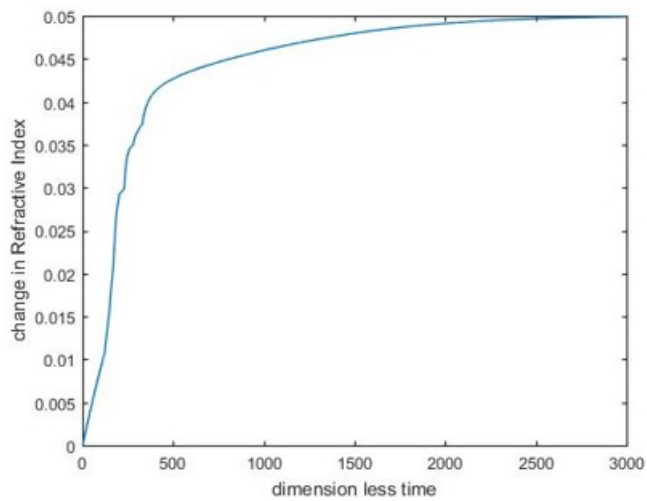

Figure 4.2: *The refractive index modulation during the beam clean-up process, that is shown in the Fig. 4.1. A Gaussian beam with a diameter of 250 µm was propagated for a distance of 100 mm. The simulation was performed for total of 3,000 time steps till complete evolution of the SWW.*

a simple first order differential equation Eq. 4.1, where the induced modification in refractive index of the material is influenced with the actinic beam intensity:

$$\frac{\partial \Delta n(x,z,t)}{\partial t} = A_s I(x,z,t)^p \left(1 - \frac{\Delta n(x,z,t)}{\Delta n_s}\right). \tag{4.1}$$

Here, Δn_s is the fixed saturation value in refractive index modulation, t is the elapsed exposure time, x is the transverse direction and z is the beam propagation direction. $\Delta n(x,z,t)$, is the regular updated value of the refractive index modulation and $I(x,z,t) = |u(x,z,t)|^2$ is the local exposing light intensity in each subsequent time step. $u(x,z,t)$ is the propagating optical field. p is the number of photons involved in the process that is typically assumed to be 1 for linear photo polymerization [19]. A_s is the real coefficient that depends upon the wavelength of light, material properties and number of photons p involved. The refractive index evolution approaches saturation (maximum possible modulation) during the simulation. This model is not based upon the physical description of the polymerization process, thus it is considered to be an approximate model, as explained in [19]. The phenomenological model does not describe the diffusion mechanism as well. One exemplary simulation result is provided where one Gaussian beam was propagated for long distance within

the material medium. The Gaussian beam had a diameter of 250 µm and it was propagated along the z direction for a distance of 100 mm. The self-clearance of dispersion and the corresponding beam clean-up during the simulation is very well observed in the simulation, see Fig. 4.1. The simulation was performed for total of 3,000 time steps, so that a completely evolved waveguide could be obtained at the end. The beam clean-up process could be achieved quicker when the propagating distance shorter, i.e. in the range of a few µm. The refractive index modulation during the beam clean-up process is shown in Fig. 4.2. In the simulations based on the phenomenological model one could observe a slow and steady increase in the refractive index value until the SWW is evolved completely and the dispersion of the beam is cleared out during the beam clean-up process.

4.3 Material Model 2: Diffusion model

The second material model employed in this thesis is the diffusion based material model that is more accurate in nature. The model has a more complex variation of refractive index that takes into consideration the individual re-distributions of mixture components within the material mixture. The concentration of polymer and monomer is influenced by the combined effect of the diffusion and polymerization process. The monomer is getting diffused from the darker region (without exposure to light) to the nearby brighter region (where the light is propagating) and is then converted into polymer chains. As a result, the process gives rise to a complex refractive index dynamics. The diffusion coefficient of polymers is neglected in the corresponding equation as they are too heavy to move around. The diffusion based material model was earlier proposed by Zaho et al. that described the effect of the ratio of the diffusion constant to the polymerization rate on the hologram formation for a sinusoidal illumination [79]. The diffusion model was further improved by Yariv's group [80] where it was applied to the holographic characterization of chain photopolymers. The above studies paved the way to conceptualize the investigation of self-written waveguides by using the diffusion-based material model. For the first time Kashin et al. [63] applied the diffusion model to determine the change in refractive index and showed a possibility of generating self-trapped beams within photo-polymer mixtures. Recently, Belgacem et al. [81] have demonstrated the influence of monomer diffusion on the interactions of light-induced SWWs using the diffusion material model. The concentration of monomer decreases and the concentration of the polymer increases in the illuminated region leading to the complex variation of refractive index of the

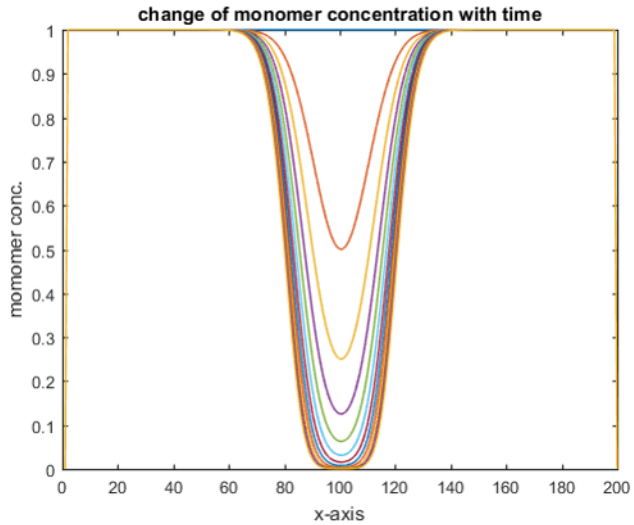

Figure 4.3: *The dynamics of the evolution of the monomer concentration profile in a temporal loop during numerical simulation. The temporal behaviour of the monomer concentration reflects the formation of a self-written waveguide in the region exposed to the writing light beam.*

material mixture during the simulation. The simulation started from an initial fixed monomer and polymer concentration. The dynamics of the refractive index of the material mixture evolved because of the corresponding change in the evolution of concentrations of individual components (monomer and polymer) during numerical simulation. The new light distributions within the SWWs was calculated from the dynamic value of the refractive index of the material and the process ends when the saturation of the refractive index value was achieved, i.e., $\Delta n = \Delta n_f$. Three partial differential equations are modelled and solved during the diffusion mechanism. The evolution of the concentration of the monomer is governed by Eq. (4.2).

$$\begin{aligned}\frac{\partial M(x,z,t)}{\partial t} =& \nabla(D\nabla M(x,z,t) - \\ & K_r M(x,z,t) I(x,z,t)\Big(1 - \frac{\Delta n(x,z,t)}{\Delta n_f}\Big)\end{aligned} \tag{4.2}$$

The diffusion coefficient for the polymer evolution was neglected (as mentioned above) as the polymer chains are too heavy to move around and the evolution

of the re-distribution of the polymer is described by Eq. (4.3).

$$\frac{\partial P(x,z,t)}{\partial t} = K_r M(x,z,t) I(x,z,t)\Big(1 - \frac{\triangle n(x,z,t)}{\triangle n_f}\Big). \tag{4.3}$$

In Eq. (4.2) and Eq. (4.3), M and P are the concentrations of monomer

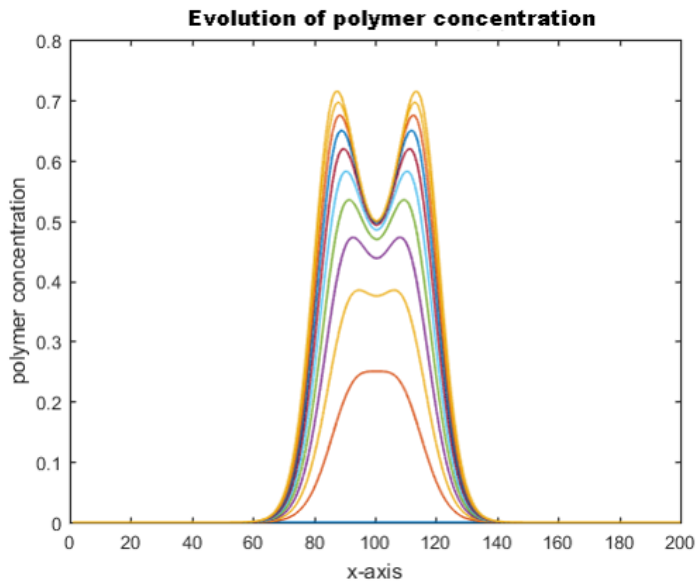

Figure 4.4: *The dynamics of evolution of polymer concentration profile in a temporal loop during the numerical simulation. The temporal behaviour of the polymer concentration reflects the formation of a self-written waveguide in the region exposed to the writing light beam.*

and polymer, respectively. The diffusion constant and the polymerization rate are denoted by D and K_r respectively. The first part of Eq. (4.2) describes the diffusion of the monomer with diffusion constant D and the second part of Eq. (4.3) explains the conversion of monomer to polymer chains. I is the light intensity and the maximum possible modulation in refractive index is denoted by Δn_f. The difference of refractive index values between the core and cladding is given by Δn. Here Δn is a dynamic value during the numerical simulation while writing a SWW.

The simulation shows that the value of Δn increased in every time step till the maximum possible modulation Δn_f was achieved. The maximum modulation in refractive index value $\triangle n_f$ during the simulation was equal to the difference in refractive index n_{max} and n_{min}. Here, n_{max} is the maximum

value of the refractive index of the mixture when all monomers are converted into polymer chains and n_{min} is the refractive index of the mixture at the beginning of the simulation prior to the conversion of monomer to polymer chains. The saturation of refractive index modulation is expressed by $\left(1-\frac{\triangle n(x,z,t)}{\triangle n_f}\right)$. The 2D Laplace operator is equal to $\nabla^2 = \frac{\partial^2}{\partial x^2} + \frac{\partial^2}{\partial z^2}$. By knowing the concentrations of polymer, monomer, and photoinitiator, their refractive index values, densities, and corresponding volume fractions are calculated for the individual mixture components. Then, the evolution of refractive index of the material mixture is calculated by using the Lorentz-Lorentz relation [82]:

$$\frac{n^2-1}{n^2+2} = \Phi_m \frac{n_m^2-1}{n_m^2+2} + \Phi_p \frac{n_p^2-1}{n_p^2+2} + \Phi_a \frac{n_a^2-1}{n_a^2+2}, \tag{4.4}$$

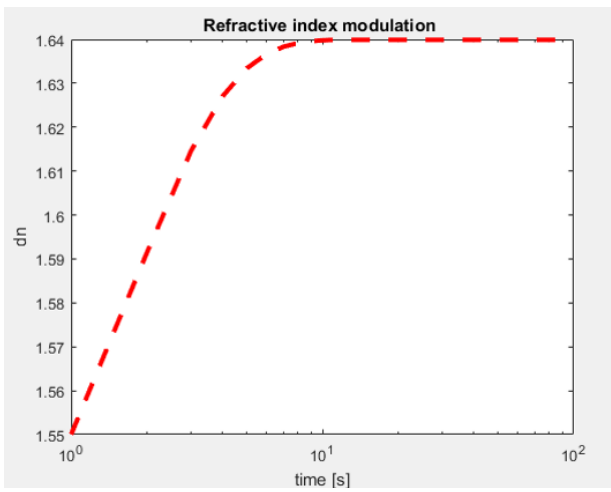

Figure 4.5: *The temporal dynamics of the refractive index modulation during numerical simulation (conducted for 100 s) in the diffusion model.*

The refractive indices of monomer, polymer and photoinitiator are denoted by n_m, n_p and n_a, respectively. Their corresponding volume fractions are Φ_m, Φ_p, and Φ_a. Φ_a is calculated from the conservation principle of total volume fraction, i.e., $\Phi_a = 1 - \Phi_m - \Phi_p$. The details of the calculation process are similar to the work of Babeva et al. [83]. In this model, the refractive index was modulated in a temporal loop until all monomers are converted into polymer chains. One initial simulation was carried out where the material mixture was considered to be made from 100% of monomer. The spatial distribution of monomer and polymer concentrations were obtained from the numerical

simulation results. The dependence of monomer and polymer concentrations profiles with respect to time are shown in Fig. 4.3 and Fig. 4.4. The initial monomer concentration was 1.

It was observed during the numerical simulation that the monomer concentration decreases to zero due to its depletion during the polymerization process, see Fig. 4.3. As per expectation, the concentration of polymer molecules is increased in a temporal loop, see Fig. 4.4. The growth was due to the accumulation of monomer coming into the illuminated region. However, because of the diffusion, the monomer does not have enough time to reach the spot centre and polymerized when close to the spot boundary. So, a dip was produced in the center of the polymer concentration profile. A W-shape concentration profile for the polymer was observed in its temporal dynamics. Also, a similar W-shape profile for the polymer concentration was observed in the two-way diffusion material model proposed by Babeva et. al [84]. There, the core part of the SWW is formed along the line in the illuminated region where the monomers are converted into polymer chains. So, the refractive index difference between the core and cladding was increased as the density of the material sample was increased along the beam propagation axis because of the accumulations of polymer chain. One exemplary simulation was carried out for 100 s and the corresponding temporal evolution of the refractive index modulation is shown in Fig.4.5.

4.4 Model Comparison

A straight SWW and bent SWW are simulated using both phenomenological model and diffusion-based material model. The difference in the numerical simulation results are observed with respect to the curing time, refractive index of the mixture and corresponding beam intensity profiles. Also, the minimum refractive index modulation required to obtain the optimal light guiding within the SWW for a fixed dimension is reported. The comparative study was carried out between the material model 1 (phenomenological model) and the material model 2 (diffusion model). The refractive index modulation and the intensity distributions for straight and bent SWWs are described.

4.4.1 Numerical parameters

To compare the implemented models, the simulation started from a homogeneous refractive index background for both model 1 and model 2. The change in the refractive index continues to increase in model 1 until Δn equals the

maximum possible value of the refractive index saturation Δn_s. Whereas in model 2, the refractive index change continued to grow in a temporal loop until all monomer was converted into polymer chains. The numerical parameters are kept equal between the models for comparison purposes. The initial homogeneous refractive index and the maximum achievable change in the refractive index modulation are also kept constant.

The simulations started from an uniform refractive index distribution with $n_0 = 1.5$ in the phenomenological model, model 1. The maximum possible change of refractive index was fixed at $\Delta n_s = 0.017$. The coefficient A was set to the value 1.2×10^{-3} [77]. The concentrations of material mixture components in the model 2 were selected in order to make sure that the maximum possible modulation in refractive index of the material mixture matches with the model 1 (phenomenological model). So, the simulation started with one photo-monomer mixture consisting of 40% monomer, 57% polymer, and 3% photoinitiator. The diffusion constant $D = 6 \times 10^{-15}$ m^2/s considered for the simulation that was measured experimentally in [85]. The polymerization rate K_r is fixed to 0.6 cm$^2/\mu$W. The refractive index of monomer n_m, polymer n_p, and photo-initiator n_a are set at 1.48, 1.52 and 1.46, respectively [81]. In both models, the waist of the Gaussian beam was considered 5 µm to illuminate the photopolymer material mixture. The bent SWW was created by propagating two Gaussian beams u_1 and u_2 from the input facets at $z = 0$ and $z = z_{max}$ through the material mixture. One needs to be cautious of the misalignment of the offset value while creating a bent SWW. For larger misalignment, the opposing beams will just bypass each other without any merging. However, only one Gaussian writing laser beam u_1 was needed to create a straight SWW by propagating it through the mixture. The Gaussian beam distributions are given by Eqs (4.5) and (4.6).

$$u_1(x, z = 0, t) = u_0 \exp\left(-\frac{x^2}{a^2}\right), \tag{4.5}$$

$$u_2(x, z = z_{max}, t) = u_0 \exp\left(-\frac{(x-d)^2}{a^2}\right). \tag{4.6}$$

Here d is the misalignment length or offset along the transverse direction x and a are the width of the input Gaussian beams for writing a bent SWW. The offset length d=5 µm was considered during simulation in both models. The beam with a width of a=5 µm was used for all the Gaussian beam excitations. The step increments along the propagation direction Δz and the transverse direction Δx were fixed as 1 µm and 0.5 µm and 0.5s, respectively for both models. The step increment Δt was kept to 0.5s. The selection of step size also satisfied the convergence criteria for the finite difference schemes. The choice

of time step is not independent of step size in finite difference discretization. The schemes eventually become unstable when there is an increase in time step keeping the mesh size fixed. The implemented equations had the stability criteria of $(D \times \Delta t)/min(\Delta x^2, \Delta z^2) \leqslant 0.5$. This is a critical number that depends on the space and time discretizations.

4.4.2 Comparison of the evolution of a bent SWW for the two models

Straight and bent waveguides are the basic blocks in integrated circuits. So, for convenience, basic coupling structures, a bent and a straight SWW are considered to verify the two models in order to test the accuracy of the simulations. A bent SWW was simulated using the phenomenological and diffusion material model, as shown in Figs. 4.6 and 4.7, respectively. The simulation started from a uniform refractive index background where $n = 1.5$ was considered in both models. In Figs. 4.6 and 4.7, the induced change in the refractive index of the material mixture and the corresponding beam intensity distribution profiles during the curing process are provided. The diffraction of the propagating beams is strongly compensated when the refractive index along their propagation axis slightly increases from the initial value of 1.5 and the optical connection is established in the overlapping region of the counter propagating beams, as in Figs. 4.6(a) and 4.7(a). Then the refractive index along the propagation axis was further increased to 1.502 at $t = 6 \times \Delta t$ in model 1 and at $t = 4 \times \Delta t$ in model 2. The widths of the propagating beams were reduced further due to the self-focusing effect in both models, as shown in Figs. 4.6(b) and 4.7(b), respectively. The connection or the bent coupler was completely established at this point.

However, there is a difference in the uniformity of smoothness among the models. The bent coupler created in the diffusion-based model has a more uniform surface, see Fig. 4.7(c). Some non-uniformity along the cross-section of the bent SWW is seen in the phenomenological model, in Fig. 4.6(c). When the refractive index modulation of the core of the bent SWWs is increased to the value 1.505 and beyond starting from the initial refractive index value 1.5 at $t = 8 \times \Delta t$ in the model 1 and at $t = 7 \times \Delta t$ in model 2, structures called primary eyes are observed to start moving along the propagation axis of the SWWs in both models. The primary eyes here are referred as the the maximum focus points in intensity distributions at a particular time instant. The movement of the primary eyes is an indication of good light guiding capabilities of the SWWs and the trajectories of the primary eyes are closely related to the SWW

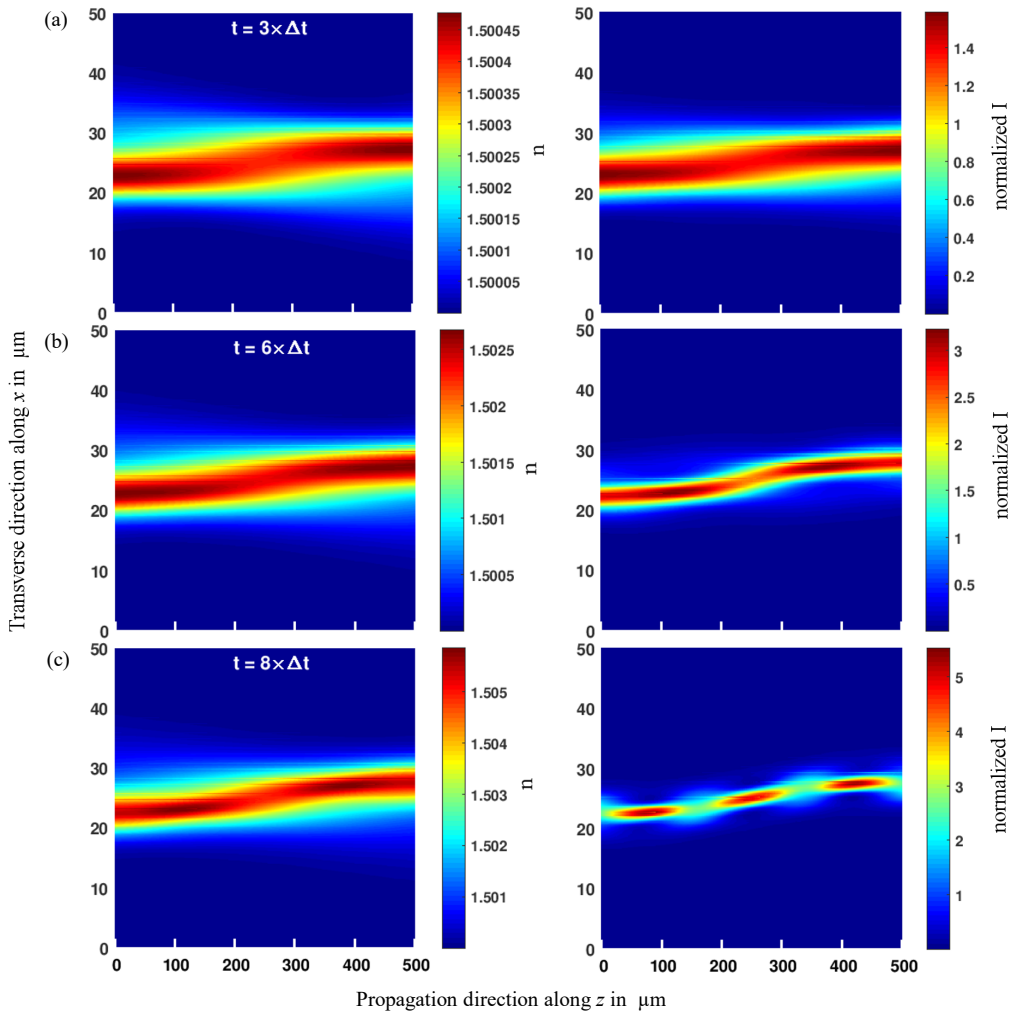

Figure 4.6: *Simulated bent SWW using the phenomenological material model. The refractive index modulation of the evolving core of the SWW is on the left side, the corresponding intensity distributions are on the right side. The intensity was normalized to the maximum intensity of the Gaussian input beam [86].*

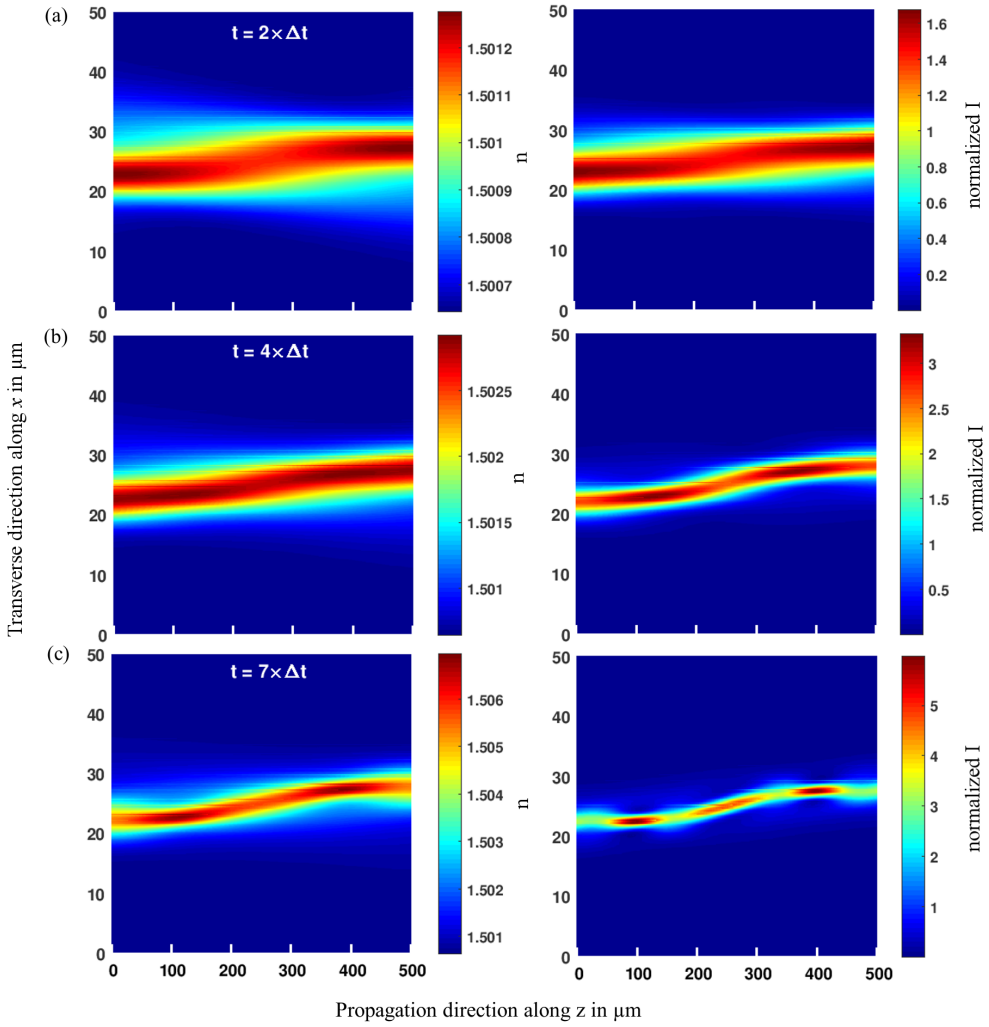

Figure 4.7: *Simulated bent SWW using the diffusion based material model. The refractive index modulation of the evolving core of the SWW is on the left side, the corresponding intensity distributions are on the right side. The intensity was normalized to the maximum intensity of the Gaussian input beam [86].*

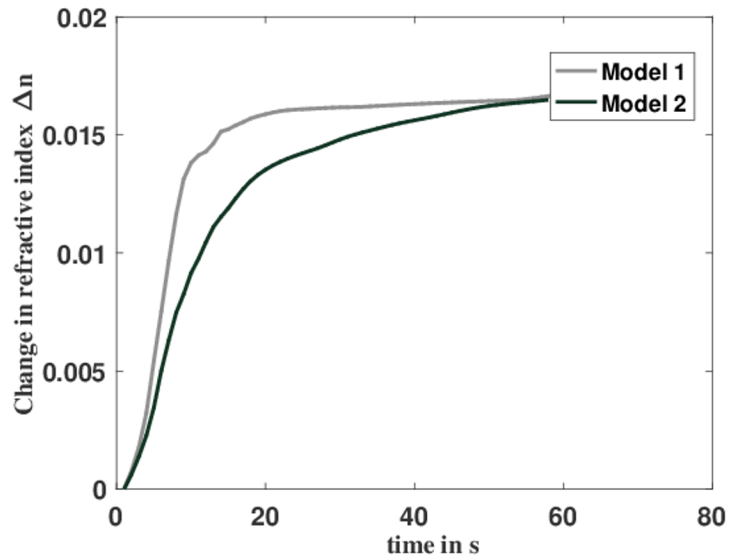

Figure 4.8: *The change in refractive index with the curing/writing time for a bent SWW obtained using model 1 and model 2, respectively.*

structures [18].

The bending in the curvature of the bent SWW is more prominent in the diffusion based material model, see Fig. 4.7(c) than in the phenomenological model, see Fig. 4.6(c). Also, the curing time was slightly less in the diffusion model compared to the phenomenological model. We could see the required refractive index modulation was achieved in fewer time steps in the model 2. Fig. 4.8 shows the change in the refractive index $\triangle n$ with respect to the curing time for both models. $\triangle n$ increases with time for both cases until the maximum saturation in refractive index was reached. The evolution of the change in refractive index from $\triangle n = 0$ to $\triangle n = 0.005$ is nearly the same for both models. Afterwards, a steeper or more sharp evolution in $\triangle n$ was observed for the model 2 than the model 1, see Fig. 4.8. A slight abrupt for the $\triangle n_{max}$ value was observed at $t = 15\,\mathrm{s}$ for model 1, whereas, the growth of $\triangle n$ was smoother for the model 2.

4.4.3 Comparison for the evolution of a straight SWW for different models

A straight SWW was modelled and simulated in using both models in order to test the accuracy of the simulations. Only one Gaussian beam having a

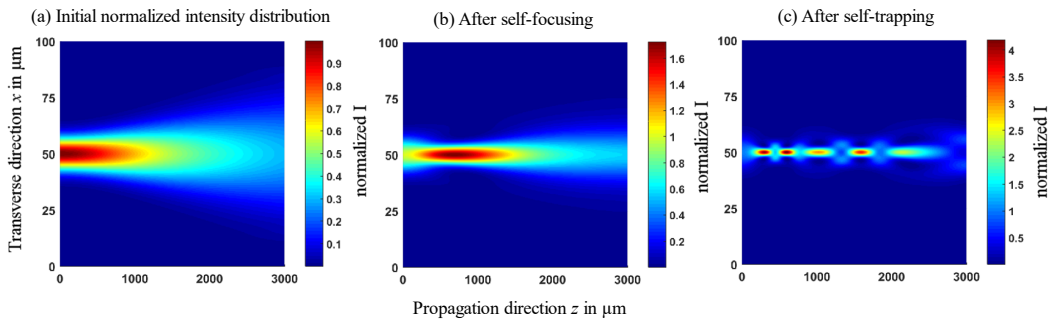

Figure 4.9: *Numerical simulation of a straight SWW within the given material mixture using the phenomenological model. (a) initial normalized light intensity distribution, (b) light intensity distribution after self-focusing of the Gaussian beam, and (c) light intensity distribution when the Gaussian beam is self-trapped [86]*

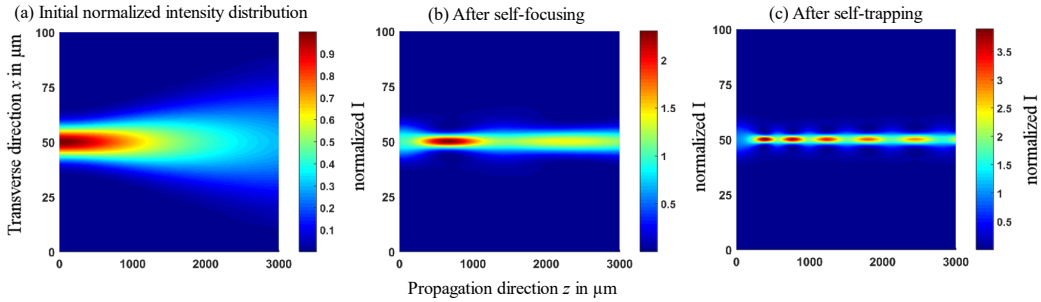

Figure 4.10: *Numerical simulation of a straight SWW within the given material mixture using the diffusion based material model. (a) initial normalized light intensity distribution, (b) light intensity distribution after self-focusing of the Gaussian beam, and (c) light intensity distribution when the Gaussian beam is self-trapped [86].*

beam width of $a = 5\,\mu\text{m}$ was traversed through the photo-polymer mixture to create the straight SWW. The maximum intensity of the initial input Gaussian beam was normalized to the value 1. The intensity profiles during the evolution process of a straight SWW from model 1 and model 2 are shown in Figs. 4.9 and 4.10 respectively. In Figs. 4.9(a) and 4.10(a), the normalized input Gaussian beams had significant diffraction within the photopolymer sample before the simulation started. As the modulation in the refractive index of the simulated waveguide core increases to the value $n_{core} = 1.502$, from an initial value $n_{core} = 1.5$, the beam is self-focused which just compensates the spreading of the beam, as seen in Figs. 4.9(b) and 4.10(b). After a few time steps in the simulation, the refractive index modulation of the core of SWW was reached at a value $n_{core} = 1.505$ that resulted in complete self-trapping of the propagating beam along the propagation beam axis. The SWW was fully evolved and created at this point, see Figs. 4.9(c) and 4.10(c).

The theoretical predictions from both models nearly match with each other. The diffusion based material model generated slightly smoother and uniform SWWs. The bending of bent SWWs is more prominent in diffusion material model. The refractive index modulation is faster in model 1 compared to model 2.

4.5 Simulation of the beam splitting effect

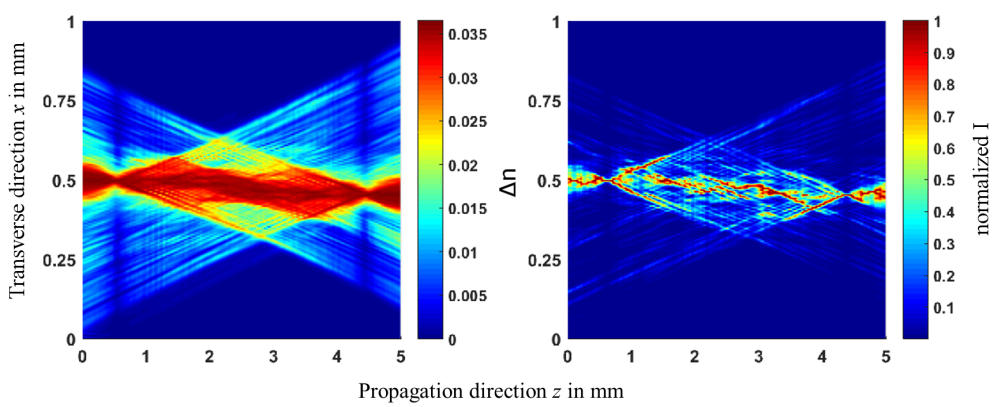

Figure 4.11: *Filamentous nature of a bent SWW when the nearby region started to polymerize. The result is obtained from the diffusion model [86].*

The material mixture saturation was reached towards the end of simulation

where it was observed that the SWW broke into filaments and generated a corresponding leakage of the beam intensity within the computational domain. Such a phenomenon was captured during the simulation of a bent SWW using the diffusion based material model, as shown in Fig. 4.11. There, the bent SWW was created from two counter propagating beams having beam widths of 50 µm, respectively with an offset or misalignment of 50 µm between them. The propagation distance along the z axis was fixed to 5 mm. In the diffusion model, the simulation started with a photo-polymer mixture having 97% monomer and 3% photoinitiator. For this case, the maximum modulation in refractive index is calculated by $n_p - n_m$, i.e., it equals to 0.04. When the simulation continued to run further after the desired refractive index modulation was achieved, the nearby region started to polymerize and the refractive index increased in those area too. This resulted in the breaking of the bent SWW into filaments and the intensity distribution was corrupted, as shown in Fig. 4.11. The filaments were generated because of the absence of proper cladding and finally resulted in no light guiding.

4.6 Simulation of multi-beam propagation

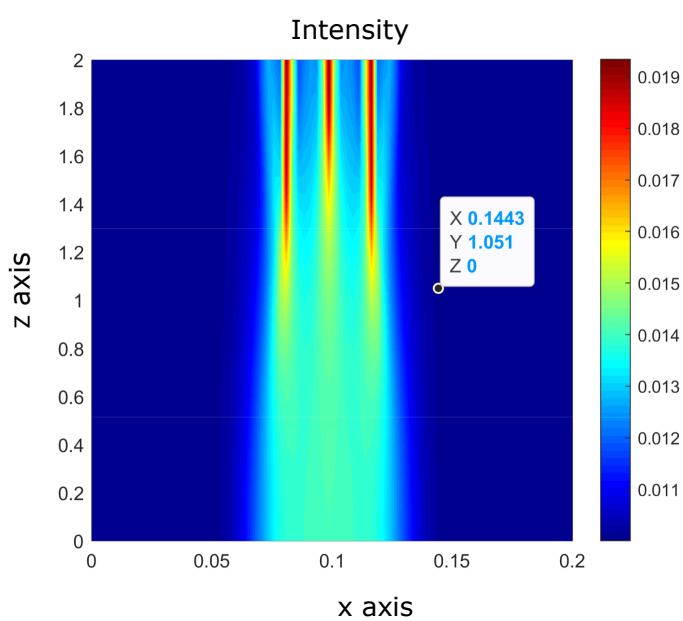

Figure 4.12: *3 Gaussian beams are propagated in the photo-polymer material.*

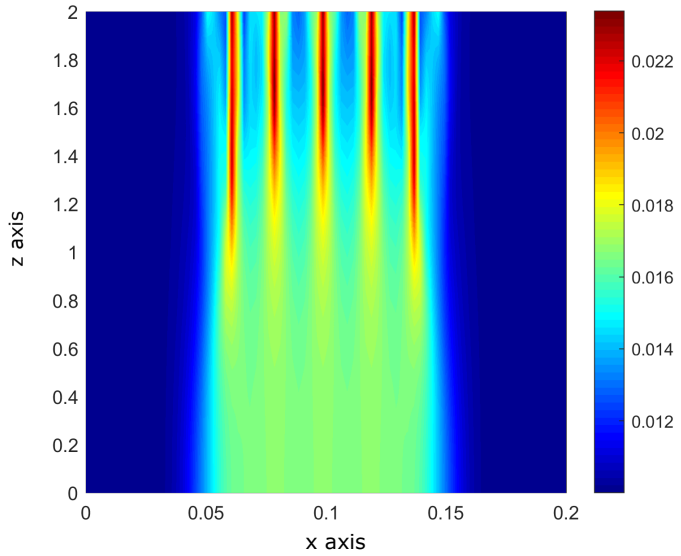

Figure 4.13: *5 beams are propagated in the photo-polymer material.*

By using both models, multiple beams were propagated in the photo-polymer medium. Some exemplary simulation results are provided in Figs. 4.12 and 4.13. In Fig. 4.12 three input Gaussian beams are propagated in the material mixture that resulted in the curing of 3 straight SWWs. Also, five Gaussian input beams were propagated in the photopolymer medium, as shown in Fig. 4.13 that lead to the curing of 5 separate SWWs. One could tweak the separating distance and direction between the propagating beams to generate more complex photonic components as well. So, this technique is useful to model other polymer photonic components. However the evolution of SWWs for complex photonic components will strongly depend upon the width of the propagating Gaussian beams, the number of beams, the direction of beam propagation to the sample and the gap or offset between each other. Also, the CN-BPM scheme was further adopted to enable the multi-input multi-beam propagation to the photo-polymer sample.

In summary, in an initial systematic investigation, a comparative study on the theoretical predictions from two kinds of material models for simulating straight SWWs and bent SWWs was discussed. The suitability of both models to simulate the polymerization and light guiding in self-written waveguides is evaluated. The results from the simple phenomenological model 1 nearly match with the results obtained from the more complex diffusion based material model 2, with a few exceptions noticed in the uniformity and the bending of the SWWs [86]. The SWWs created using the diffusion based material model

show smoother, more uniform surfaces and more prominent bending compared to the SWWs created using the phenomenological model. The curing time of bent SWWs is provided for both models showing that model 1 yields a faster increase in refractive index in comparison to model 2. Also, the self-written structures become filamentous when the nearby region starts to polymerize as the evolution in refractive index is near to the maximum or saturation value of the refractive index. Furthermore, it is possible to create more complex SWWs by using multi-beam propagation scheme.

Chapter 5

Numerical Investigations on a bent SWW

In this chapter, various numerical investigations carried out on bent SWWs are described. A bent-SWW is established in the photo-polymer mixture when two opposing Gaussian laser beams with offset or gap along their propagation axes are traversed through the medium and the beams, eventually, get self-trapped. Here, the investigations are ranged from the study of the temporal dynamics of refractive index modulations, their corresponding effect on the intensity carrying capabilities and the compensation of the gap or misalignment with respect to the length of the bent coupler. Furthermore, a study on the curvature and the curing time of a bent coupler which are regulated by controlling some of the model parameters during the simulation process is reported. The model parameters are referred to the component concentrations, value of the rate constant and propagation distance between the opposing beams.

The schematic diagram of a bent coupler SWW is provided in the Fig. 5.1. Here, the misalignment is quoted as the offset d which is also the gap between the propagation axes of the laser sources, as shown in Fig. 5.1(a). Subsequently, a photo-polymer mixture is considered which is composed of a monomer and a photoinitiator. In the laser-exposed region, the monomer starts to polymerize, as a result the counter propagating beams are strongly guided along the propagation axes. The gap or misalignment between them is compensated as the self-writing process proceeds further and finally, a bent SWW is created within the photo-polymer sample, as shown in the Fig. 5.1(b). This type of bent SWW have received potential applications as a coupler between two laser sources, two waveguides or a waveguide and a laser diode. It can also be applied to active or passive components. The very classical mechanism to couple light into waveguides includes the simple butt-coupling

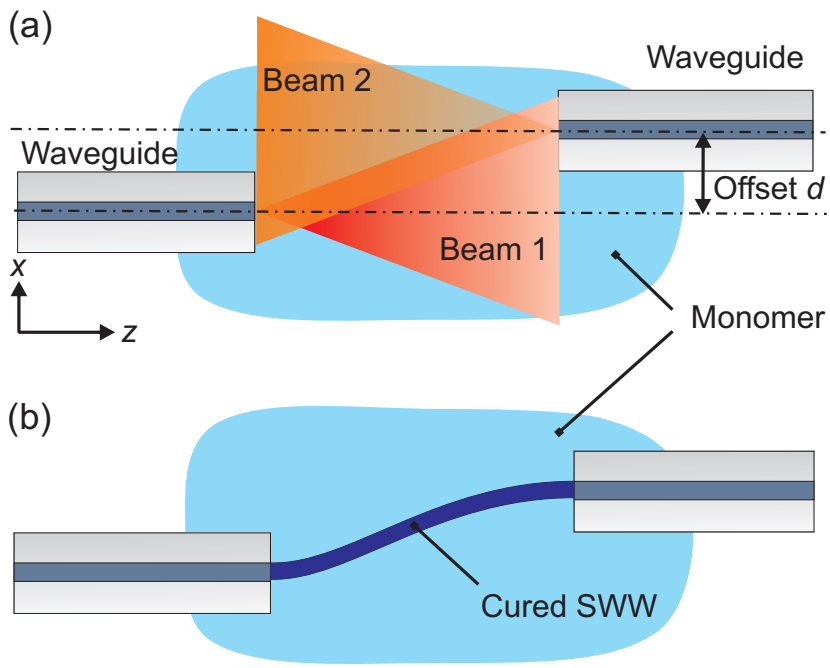

Figure 5.1: *Schematic diagram of the writing process of a bent SWW.*

technique where opposing optical components or waveguides are placed in such a way that the maximum intensity gets transferred between them. Often mirror couplers are used for coupling light sources into multimode waveguides that redirects the vertically incident light into the waveguide core.

Another approach which is often pursued for single mode waveguides relies on grating couplers which converts a vertically incident mode from a light source into a propagating mode inside the waveguide by means of diffraction [26]. However, very precise positioning of the optical components is required to achieve a coupling efficiency as high as possible. To overcome this drawback, Lindemann et al. demonstrated a method where they connected single-mode waveguides using a two-photon polymerization process [87]. A very precise path planning was essential in their case. This can be circumvented by self-written waveguides where an optimal waveguide is formed through a self-guiding effect without pre-planning and excessive laboratory equipment. The interaction between two counter-propagating beams with no gap between their propagation axes that resulted in the creation of self-written channels in photosensitive material as demonstrated by Sukhorukov et al. [22]. Malallah et al. [64] tested the same for dry photo-polymer material. The evidence of compensation of

the misalignment between two counter-propagating beams and its impact on coupling efficiency is experimentally exhibited by Günther et al. [65]. The optical coupling for a two-photon SOLNET(self-organized lightwave network) that is created from two opposing beams was reported by Yoshimura et al. [20]. They determined the increase in the misalignment tolerance by applying a two-photon photo-chemistry model to the photo-polymer mixture. The phenomenon of interaction between several SWWs considering a diffusion-based material model within a photo-polymer mixture was investigated by Belgacem et al. [81]. In various earlier studies on bent SWWs, the gap between the counter-propagating beam was kept small to generate an overlapping beam region. When the light cones emerging from laser beams from both fibers overlapped, the misalignment was compensated, as shown in [65]. The interaction angle between the opposing beams was kept small so that the beams can merge [22]. The offset value in one of our numerical investigations was increased beyond half of the beam diameter for identical counter-propagating beams and it was demonstrated that the gap can be compensated only when the length of the coupling structure was increased further. The aim of the chapter is to use the already described customized research tool to perform systematically numerical investigations on a bent coupler for determination of the refractive index modulation, the gap compensation, the advent of the curvature and the determination of the curing time. As described in the previous chapter, the customized research tool was implemented using MATLAB R2016b in which the CN-BPM method is directly coupled to the evolution of 2 dimensional diffusion equations to describe the polymerization process and carry out numerical investigations. The implemented diffusion model was earlier proposed by Zaho et al. [79]. The proposed diffusion model was further adapted by Belgacem et al. and included a saturation term in the refractive index modulation [81].

5.1 Numerical model and parameters

Eqs. (4.2) and (4.3) from the previous chapter were used to compute the evolution of monomer and polymer concentrations for the photo-polymer material sample. The diffusion of the monomer and polymerization mechanism were considered during the simulations. The refractive index modulation of the material mixture is then signified by the Lorentz-Lorentz relation. For simulating the optical beam propagation, the CN-BPM scheme along with the TBC was used to obtain the light distributions within the photo-polymer material mixture. The set of 3 partial differential equations is updated in the leap-frog manner during simulation. The simulation proceeds in the time

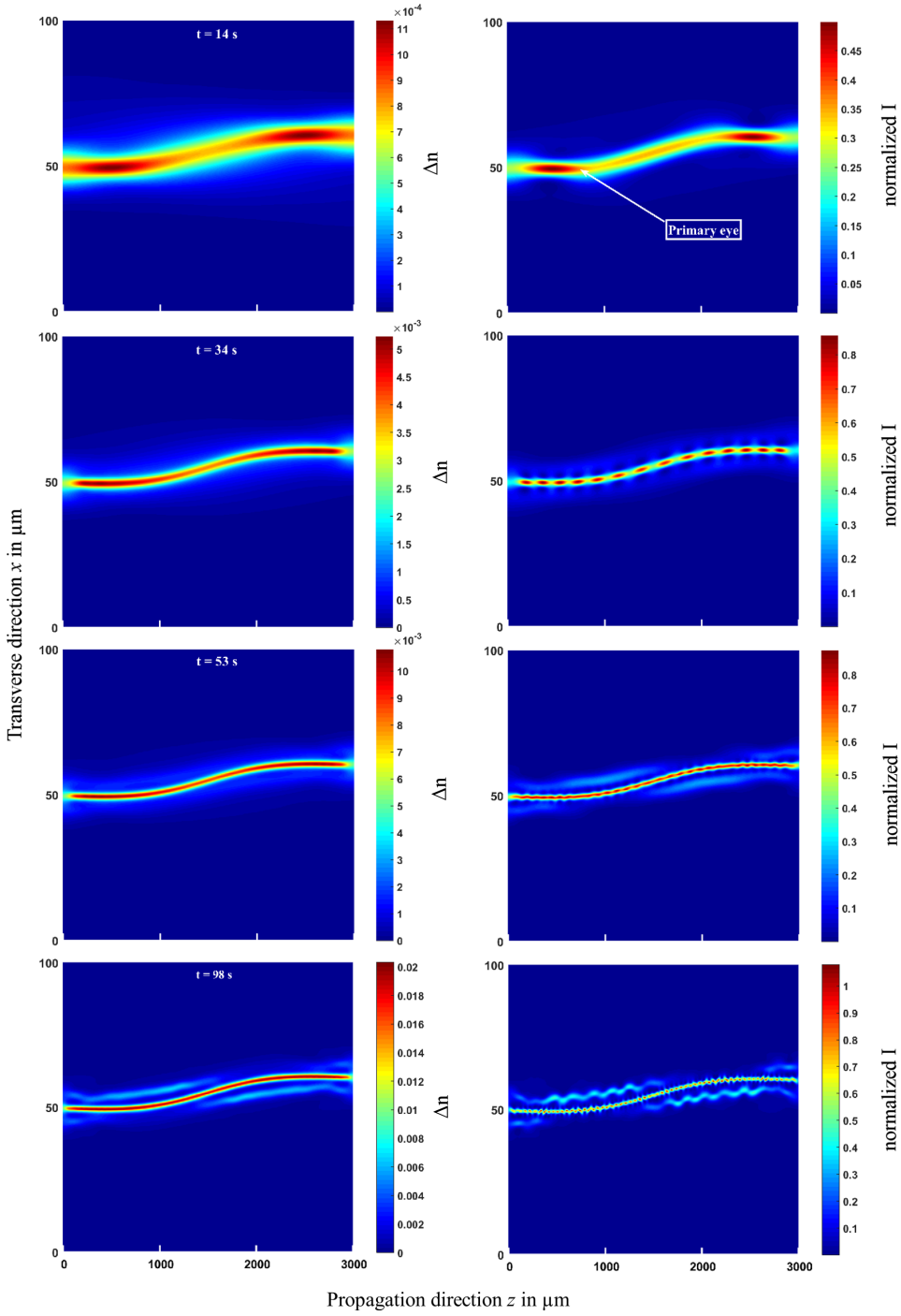

Figure 5.2: *Temporal dynamics of the refractive index change $\triangle n$ of 0.001, 0.005, 0.01 and 0.02 (from top to bottom) (a) and corresponding normalized intensity profiles (normalized I) at times $t = 14$ s, 34 s, 53 s and 98 s, respectively (b). [45].*

domain. For every time step, the concentration of monomer and polymer are obtained by solving Eqs. (4.2) and (4.3). Then these values enter into Eq. (4.4) to obtain the current estimate of the refractive index. Subsequently, this refractive index profile is used in Eq. (4.4) to obtain a new, 'current' estimate of the light beam intensity distribution in the x-z plane.

All numerical investigations presented in this chapter were performed in 2D because of simulation speed limitations and also for lowering of computing capacity. In one earlier study, Belacem et al. validated the outcomes from the diffusion material model coupled with 3D BPM with a 2D model for a smaller volume and did observe the same behavior as in 2D [81]. Therefore, we assume the same behaviour as in 3D case as well.

For carrying out numerical investigations on bent couplers, two Gaussian beams, each having a beam diameter of 20 µm that is defined as twice the beam radius, i.e., $2 * x_0 = 20\,\mu m$ with an offset of 10 µm between them are propagated into the photo-polymer mixture from opposite directions. The diffusion constant $D = 6 \times 10^{-15}\ m^2/s$ is considered in the simulation that was measured experimentally in [85]. The excitation beam wavelength was set to 550 nm. In all numerical investigations, the value of the rate constant $k_r = 0.001$ is considered expect one scenario where the impact of various rate constant values on the curing time of the bent SWW was investigated. For this case, four different values for the rate constant were taken, $K_r = 0.001, 0.005, 0.01, 0.02$, respectively. The refractive index of polymer n_p, monomer n_m and photo-initiator n_a are fixed at 1.52, 1.48 and 1.46, respectively [81]. The step increments along x and z directions are fixed to 0.5 µm and 1 µm respectively. The temporal step size during simulation is 1 s. Most simulations were carried out for total 500 s. The step sizes were fixed in a way that they satisfied the convergence criteria for finite difference approach applied to PDEs in Eqs. (4.2) and (4.3). The propagation constant for the standard CN-BPM scheme is fixed to $\alpha = 0.5$ because it is then unconditionally stable irrespective of the step sizes.

5.2 Temporal dynamics of refractive index and beam intensity

In the beginning, the photo-polymer mixer was considered to consist of 97% monomer and 3% polymer. By knowing the concentrations of monomer and polymer in the sample, the initial refractive index of the sample n_1 was calculated by using the Lorentz-Lorentz relation Eq. (4.4). Another value of refractive index n_2 for the material sample was also calculated at the end of

the simulation where all monomer was converted into polymer chains. So, the maximum modulation in refractive index was obtained by subtracting n_1 from n_2 . The simulation began from an uniform refractive index background having the value n_1 and the maximum possible modulation in refractive index in the current numerical investigation was 0.038. As the simulation proceeds in a temporal loop, the refractive index difference between the bent SWW core and cladding continued to increase until the maximum saturation was achieved. The dynamics of refractive index modulation between the core and cladding part of the SWW and beam intensity profiles for the bent SWW during the simulation are shown in Fig. 5.2.

Initially the waist of the Gaussian beam was applied at the input face and the intensity had a trivial maximum near the origin at the input port. In Fig. 5.2, the refractive indices are provided on the left side and corresponding beam intensity profile shown on the right side. The intensity values are obtained in the x-z plane. At $t = 14\,\mathrm{s}$, the refractive index modulation between the core and cladding was at $\Delta n = 0.001$. At this point, a bent SWW was just created within the photo-polymer sample.

The maximum intensity focus points are specified as primary eyes in the intensity distribution profile of the coupler in Fig. 5.2. The primary eyes in the intensity distribution profiles are focused near the point of the source exits. Then the refractive index difference between core and cladding part of the coupler was increased to $\Delta n = 0.005$ at time $t = 34\,\mathrm{s}$. The primary eyes are observed to move within the bent SWW at this stage. Here, the refractive index modulation becomes large enough to counteract the diffraction and the primary eyes start to move away from the input port along the propagation axis [18]. The locations of the primary eyes change over time. The SWWs become more and more uniform to form a channel beyond the primary eyes. Indeed, the numerical simulations from Monro et al. [18] suggest that the eyes are always a precursor to the formation of a waveguide at the specific transverse position in the material. They indicate that the structure of the SWW is closely related to the trajectories of the eyes within the material sample. The movement of the primary eyes within the bent SWW when $\Delta n = 0.005$ at $t = 34\,\mathrm{s}$ indicated a good guiding capabilities of the structure created. However, when the refractive index difference grows to the value $\Delta n = 0.01$ at time $t = 53\,\mathrm{s}$, the width of the evolving bent SWW coupler becomes dramatically narrower. A further increase in Δn value to 0.02 at $t = 98\,\mathrm{s}$ leads to a large leakage of radiation from the coupler to the surrounding environment because of the narrow non-uniform core. At this point the nearby region started to polymerize. It was also observed during the simulation that the SWW broke and disappeared when the modulation in refractive index difference between core and cladding Δn

reached the value of 0.03. From this analysis, it is interpreted that a refractive index modulation $\Delta n = 0.005$ is quite an optimal value to obtain a bent coupler with good waveguiding capability for the considered material sample. There is also a work by Missinne et al. [88] where it was demonstrated that more than 98.4% of transmission is achieved for a partially polymerized SWW reaching a refractive index value higher by 0.004 - 0.005 than that of the surrounding unpolymerized material. Their results are quite consistent with the current investigation. The intensity distribution profile of the simulated bent SWW

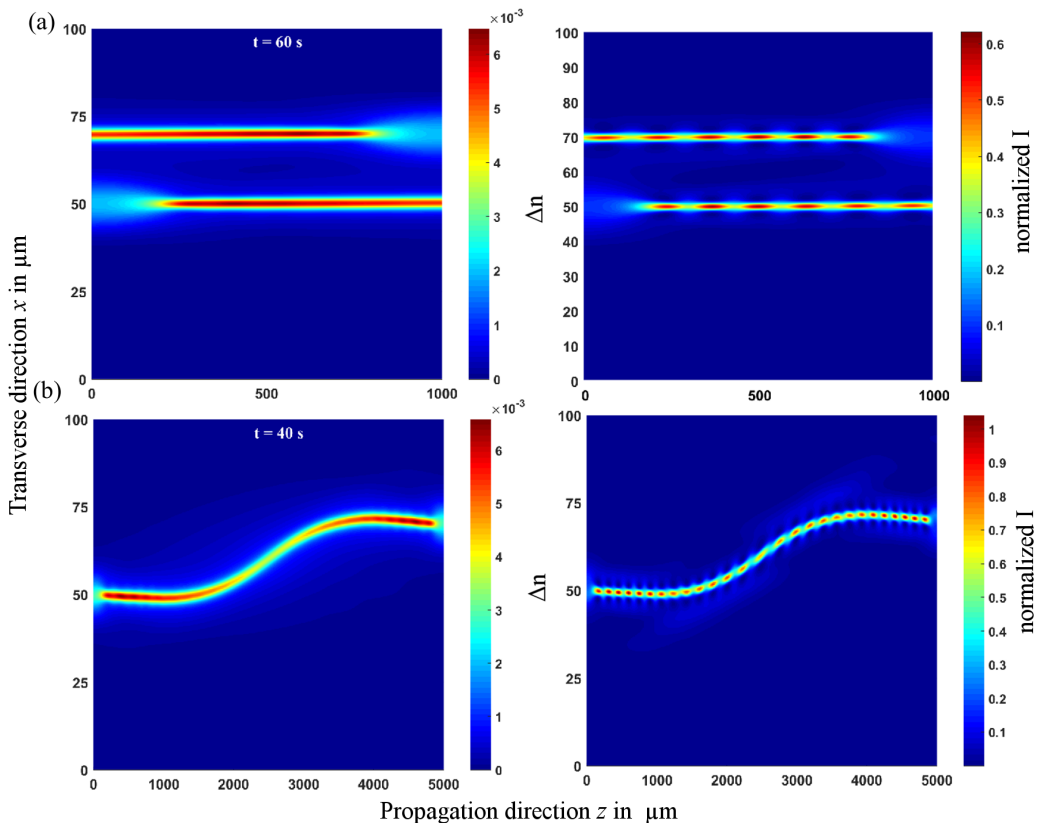

Figure 5.3: *Refractive index modulation on the left and normalized intensity profile (normalized I) on the right column. (a) Offset is 20 µm, coupling length is 1,000 µm (b) Offset is 20 µm, coupling length is 5,000 µm. [45]*

exhibits certain dynamics as well. As it gets evolved in a temporal loop, the effective refractive index and number of guided modes both change over time. To specify the properties of a bent SWW, one completely evolved waveguide is extracted when the refractive index difference Δn between core and cladding

is 0.005 at $t = 34\,\mathrm{s}$. This completely evolved SWW had an effective refractive index of 1.48 and the optical waveguide had two guided modes at the entry port. For the propagating beam at wavelength of 550 nm, the power loss was computed by via $P(l) = 10 * log(^{I_0}/_{I_l})$ and equals to 1.008 dB. Here I_l is the output intensity and I_0 is the input intensity. The power loss that accounts for both the insertion loss as well as the bending loss was also calculated. In one optimal bent SWW, when the $\Delta n = 0.005$, other beams having wavelength of 450 nm and 650 nm were propagated through it. We only observed different eye distributions in the intensity profile without altering the major properties of the cured SWW.

5.3 Investigation for offset tolerance

The misalignment between the two light trajectories is compensated when a bent SWW forms and the intersection angle between the counter-propagating beams is quite small, [22]. The misalignment in a direction transverse to the beam propagation also gets compensated when the light cones coming from counter-propagating laser beams or fibers overlap [65]. Yoshimura et al. demonstrated the self-aligned optical coupling involving nano-scale optical devices with wide tolerance in misalignment range by using the two-photon photo-chemistry approach [20]. The investigation was carried out for offset or gap tolerance for specific optical models. In this work, two identical opposing Gaussian beams with beam diameters of 20 µm, were counter-propagated through the material sample to create a bent SWW. The offset value was set at 20 µm, which is 2 times larger than half the beam diameter to carry out the numerical investigation for offset tolerance. The coupling also depends upon the longitudinal distance along the z axis. The results obtained in the current study are shown in Fig. 5.3. The refractive index profile of the bent SWW is shown on left side and the corresponding intensity profile on right side in Fig. 5.3. It was observed that the self-written channels from opposite ends just pass each other without any connection established between them when the longitudinal distance along $z-$axis between the counter propagating beams was set to 1,000 µm, see Fig. 5.3(a). Then the separation distance in z direction between the beams was increased by a factor of five, i.e. the beams were propagated for a distance of 5,000 µm. For this scenario, the two self-written channels from the opposite ends were merged to create a single channel as a bent SWW, see Fig. 5.3(b). For both these cases, the offset value was fixed at 20 µm. The simulation results shown in Fig. 5.3 are obtained when the refractive index difference between the core and cladding was $\Delta n = 0.005$.

The modulation of $\Delta n = 0.005$ was achieved in less time for the second case when the propagation distance was 5,000 µm (after 40 s) compared to the first case where the separation distance was 1,000 µm (after 60 s). There was no overlap between the beam intensity distributions in the first case due to smaller divergence angle, see Fig. 5.3(a). This leads to a slower modulation in refractive index value. Due to larger divergence, the opposing beams were merged when the $\Delta n = 0.005$ at t=40 s.

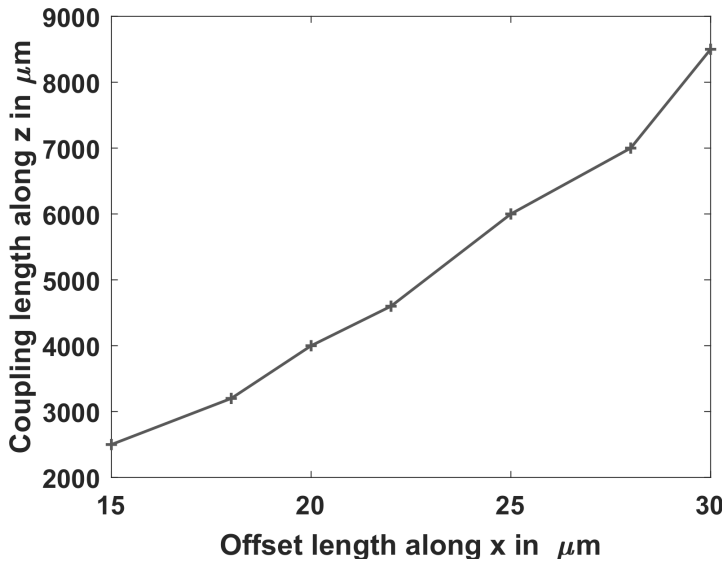

Figure 5.4: *Minimum separation distance between the sources along the z axis required to compensate the lateral offset along the transverse x axis. [45]*

To emphasize the relationship between the misalignment and coupling length of a bent SWW, further simulations were carried out for other offset values of 10 µm, 15 µm, 25 µm and 30 µm, respectively. The necessary minimum longitudinal separation distance along the z axis between the counter-propagating beams obtained is shown in Fig. 5.4. This was the least separation distance that was required to establish a connection between them. It was also observed that, when the offset is less than or equal to 10 µm which is half the dimension of beam diameter, the longitudinal separation between opposing beams has no impact on the offset tolerance. The connection was always established between the channels and a bent SWW is created within the mixture no matter how large or small the longitudinal separation between the sources is for the offset value of 10 µm.

As the lateral misalignment value was increased beyond 15 µm, the length of

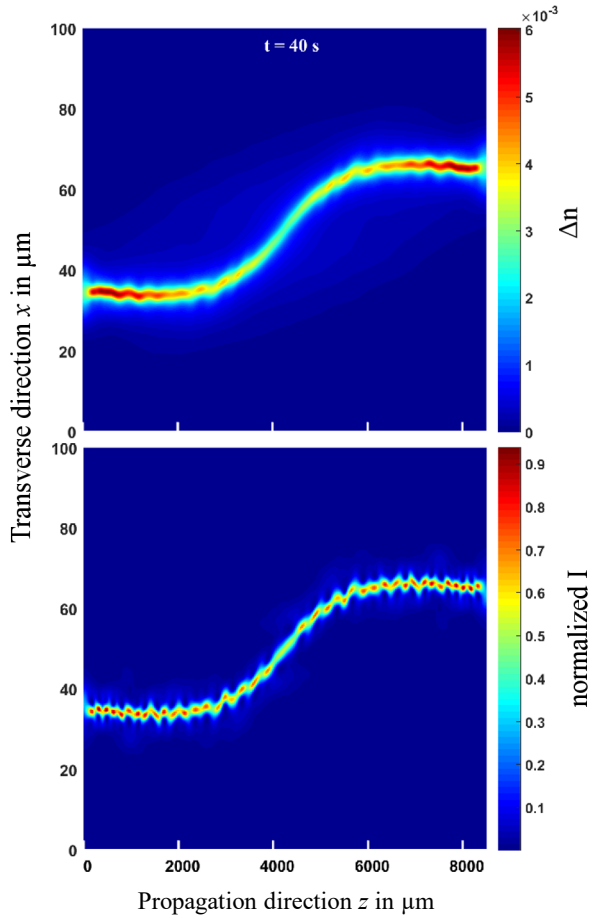

Figure 5.5: *Refractive index modulation $\triangle n$ (on top) and normalized beam intensity I (on bottom) when the misalignment between counter propagating beams is 30 µm. [45]*

the coupling structure must increase to compensate higher offset misalignments. The bent coupler was created at a minimum separation distance of 8,500 µm when the misalignment between the opposing beams was at 30 µm, as shown in Fig. 5.5. However, the bent SWW created for this scenario did not possess a smooth surface. There was a fluctuation in the diameter of the coupling structure along the transverse x axis. This emerged because of the large separation distance 8,500 µm between the counter-propagation beams for the offset value of 30 µm. It was observed due to loss in the directional properties of the beams because of the large separation distance between them. Also, one could study the effect of an angle along with the offset and its combined effect on the length of the bent SWW. However, the inclusion of an angle along

with the offset will add more complexity to the existing basic phenomenon for counter-propagating beams. So, it was not considered in the current study and has to be performed in the next steps following this work.

5.4 Curvature of bent couplers

To investigate the shape of a bent waveguide coupler, further simulations were carried out where two Gaussian light beams with beam diameter 50 µm each propagated into the photo-polymer material. The opposing beams had a offset value of 50 µm. The propagation distance along the z axis was varied from 1 mm over 5 mm to 10 mm during the simulation. The resulting bent SWWs couplers are shown in Fig. 5.6. The beam intensity profiles were extracted when the refractive index modulation between core and cladding was $\Delta n = 0.005$ which is considered optimal for SWWs because it is the adequate value to move the primary eyes within the structure without much narrowing of the width of the coupler. We observed that the bending in the self-written coupler starts to form as the propagation distance between the counter-propagating beams increases. Apart from this, when the coupling length is 1 mm, the self-written structure has a larger width compared to the cases when the length is 5 mm or 10 mm. The bending was more prominent when the propagation distance was at 10 mm Fig. 5.6(c).

Due to the divergence of the Gaussian beams, there was a change in width and curvature/bending of the bent SWW. The beams do not diverge linearly and also the divergence angle is extremely small close to the exit port of waveguide. Consequently, there is no overlap between the opposing beams. For this reason, an almost straight waveguide was created when the coupling length was 1 mm along the z axis, see Fig. 5.6(a). The divergence angle increased when the beams were propagated into the far field region that provided an overlapping area between the intensities of the opposite SWW channels and the modulation in phase as well as amplitude evolved between the channels. The curvature of the wavefront increases due to larger divergence angle when the separation distance between the sources increased to 5 mm and 10 mm. The obtained simulation results for the separation distances for the creation of bent SWW structures is shown in the Fig. 5.6(b) and (c), respectively. Furthermore, it is clearly evident from the simulation results that the width of self-written couplers was decreased as the longitudinal separation between counter propagating beams increased, as shown in the Fig. 5.6. It is also worth noting that the misalignment was compensated for all three cases in the simulation because the offset value was considered in the range of the width of

the input Gaussian beam diameter.

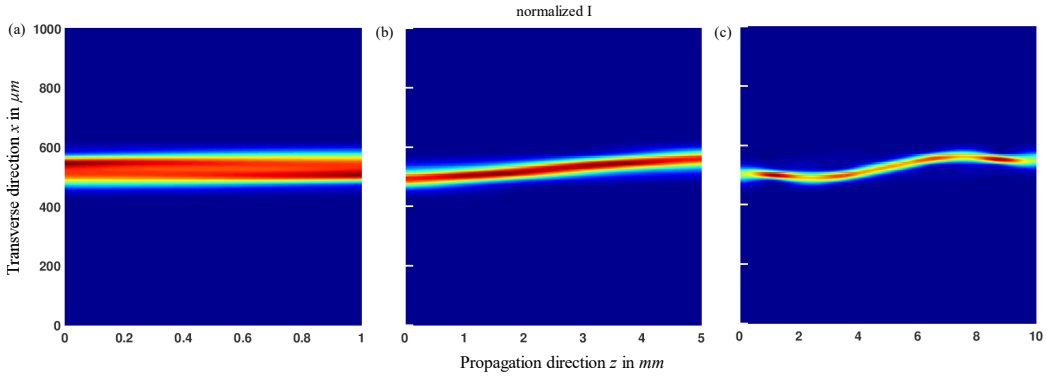

Figure 5.6: *Normalized intensity profiles for bent SWWs having a coupling length of 1 mm, 5 mm and 10 mm, respectively (left to right). [45]*

5.5 Impact of component concentrations on the curing time

To investigate the impact of component concentrations on the curing time of a bent SWW, various numerical simulations were carried out for 3 cases of the material mixture with varying amount of component concentrations. The component concentrations for the first case was fixed to 95% monomer, 2% polymer and 3% photoinitiator. For the second case, the concentrations of monomer, polymer and photoinitiator were set to 55% monomer, 42% polymer and 3% photoinitiator, respectively. Then for the third case, the component concentrations were considered as 25% monomer, 72%polymer and 3% photoinitiator. For all three cases the concentration of the photoinitiator was fixed to 3% to ensure the same rate constant during the simulation using the diffusion model. The maximum possible modulation in refractive index Δn for these three cases was slightly more than 0.03 (case 1), 0.02 (case 2) and 0.01 (case 3), respectively. The values for Δn were obtained by inserting the component concentration values in the Lorentz-Lorentz relation.

The temporal dynamics of Δn for the bent coupler from these 3 cases of different component concentrations during the writing mechanism are shown in the Fig. 5.7. Different possible refractive index modulation values for Δn were achievable for the 3 material mixtures. The maximum refractive index modulation was 0.01 for case 3. The temporal evolution of the refractive index

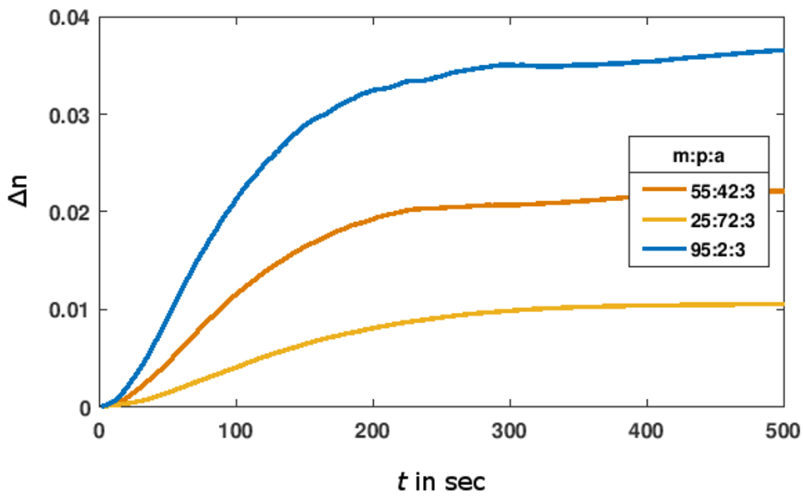

Figure 5.7: *Temporal dynamics of change in refractive index Δn values for component concentration ratios (m:p:a) within the photopolymer mixture of* $95:2:3$, $55:42:3$ *and* $25:72:3$, *respectively. Here, m, p, and a stand for monomer, polymer, and photoinitiator, respectively. [45]*

change is smoother for case 3 as opposed to case 1 and case 2, see Fig. 5.7. We also observed that the primary eye moved within the bent SWW at time $t = 34\,\mathrm{s}$ for case 1, $t = 53\,\mathrm{s}$ for case 2 and $t = 117\,\mathrm{s}$ for case 3, respectively. From the numerical investigation outcomes, one can conclude that the percentage of polymer concentration in the material mixture had a negative impact on the temporal modulation in refractive index values, i.e., the Δn evolution slowed down as the polymer concentration increased within the mixture, as in case 3.

5.6 Impact of rate constant on curing time

The impact of different values of the polymerization rate constant k_r on the curing time and refractive index evolution Δn of the mixture was investigated. the simulations were performed for four different k_r values, such as k_r equal to 0.001, 0.005, 0.01 and 0.02, respectively. The temporal dynamics of the change in the refractive index values for these k_r values is shown in Fig. 5.8. The primary eyes start to move within the bent SWW at the curing time $t = 17\,\mathrm{s}$ for the $k_r = 0.02$ during the polymerization process. However, the primary eyes moved within the bent SWW structure at about $t = 100\,\mathrm{s}$ when the rate constant was set to $k_r = 100\,\mathrm{s}$. For rate constants values 0.005 and 0.01, the

primary eyes move within the waveguide at t =22 s and 13 s, respectively.

From earlier explanations, it is well understood that the movement of primary eyes is a critical parameter to emphasize on the guiding capabilities of these SWW bent couplers. The results obtained from this numerical investigation suggest that the curing time or the writing time of the self-written structures can be extensively controlled by changing the parameter rate constant k_r during numerical simulations. The curing time decreased as the value of the rate constant increased. From experimental perspectives, the parameter rate constant can be changed by using more and less photoinitiator while preparing the the material mixture.

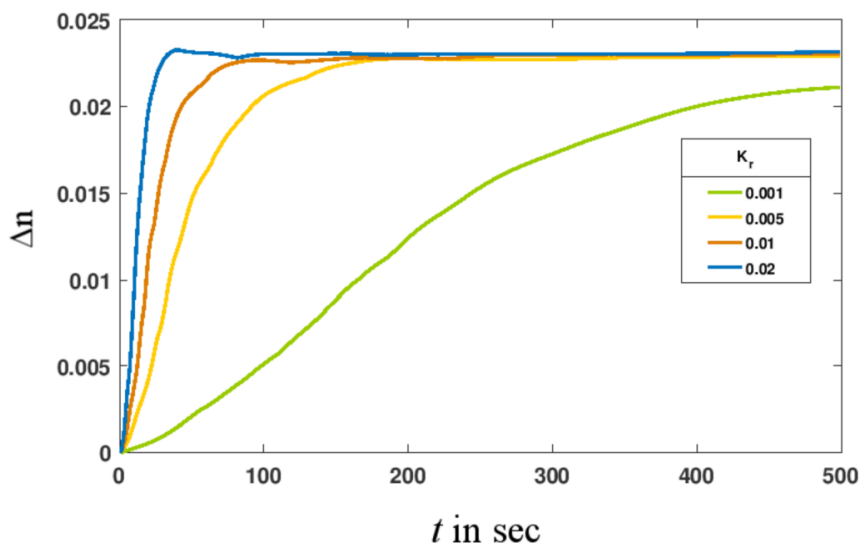

Figure 5.8: *Temporal dynamics of the change in refractive index* Δn *for rate constant* k_r *values* 0.005, 0.001, 0.01 *and* 0.02, *respectively. [45]*

Chapter 6

Experimental and theoretical analysis

This chapter introduces to various experimental as well as theoretical studies on polymer SWWs. The experimental results obtained by using just a single polymer material to create SWWs, also called one polymer-approach, are validated with the theoretical predictions from the diffusion material model. The transmittance from self-written waveguide couplers and their temporal dynamics of intensity profiles during the writing mechanism is reported for both experiments and simulations. The insertion losses were calculated for polymer SWWs to compare the corresponding attenuation coefficients between experiments and theoretically predictions. The optical interconnects are realized between multi-mode optical fibers based on the self-writing mechanism. The attenuation measurements were performed between optical fibers with SWWs as interconnects and compared to the case without SWWs, i.e. with an air gap in between.

6.1 One polymer-approach

The one polymer-approach to create self-written waveguides was explained by Günther et. al [65]. In usual approaches, the core and cladding of the waveguide are created from different polymer material samples. The one polymer-approach is simpler because only one polymer material is used to fabricate both the core and cladding part of the SWW. It does not involve the removal of the residual core material after the self-writing process was completed [89] and is thus more resource and cost-efficient. Furthermore, in this work, only one single writing beam was used to realize the core and cladding of a SWW whereas

in the two-polymer approach two writing wavelengths are required to pass through the photo-polymer sample to induce different amounts of refractive index modulations in the core and cladding part of the SWW, respectively. This is due to the fact that polymers exhibit different absorption cross sections in different wavelength regions [90].

The one polymer approach was first introduced by Missine et al. and was applied to commercially available Norland optical adhesive NOA68 [91]. It was then further modified by Günther et. al [76] by applying the one polymer approach to other, partially novel polymers, i.e. epoxy based acrylate, Syntholux 291 EA (SynIII). To conduct experiments, we have used the one photo-polymer approach and employed a material that was made from a mixture of two components. One compound was SynIII (93 wt.%), from Synthopol (Buxtehude, Germany) which is UV-curable with 80 wt.% TPGDA (tripropylene glycol dimethaacrylat), the second compound was 2,3-butanedione (7 wt.%) from Sigma-Aldrich (Taukirchen, Germany) also known as biacetyl. Biacetyl acts as the photoinitiator for the material mixture. These two components are mixed by hand for 3 hours to ensure homogeneity under standard room conditions. Then the mixture was placed in the vacuum chamber overnight to remove air bubbles present.

6.2 Experimental set-up

The experimental schematic for the fabrication of optical interconnects between two opposing multi-mode fibers is shown in Fig. 6.1. A four channel laser source (Thoslabs MCLS1, Germany) was used to provide the laser beam at 638 nm. The beam was then further passed through a 50/50 beam splitter (TW630R5F1, ThorLabs), that divided the incoming laser beam into two equal halves. These beams were then fed into two multi mode fibers having different core diameters. By the help of a high precision linear manual positioning stage, the multi-mode fibers were aligned with each other. The manual positioning stage provided five alignment axes along the lateral and axial directions. The formation of SWW happened only in the overlapped beam region between the counter propagating beams. So, the precise positioning of the waveguide was very crucial for the fabrication process. A slight misalignment between the opposing fibers could prevent the formation of the optical interconnect. An external white LED lamp (SCHOTT, VisiLED ring S80-55) was fixed on the top of the experimental setup. The external LED lamp was switched on and off in a controlled way that triggers as well as speed-up or slow down the polymerization process. A microscope objective and a CCD camera which

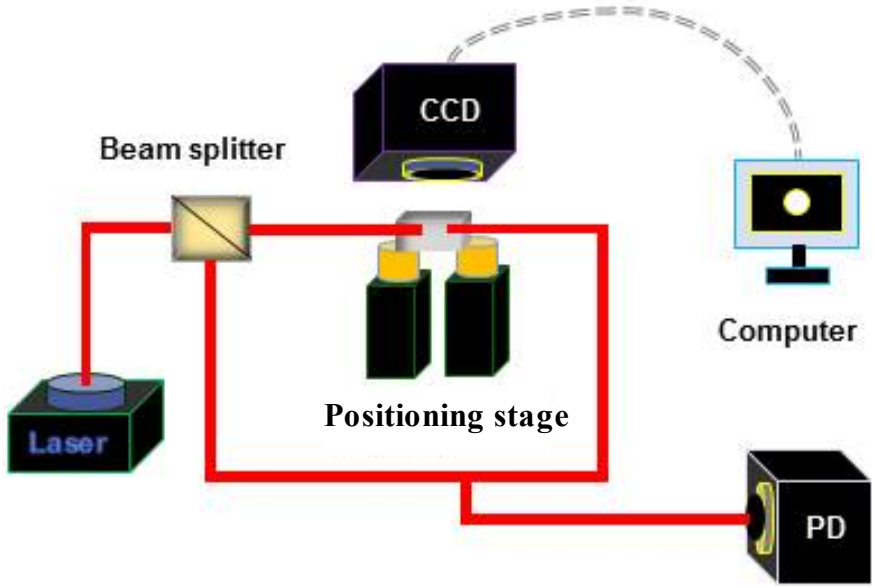

Figure 6.1: *Schematic of the experimental set-up for fabrication of SWWs. CCD : Charged Coupled Device, PD : Power Detector.*

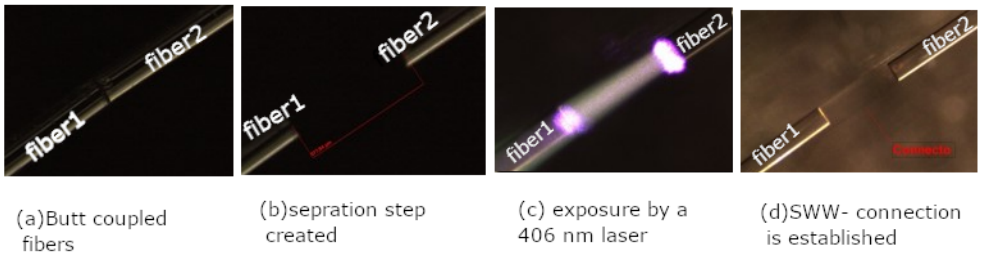

Figure 6.2: *Process steps involved to write the SWWs. Images were captured after the polymer and lasers are applied.*

was connected to a personal computer are carefully placed over the fibers to capture the images during the curing process. The multi-mode fiber ends were

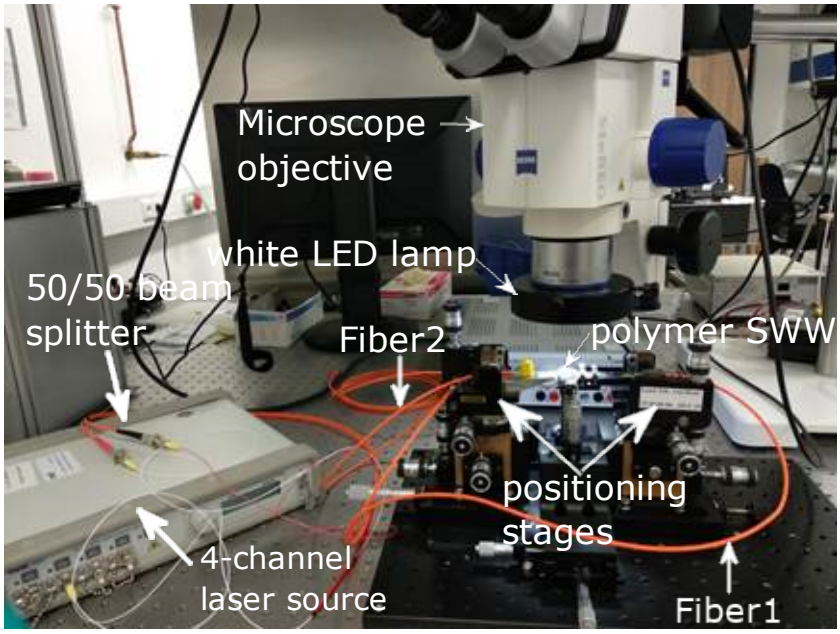

Figure 6.3: *Characterization experimental set-up.*

inserted into the photopolymer material mixture by using the 5 axes positioning stage. The right side collecting multi-mode fiber (CF) was detached from the beam-splitter once the physical connection was established between opposing fibers. The collecting fiber was then coupled to a power detector, PD (S120C, ThorLab, Germany) to monitor the transmitted intensity from the SWWs continuously.

It is also possible to completely eliminate the 50/50 beam splitter from the experimental set-up, i.e., a single incident laser beam is then launched to the multi-mode fiber on the left side, then propagates through the photopolymer material mixture, and finally the transmitted power is recorded from the collector MM fiber on the right side. This approach is known as one-way writing that demands very precise alignment of both the fiber ends.

A two-way writing approach was also performed for some experiments where two laser beams were used for writing the interconnect. The emerged interconnect SWWs from the two-way writing approach did not show any dependence of the propagation loss on writing direction because writing wavelength and writing power were kept in the same range for all experiments. The initial trajectory of the beam was observed between the multi-mode fibers after the

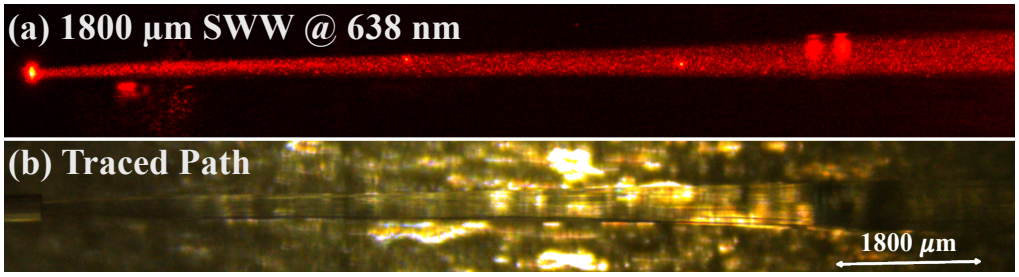

Figure 6.4: *(a) An SWW with a length 1800 µm is created by a laser beam at 638 nm with 15 mW power from a MM fiber having a 50 µm core diameter, (b) the traced path remained in the sample after the removal of excitation source. [46].*

laser beams were just launched. However, the interconnect SWWs are not completely evolved at this point. Any change in the position of the input beam leads to the bending of the beam trajectories within the material sample. Application of an external excitation source (white light LED) was required to cure the core and cladding part of the ultimately all solid interconnect. For almost all SWWs, the writing was carried out for 10 min in experiment. However, a stable output power was obtained after 4 min of the writing of the SWW. The fabrication process to write SWW in laboratory is shown in Fig. 6.2. At first, the opposing fibers were butt coupled and placed in front of each other by optimizing the transmission, as in Fig. 6.2 (a). Then, a separation distance was created by using a positioning stage, in Fig. 6.2 (b), and a laser beam at 406 nm was propagated from fiber1 to fiber 2, see Fig. 6.2 (c). The inscribed path remained within the sample when the laser light was turned off, see Fig. 6.2 (d). Two other exemplary SWWs are shown in Figs. 6.4 and 6.5 respectively. An characterization experimental set-up is shown in the Fig. 6.3. In Fig. 6.4, a SWW of 1800 µm length was written by using a laser beam at 638 nm having a power of 15 mW. The laser beam was launched from a multi-mode fiber having a core diameter of 50 µm and then propagated through the photo-polymer sample, in Fig. 6.4(a). The inscribed path of the light remained within the sample once the writing was completed, marked as the traced path in Fig. 6.4(b). In another example, a SWW was cured between two multi-mode fibers by using a laser beam at 406 nm having a power of 800µW. The length of the created SWW was 235 µm, as shown in Fig. 6.5(a). The diameter of the incoming fiber and the collecting fiber was 50 µm and 105 µm, respectively. Once the laser beam was turned off, the cured path remained within the photopolymer material sample. It was also possible to propagate a beam with a different wavelength, for example, 638 nm,

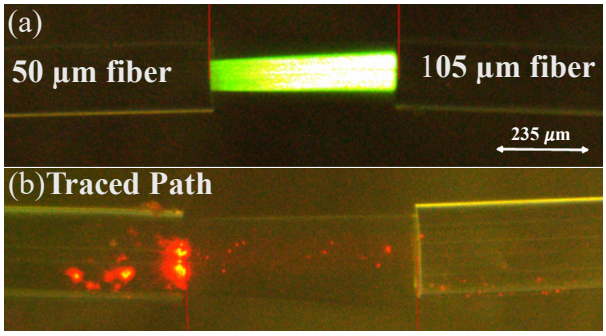

Figure 6.5: *(a) A 235 µm SWW created between MM fibers (different diameters) at a wavelength of 406 nm and a power of 800 µW. (b) A beam at 638 nm propagates in the existing SWW channel.[46]*

compared to the writing wavelength at 406 nm, through it after fabrication. One such example is demonstrated in the Fig. 6.5(b). The captured images are in different magnification scales of the microscopic camera.

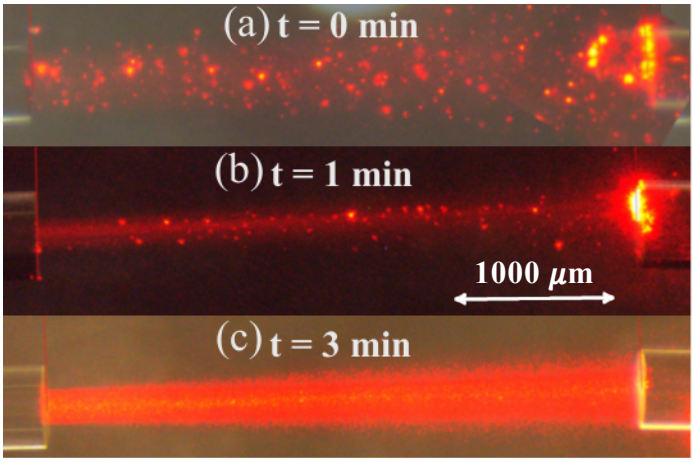

Figure 6.6: *Evolution of a straight waveguide in experiment. The panels show the evolution process of the waveguide as function of time [46]*

6.3 Theoretical simulations and numerical parameters

The numerical simulations of the underlying light induced-polymerization process was carried out by using the diffusion material model as it is more accurate than the phenomenological model. The diffusion model takes into account both the polymerization of monomer into polymer chains and the simultaneous diffusion of the monomer to the high intensity light field regions. A series of numerical investigations were carried out on SWW by using the diffusion material model as presented in [45]. The two-dimensional (2D) beam propagation method (BPM) scheme is coupled to a diffusion material model to obtain the induced change in the refractive index of the medium upon propagation of laser light along the propagation direction z. The temporal modulation of the refractive index is a complex phenomenon which accounts for the redistribution of the individual components during the simulation and requires the solution of the corresponding partial differential equations. The detailed explanations are provided in the chapter 2. The numerical parameter

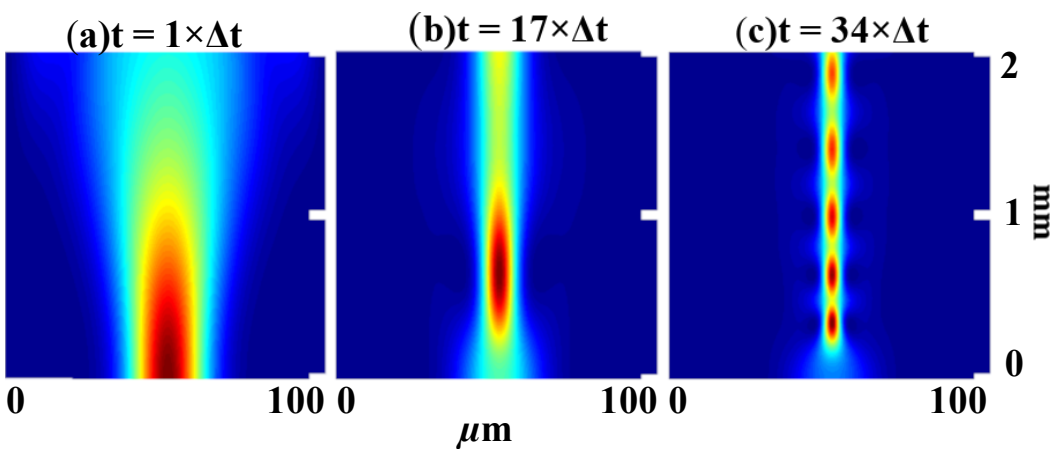

Figure 6.7: *Evolution of a straight waveguide in the simulation. Vertical length is from 0 to 2 mm, and the horizontal length is from 0 to 100 μm. [46]*

values were fixed as given below to carry out the corresponding numerical simulations. The diffusion constant $D = 6 \times 10^{-15}$ m^2/s is considered that was measured experimentally in [85]. As we already know, the value of the rate constant k_r can significantly influence the curing time for SWWs. So the value of k_r was fixed at 0.005 for all simulation and these were run for a total time of 10 min. The refractive index values of the polymer n_p, monomer

n_m and photoinitiator n_a are extracted from the product data sheets. Their values were set to $n_m = 1.52$, $n_p = 1.55$ and $n_a = 1.39$ respectively. The simulation started from an initial condition having 93% monomer and 7% photoinitiator. The percentage of mixture components are kept as the one prepared for experiment. A Gaussian beam was used as excitation source for the initial field distribution. During the simulations, the step increment size along the transverse and propagation directions were chosen as $\Delta x = 0.5\,\mu\text{m}$ and $\Delta z = 1\,\mu\text{m}$, respectively. The simulation proceeded in a temporal loop and step increment for time was fixed to $\Delta t = 1\,\text{sec}$. All values adhere to the convergence criteria of the finite difference scheme. The induced change in refractive index was computed by the material model which is then passed to the CN-BPM algorithm to compute the new light intensity distribution for each time iteration.

6.4 Evolution of straight SWWs in experiment and simulation

An SWW was fabricated in experiment and also simulated theoretically both having the same dimensions. The temporal dynamics of the evolution mechanism of the SWW during the writing process in experiment is shown in Fig. 6.6. A laser beam at 638 nm was utilized for the writing of the SWW. This straight SWW interconnect was written between two multi-mode fibers. The incoming multi-mode fiber had a core diameter of 50 µm whereas the output multi-mode fiber had a core diameter of 105 µm.

The images were captured by the CCD camera during the initiation of the laser excitation, after 1 min, and then after 3 min, respectively, as provided in Fig. 6.6. During the initiation phase the laser excitation was provided to the material sample. Light scattering can be observed as red dots before the commencement of material modulation as shown in Fig. 6.6(a). The spreading of the light beam became narrower just 1 min after the fabrication process started. From then on, the laser beam was confined to a fine thin line, as seen in Fig. 6.6(b), where the refractive index value of the medium along the beam propagation axis was increased from the initial value. However, the confinement of the beam was not sufficient at this stage to form a SWW. A sufficient material modulation was induced after 3 min, that resulted in the creation of a SWW with complete beam guidance, as seen in the Fig. 6.6(c). Also, the simulation was carried out for a straight SWW by propagating a Gaussian beam through the material sample and then observing the evolution of the temporal dynamics of intensity profiles obtained from different time

steps, see Fig. 6.7.

A very similar evolution pattern of the SWW was observed in the simulation compared to the experiment. Initially, at $t = 1 \times \Delta t$ the beam diverged, see Fig. 6.7(a). The spreading was then decreased at a later time at $t = 17 \times \Delta t$ due to the increase in refractive index value along the direction of beam propagation axis, see Fig. 6.7(b). The maximum focus point in the intensity distribution was created near to the entry port of the beam and at a later stage at $t = 34 \times \Delta t$ the maximum focus point started to move along the optical axis of the SWW, as shown in Fig. 6.7(c). This movement indicated good light guiding capability of the SWW depicting the attainment of sufficient refractive index modulation for beam confinement [18, 63]. So, the evolution mechanism of the SWW interconnect from experiment agrees well with the evolution of the intensity profile of the SWW from simulation.

6.5 Transmittance comparison during the writing process of an SWW

An SWW of 340 µm long was fabricated in experiment and also the similar dimension SWW was simulated using the diffusion model. A laser beam at 638 nm wavelength was coupled to a multi-mode fiber having a diameter of 50 µm to write the SWW. The transmitted intensity was recorded continuously from the exit port of the SWW for a duration of 10 min during the writing process in experiment. The same process is also repeated in the simulation. The variation of the transmitted power was recorded by the power detector (PD) that was coupled to the output port of the collecting multi-mode fiber in experiment. The transmitted power from experiment is shown in the Fig. 6.9. Initially, only the laser excitation was provided. At this point, the output intensity remained at 1 mW. Then the external LED was switched on in addition to the laser excitation. The white light from the LED lamp can be controlled in a range of 1 to 8, where the maximum setting 8 corresponds to an illumination of nearly 200 klx. The illumination the LED lamp was gradually increased till time $t = 100$ s and then afterwards kept at the maximum setting 8. The curing time of the SWW during the fabrication can be controlled by regulating the intensity illumination from the LED.

We observed that the transmitted power from the SWW steadily increased during the writing process till the maximum value of 5.1mW was obtained at time 100 s. The transmitted power remained at 5.1mW until $t = 200$ s and then there was a decrease in the intensity followed by another rise and finally the transmitted power stabilized. The dip in the transmitted intensity

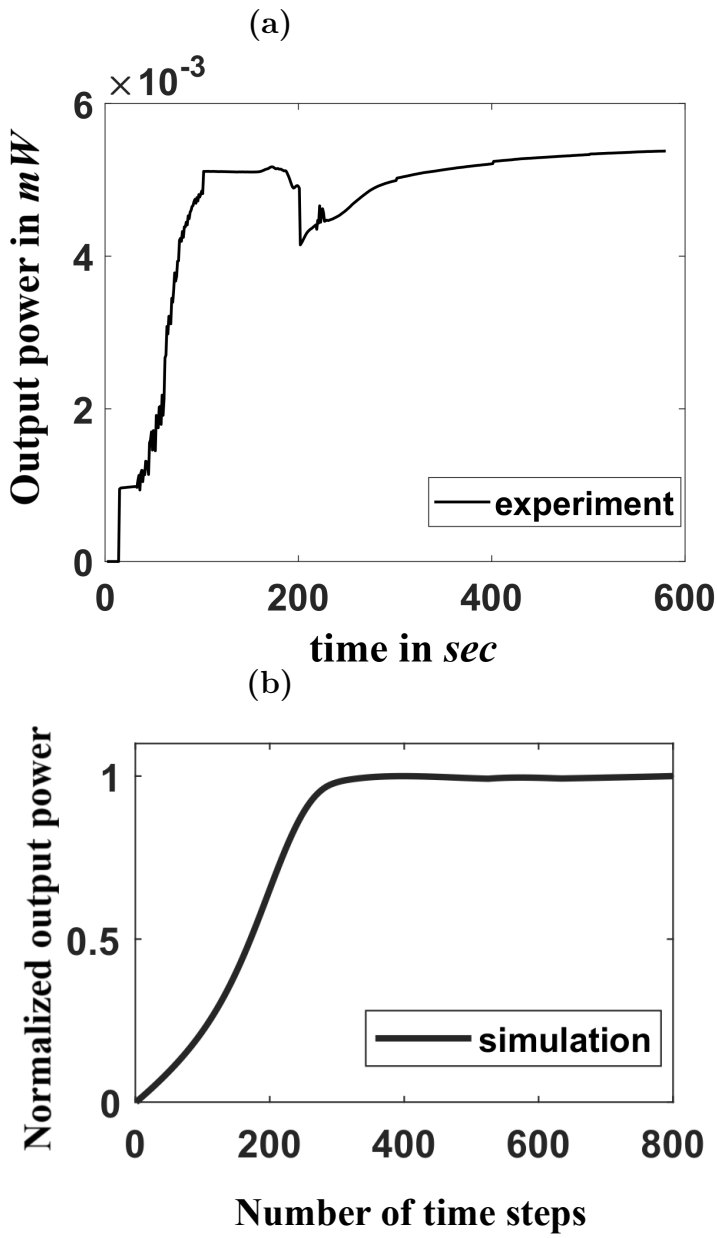

Figure 6.8: *Transmitted power during the writing process. (a) Transmitted power as recorded by the power detector for a 340 μm long SWW in experiment. (b) Normalized output power for a 340 μm long SWW in the simulation [46].*

could be due to different modulations of the refractive indices of the core and cladding part of the SWW during fabrication. Possibly at this point, the refractive index of the outer cladding part of the sample is increasing faster as compared to the inside core area as the former starts to solidify. The difference in refractive index between the core and cladding was reduced which then had a direct impact on the power carrying capability of the waveguide. The material sample completely changed to fully solid after the transition phase. The transmitted power saturates to a constant value which as also calculated from the simulation during the temporal evolution of a SWW. The transmittance increased smoothly and steadily from zero towards a maximum value and finally attains saturation when the liquid material sample completely polymerized in simulation. Its value during the evolution mechanism of the SWW in simulation having the same dimension as in experiment is shown in the Fig. 6.9(b). Of course, the obtained result from simulation reflects the ideal case. Additionally, it does not consider the illumination with the external white LED lamp. Only one excitation source, the Gaussian beam, was propagated through the material medium to create the SWW in simulation.

6.6 Attenuation in experiment and simulation

The attenuation measurements for various interconnect SWWs having axial dimensions ranging from 0 - 1,000 µm were performed at a wavelength of 638 nm. The laser beam was coupled to the input fiber with a core diameter of 50 µm and the transmitted power was received from the collecting fiber having a core diameter of 105 µm. Between these multi-mode fibers, several SWWs with lengths of 115 µm, 230 µm, 460 µm, 575 µm, 690 µm, 805 µm, and 920 µm were realized. At every length scale, the experimental measurements were repeated four times for each SWW to obtain better accuracy for the measured losses.

The fabrication process is explained in detail in [76]. The opposing fibers were butt-coupled without any residual gap between them in the very first step. A liquid drop of photo polymer resin mixture was placed over the two fiber tips in the butt-coupled stage and the maximum transmitted intensity I_0 from the collecting multi-mode fiber was measured. In the next step, the positions of the fibers were separated to create a gap length l in between them. The gap length l was equal to 115 µm, 230 µm, 460 µm, 575 µm, 690 µm, 805 µm, and 920 µm, respectively. The laser beam was launched from the incoming fiber towards the collecting fiber while the external LED was switched on during the curing of the SWW. Once the writing was completed, the transmitted power I_l was recorded. I_l was normalized to the transmitted power in the butt-coupled

case I_0 for the attenuation calculations. By doing so, the fiber based effects including the Fresnel reflections were subtracted from the actual measurement as we assumed a 0 dB loss at an interconnect length of 0 µm. The attenuation for the SWWs was calculated by using the Eq. (6.1).

$$L_{dB}(l) = 10 * \log(I_0/I_l). \tag{6.1}$$

The red dots shown in the Fig. 6.9 represent all calculated losses from the

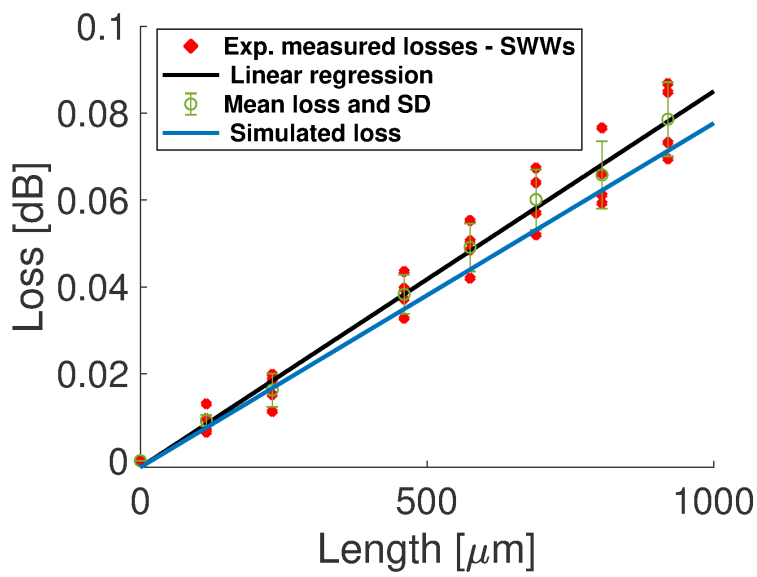

Figure 6.9: *Loss measurements at 638 nm for polymer SWWs from experiment and simulation. [46]*

experimental measurements. A linear fit was applied to these measurement data points. The gradient of the linear fit yields the attenuation coefficient. The attenuation coefficient based on the data from the experimental results is $\alpha_{experiment} = (8.43 \pm 0.3) \times 10^{-5}$ dB/ µm at 638 nm, as shown in Fig. 6.9. The standard deviation (SD) was computed for the measurement data points at a particular length l and the mean value was also determined, see the green circles in the Fig. 6.9. The error bars (in green color) are shown for the calculated dB loss values from the experimental repetitions at a particular length of the SWW. We observed that, as the length of the SWW increased, the size of the error bars also increased.

To validate the obtained experimental outcomes, SWWs at lengths from 0 - 1,000 µm in the interval of 50 µm were then simulated by using the diffusion material model. The simulations were carried out to calculate the dB losses

for SWWs where the mode field radius of the Gaussian laser beam excitation was set to 25 µm that is half of the core diameter of the input multi-mode fiber in the experiment at a writing wavelength of 638 nm. The refractive index modulation between the core and cladding of the SWW for the resin mixture consisting of Syntholux as the monomer and biacetyl as the photoinitiator was found to be $\Delta n = 4 \times 10^{-4}$ [65]. So, the evolving SWWs are extracted from the diffusion model in simulation when the refractive index modulation between the core and cladding was also $\Delta n = 4 \times 10^{-4}$. The losses were computed in the simulation for the SWWs and the procedure was repeated at each length scale. A linear fit was applied to the simulation results for the calculated dB loss values. The linear fit yields the attenuation coefficient for the simulation data set and equals to $\alpha_{simulation} = 7.93 \times 10^{-5}$ dB/ µm. The attenuation obtained from simulation of SWWs closely follows the experimental data, as shown in Fig. 6.9. The linear fit to the simulation results was within the range of uncertainty specified from the experiment. The dB losses were also measured for the cases when there was no SWW interconnect between the opposing multi-mode fibers. For this, the opposing multi-mode fibers were butt-coupled and the maximum transmitted power I_0 was recorded from the collecting fiber. Then air-gaps of length 115 µm, 230 µm, 460 µm, 575 µm, 690 µm, 805 µm, and 920 µm were created between them. However, no photopolymer resin mixture was applied over the fiber tips and the transmitted power I_l for different air-gap lengths was again recorded at the receiving end. Then, the dB losses were computed by using Eq. (6.1). The core diameters of the fibers were fixed same as in the earlier case. The calculated attenuation values are shown in Fig. 6.10. A linear field was applied to these attenuation values and the slope of it yielded the attenuation coefficient as $\alpha_{air} = 10^{-3}$dB/ µm. The attenuation coefficient for the air-gap case is 11 times higher than for the polymer-based SWWs. In the next step, the studies can be extended towards including further relevant parameters such as temperature and stress.

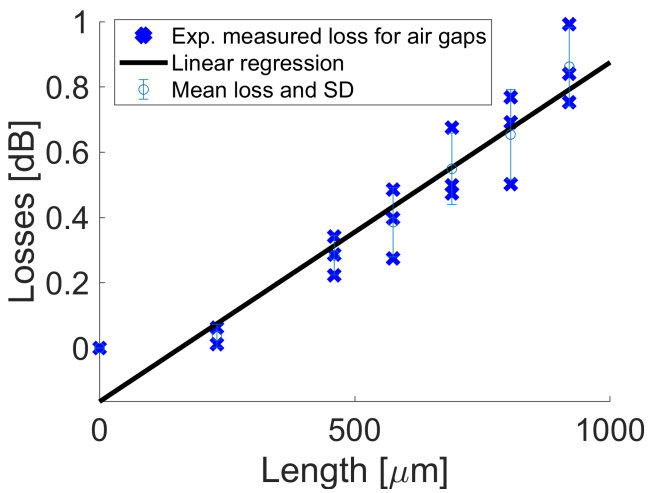

Figure 6.10: *Loss measurements at 638 nm for the case of an air gap between the fibers in experiment. [46]*

Chapter 7

Combined thermo-mechanical and optical simulations

In this chapter, a theoretical approach for combining thermo-mechanical simulations and optical simulations for planar optical polymer waveguide is presented. A finite element approach was considered to carry out thermal and stress/deformation simulations. The already implemented Crank-Nicholson finite difference beam propagation method (CN-BPM) was used to perform the optical simulations. The results obtained from the finite element analysis were coupled back with the CN-BPM results. It is thus possible to carry out the optical simulation of PMMA waveguides as a function of temperature gradients. A model was designed where a polysilicon microheater was implanted to the upper cladding of the PMMA waveguide to carry out the thermal simulations.

The temperature of the microheater was varied between 20°C to 200°C. Further, the impact of the induced temperature gradients on the refractive index modulation and corresponding change in the numerical aperture (NA) of the PMMA waveguide were determined. The temperature gradient also disturbed the optical properties by changing the beam intensity profiles and the movement of primary eyes within the optical waveguides. The thermally induced stress and deformation analysis for the PMMA waveguide were also carried out to determine the elongations along the transverse x and propagation z direction. Polymer waveguide structures lend themselves as very promising components for the broadband telecommunication connections, i.e. for computing systems, optical networks and sensor networks. One such prototype of an optical PCB using all polymer optical waveguide arrays and circuits had been examined for information handing performance by Lee et al. [92], that is shown in the Fig. 7.1. The photo-chemical mechanism and the nonlinear photo-absorptive effect on dry acrylamide polyvinyl alcohol based photopolymer was analyzed

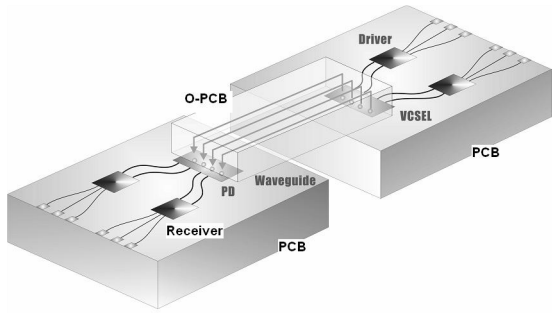

Figure 7.1: *A prototype design of an polymer optical PCB with optoelectronic VLSI circuitry [92].*

by Li et al. in [93]. Polymer materials are very attractive for integrated optical devices because they enable rapid processability, very good optical performance and high yield. They have relatively low losses and smaller birefringence compared to their counterparts silica. The polymer materials have negative thermo-optic coefficients ($\frac{\partial n}{\partial t}$) and they generally lie in the range $-1 \times 10^{-4\circ}C^{-1}$ to $-4 \times 10^{-4\circ}C^{-1}$ that is 10 to 40 times higher than most conventional optical glasses [9]. This enables polymer materials to be used for efficient thermal actuation. The thermo-optic coefficient plays a vital role in accessing the performance of polymer based photonic devices, as described in detail by Zhang et al. [94]. On the other hand, the operating conditions may easily drift and could lead to a change in refractive index that is induced by the change in the environmental conditions. This will cause thermal and functional instabilities in such devices.

The change of refractive index is influenced by two major factors and both of them counteract each other. The change in the density of the polymer and the increase in polarizability with respect to temperature are caused by a positive thermal expansion coefficient. The coefficient of thermal expansion is inversely proportional to bond strength. Due to weak inter-molecular bonds in polymer, they have very high thermal expansion coefficients. It is just material expansion over temperature and has nothing to do with refractive index or thermo-optic coefficient. The light intensity distributions within the waveguides can be significantly altered by a small thermally induced change of refractive index value, especially in coupled systems [95]. The operating service temperature of polymers is limited to the range between $60 - 250°$C that is substantially less than the operating temperature range for optical glasses ($400 - 700°$C) [96]. Mechanical deformations are eventually induced in the polymer waveguides because of the presence of the heat and stress.

Tensile stress is generated in a direction perpendicular to the beam propagation direction where as a compressive stress is generated parallel to the beam propagation axis. This is mainly caused due to the difference in the thermal expansion coefficient between the core and cladding part of the waveguide. The change in the environmental conditions represents a major drawback on the usability of the polymer material in this field.

In this work, we focused on combining thermo-mechanical and optical simulations by considering polymer waveguide structures as the basic elements for polymer photonic devices to analyse more comprehensively their corresponding properties and performance by taking into considerations all relevant physical effects. The variation of refractive index of optically transparent PMMA (poly methyl mathacrylate) waveguides within the temperature range from $20-200°C$ was investigated which is a reasonable range for this material [97, 98]. Also, optical simulations results, i.e. the intensity beam profiles within the PMMA waveguides, are performed which were induced due to different temperature settings of the microheater.

7.1 Thermo-mechanical simulations

The FEATool was used to carry out the finite element thermo-mechanical simulation and analysis of PMMA polymer waveguides. The finite element approach in the FEATool combines multi-physics and partial differential equation (PDE) simulation environments that allows the modeling of fluid dynamics, chemical engineering, structural mechanics, heat transfer and electromagnetic effects [99]. The modelling process in the FEATool is subsequently divided into sub-process such as the definition of the geometry, the generation of the mesh/grid, and the specification of the physical effects and boundary conditions, among others [100]. The mentioned sub-processes are often iterative in nature. To achieve an optimal performance for the design model, one may also repeat some of the procedure steps again.

In the current approach, the heat transfer module and the plain stress analysis module of the FEATool are used simultaneously under the multi-physics mode to carry out the finite element simulations of the waveguides which is then combined with the optical simulations. The PMMA waveguide model structures are designed in two dimensions in the FEATool, so that it can be easily coupled back to the two dimensional finite difference CN-beam propagation method that was used to conduct the optical simulations. As a result, the simulations do not require large memory space for operation. An efficient and very fast triangular grid system for the mesh generations was

selected which allowed more flexibility while specifying the grid size for different subdomains of boundary and geometry regions.

The heat transfer via conduction mechanism was taken into consideration for the thermal simulations. The effect of convection and radiation in polymer waveguides can be neglected, as demonstrated in [101]. The following Eq. (7.1) is used to carry out the thermal simulations.

$$\rho C_p T' + \nabla.(-k\nabla T) = Q \tag{7.1}$$

Here, C_p is the specific heat, ρ the density and k the thermal conductivity of the PMMA material. T is the temperature distribution within the waveguide and T' is the derivative of the temperature with respect to time. Table 1 shows the detailed values of the parameters that are set in the FEATool during the thermal simulations. Furthermore, the plain stress equations are used to calculate the elongation deformations in the PMMA waveguides, provided in Eqs. (7.2) and (7.3).

$$\rho u' - E/(1-\nu^2)((u_x + \nu v_y(1+\nu)\alpha T) + (1-\nu)/2(u_y + v_x)) = 0 \tag{7.2}$$

$$\rho v' - E/(1-\nu^2)((\nu u_x + v_y(1+\nu)\alpha T) + (1-\nu)/2(u_y + v_x)) = 0 \tag{7.3}$$

where ν is the Poisson's ratio is the ratio of lateral strain to longitudinal strain, E is the Young's modulus and α is the thermal expansion coefficient. v is the displacement along y-axis. ρ is the material density and u is the displacement along x-axis that is perpendicular to the optical axis of the waveguide.

The optical simulation of the models are carried out by using the CN-BPM along with transparent boundary conditions (TBC). The detailed of the implementation of the CN-BPM scheme is described in chapter 3. The CN-BPM scheme was considered because of reduced computational time and lower computational complexity. For thermo-optical simulations, the challenge is to combine commercial and own codes to perform a comprehensive multi-physics simulation of processes governing polymer waveguide performance. In general, the approach could also be combined with any more accurate finite difference time domain (FDTD) method for the optical simulations.

7.2 Model design

The schematic of the cross sectional view of the planar PMMA waveguides is shown in Fig. 7.2. A polysilicon microheater was implanted to the waveguides to mimic the case of thermo-optical switch. The microheater was placed at two different positions, i.e. on the top of the upper waveguide cladding and

inside the upper waveguide cladding, respectively. Both models were further considered for thermo-mechanical simulations along with the optical simulations. The upper and lower cladding of these waveguides were assumed to be made from monomer material in the liquid form whereas the core part of the models were assumed to be made from polymer PMMA material. Due to large negative thermo-optic coefficients, the polymer material in general can well be used for thermo-optical switches. The position of the microheater as well as its dimension have a significant impact on the efficiency of a thermo-optic (TO) waveguide switch, for example, and the switching time.

In the first case in Fig. 7.2(a), the polysilicon microheater was placed on the top of the upper cladding. Here, the width of the cladding and the core along transverse x and y-directions were 20 µm and 40 µm, respectively. The length of the waveguide along the propagation direction z axis was fixed to 1,600 µm in Fig. 7.2(a). The implanted polysilicon microheater had a width of 20 µm along the transverse x-axis and a length of 1,200 µm along the propagation z-axis. The microheater had the same dimension for the second model in the schematic in the Fig. 7.2(b). However, the microheater in this case was buried to the middle part of the upper cladding of the waveguide. The width of the core for the second model was again considered to be PMMA material having a width of 40 µm along the transverse $x-$ (and $y-$) axes and a length of 1,600 µm along propagation $z-$axis. The upper cladding and the lower cladding had a width of 80 µm along $x-$ (and $y-$) axes and were again considered to consist of liquid monomer during the simulations.

In Fig. 7.2(b), the microheater is fixed at a distance of 30 µm from the core part of the waveguide. The cladding width in model 2 in Fig. 7.2(b) is different from the width of the cladding in model 1 in Fig. 7.2(a). The second model was designed this way to fit the microheater within the upper cladding part of the waveguide and to keep a reasonable distance from the core. The width of the core part was same for both models, shown in Figs. 7.2(a) and 7.2(b). The central line (L1) passing through the middle section of the core part is the optical axis of the waveguide along the z direction. The temperature modulations and further induced elongations were obtained along the line L1 at various settings of the microheater.

The thermal simulations were carried out by the already described heat transfer module by using the pre-defined geometries. The initial temperature distribution T_0 was constant for the whole waveguide and was set to $T_0 = 20°\text{C}$. Then the temperature of the polysilicon microheater was varied from the initial temperature T_0 to the maximum temperature $T_{max} = 200°\text{C}$. The temperature of the microheater was increased until the output intensity from the exit port of the waveguide dropped below 50% of the initial input beam

intensity. Appropriate boundary conditions were chosen for thermal analysis. The boundaries denoted as 1,2,3 and 4 in Fig. 7.2(a) and 1,2,3,4,5 in Fig. 7.2(b) were set to a temperature $T_0 = 20°C$. Then, the boundaries denoted as 5,6,7,8 in the first scheme in Fig. 7.2(a) and as 8,9,10, 11 in second scheme in Fig. 7.2(b) were set to the temperature of the microheater $T = T_{microheater}$. The continuity boundary condition was set at the interface boundaries between the monomer cladding and the PMMA core. The continuity boundary condition ensures a smooth flow of heat between these media by establishing a link in between them. This is the default boundary condition from the FEATool and for the corresponding interior boundaries 6 and 7 in Fig. 7.2(b) and 9 and 10 in Fig. 7.2(a) the same conditions were accepted. The material model parameters fixed during the thermal analysis are provided in the Table 7.1.

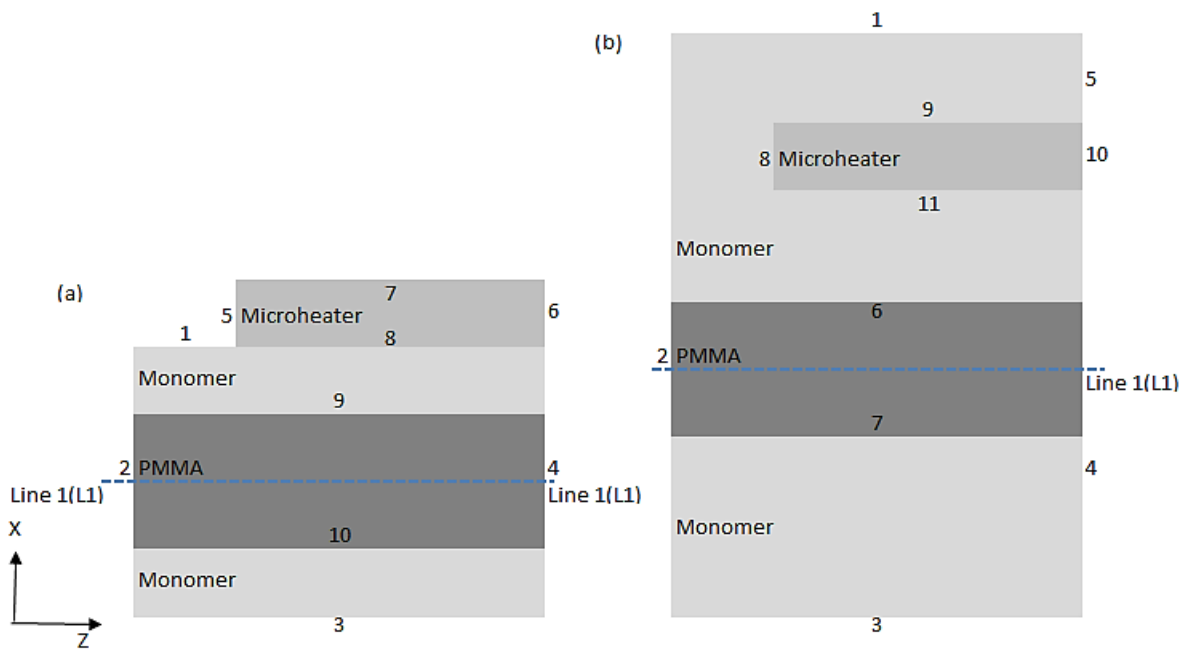

Figure 7.2: *Schematics of the planar PMMA waveguide geometry. (a) Microheater placed at the top of the upper cladding, (b) microheater buried within the upper cladding. The numbers relate to different boundary conditions as explained in the text. [102]*

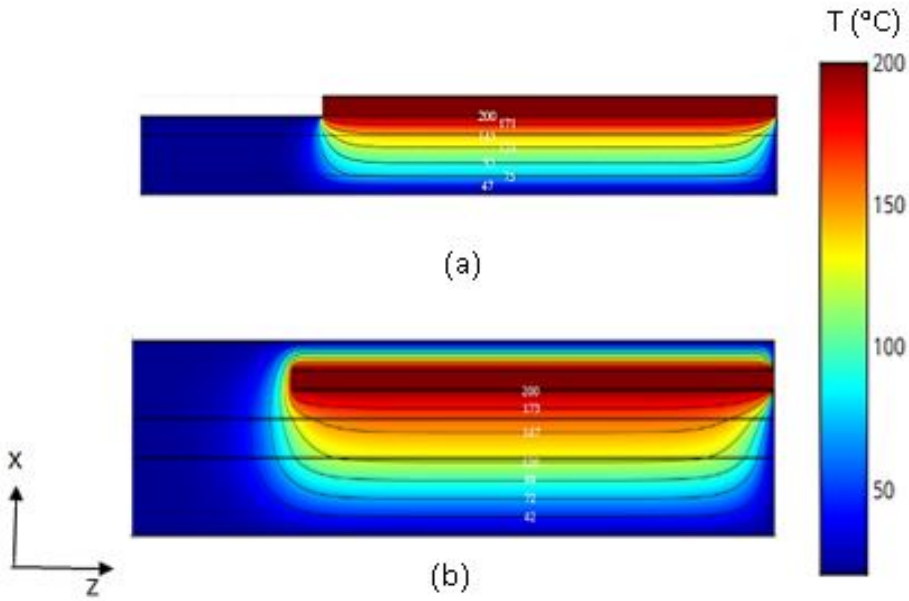

Figure 7.3: *Contour maps for the temperature distribution within the waveguides. (a) Microheater is at the top of the upper cladding, (b) microheater is buried inside the middle region of the upper cladding. [102]*

Material	ρ [kg/m3]	C_p [J/kg*°C]	k [W/m*°C]
Monomer	940	1890	0.147
PMMA	1190	1500	0.25
Polysilicon	2320	678	34

Table 7.1: *Model parameter values for the thermal simulation.*

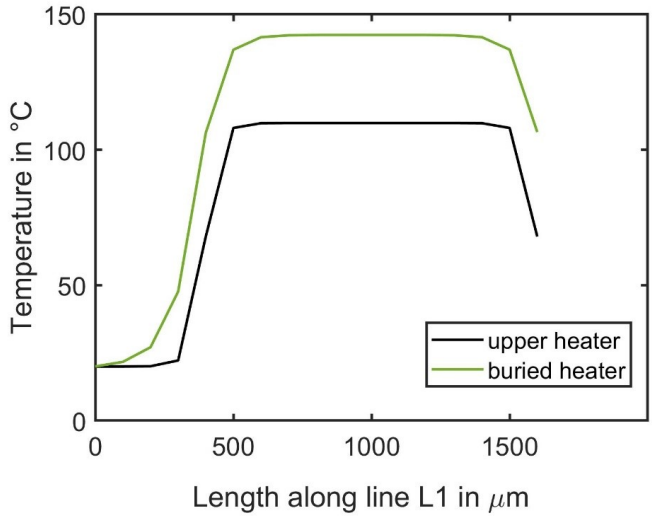

Figure 7.4: *The change in temperature distribution along the line L1 (central core axis along beam propagation direction) for the maximum microheater temperature at 200 ℃. (a) Upper heater, (b) buried heater. The heating time was 7ms. [102]*

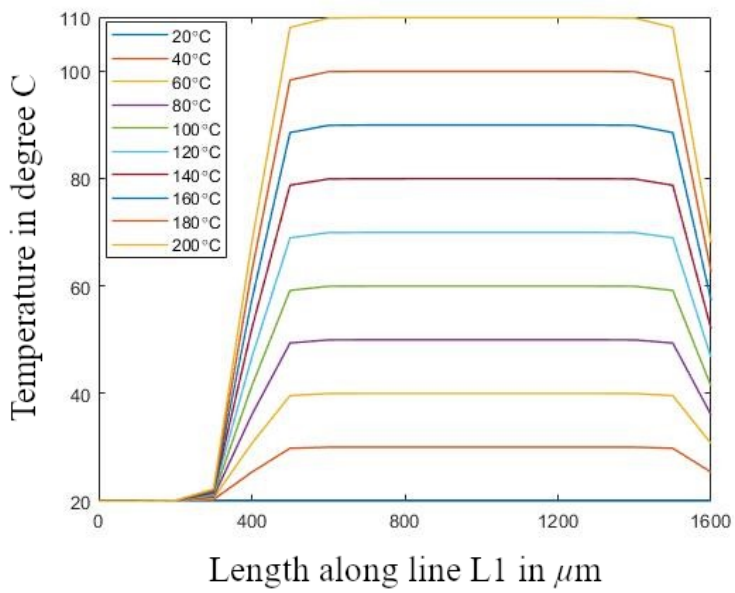

Figure 7.5: *Temperature modulation along the central beam propagation axis L1 when the temperature of the top microheater was varied between 20℃ to 200℃.[102]*

7.3 Thermal analysis of polymer waveguides

After conducting the thermal simulations, the contour maps for heat distributions of the waveguide were obtained for different temperature settings of the microheater. One such example of the contour map for the conductive heat transfer distributions within the waveguide when the microheater was at maximum temperature of 200°C is shown in Fig. 7.3. Fig. 7.3(a) displays the contour map for temperature distribution for the microheater at the top of the waveguide and Fig. 7.3(b) shows the contour map when the microheater was buried inside the middle part of the upper cladding. The change in temperature in the same layer along the central propagation z-axis, line L1, for the upper and the buried microheater models are shown in Fig. 7.4. At this stage, the microheater was at maximum temperature of 200°C. For the top microheater on the upper cladding model, the temperature along the line L1 was increased from 20°C to 110°C. The temperature along L1 for the buried microheater was

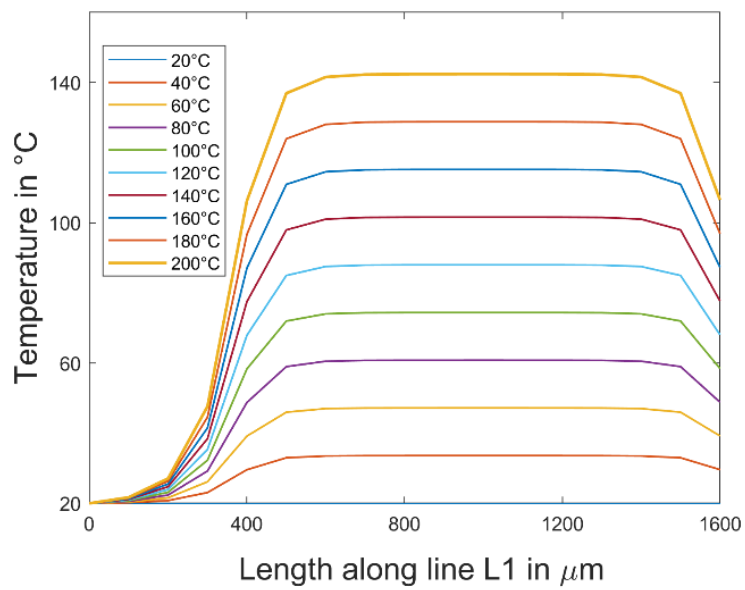

Figure 7.6: *Temperature modulation along the central beam propagation axis L1 when the temperature of the buried microheater was varied between* 20°*C to* 200°*C. [102]*

increased from 20°C to 148°C. A larger increase in the temperature along L1 for the buried microheater was thus observed.

When the microheater was placed on top of the waveguide, it provided controlled and better increase in temperature modulation along L1. However,

the embedded microheater design model could possibly be used to obtain a quicker response in switching time. For both cases, the microheater itself was at 200°C. The numerical solver remained static for almost all simulations. However, in one case the solver mode was changed to dynamic time dependence to check the spreading time of the heat throughout the waveguide. The spreading time was noted to be 7 ms in that case. Also, the temperature distribution along the reference line L1 shows a slightly smoother increase for the top microheater compared to the buried microheater case, see Fig. 7.4.

In real world calculations, it is very hard to implement a microheater within the cladding of a waveguide. Fig. 7.5 shows the gradual modulation in temperature increase along L1. The modulation in temperature change in the model 2 for the buried microheater when the temperature of the micrometer was increased from 20°C to 200°C is shown in Fig. 7.6. The increase in temperature along L1 is always proportional to the fixed temperature of the microheater. The buried microheater induced a larger increase in temperature along L1 than the microheater that was placed on the top of the waveguide. Zhang

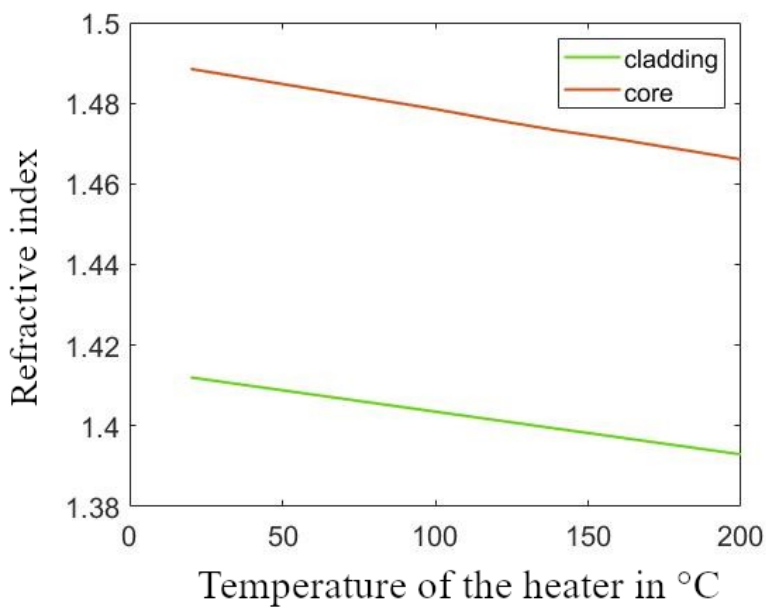

Figure 7.7: *Change in refractive index of the core and cladding of the polymer waveguide as the temperature of the microheater was varied between* 200°*C. [102]*

et al. demonstrated a linear relationship between the coefficients of thermal expansion (α) and the thermo-optic coefficient $\frac{\mathrm{d}n}{\mathrm{d}T}$ by evaluating many polymer materials including PMMA [94]. In our calculations, we considered the change

in refractive index as a function of temperature change of the waveguides. It is also described well in Ref. [94].

By considering the temperature distributions obtained from the thermal simulations, the refractive indices of the core and cladding of the waveguides were calculated. Here, the refractive index of the material as a function temperature was calculated by utilizing Eq. (7.4), [103].

$$n_{temp} = n_0 + n_0 * \frac{\mathrm{d}n}{\mathrm{d}T} * (T_1 - T_0) \tag{7.4}$$

where n_0 is the initial value of refractive index considered during the beginning of thermal simulations at room temperature. The new/updated value of refractive index is n_{temp} and was calculated from the change in temperature within the waveguide due to the heating process and also due to the effect of the thermo-optical coefficient.

The thermo-optic coefficient for PMMA was taken as $\frac{\mathrm{d}n}{\mathrm{d}T} = -1.3 \times 10^{-4}$°C. The initial room temperature is $T_0 = 20$°C and T_1 is the induced increase in temperature due to the heating by the microheater, as obtained from the solution of the finite element heat analysis. The initial values of the

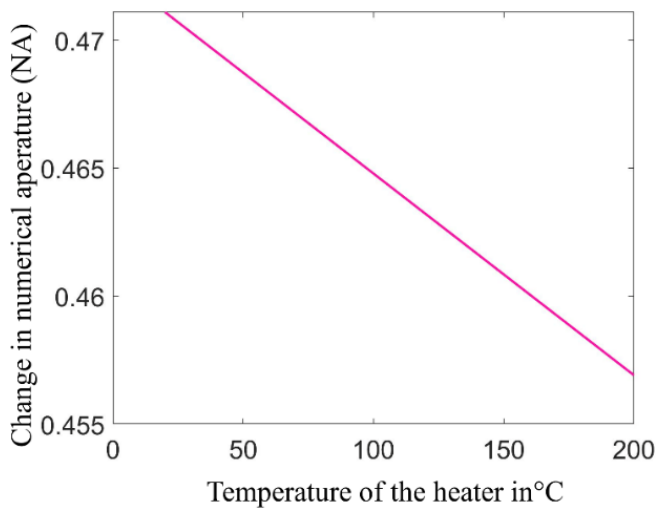

Figure 7.8: *Change in numerical aperture (NA) of the polymer waveguide as the temperature of the microheater was varied between* 200°*C.*

refractive indices of the PMMA core and monomer cladding were 1.48 and 1.41, respectively. The polymer material possess a negative thermo-optic coefficient, so there is a decrease in the refractive index value with an increase

in temperature, as it is also observed in the simulations. The change in the refractive index values during the heating process by the microheater is shown in the Fig. 7.7. A decrease in the refractive index value from 1.4885 to 1.4600 was observed, while the temperature of the microheater increased from $20 - 200°C$. The corresponding decrease in the refractive index for the cladding was from 1.412 to 1.392. The associated numerical aperture NA of the waveguide also decreased for the considered temperature range during the heating process, see Fig. 7.8. The NA of the waveguide was calculated by using $\mathrm{NA} = \sqrt{n_{core}^2 - n_{clad}^2}$. During the thermal simulation, the NA of the PMMA waveguide was decreased from 0.471 to 0.457. Also, there was a refractive index gradient across the core of the waveguide. However, it was not that significant due to the smaller core diameter. The size of the gradient across the core of the waveguide was $0.00015\,\mu m^{-1}$. There was also refractive index gradient across the waveguide and it was considered while performing the optical simulations.

7.4 Multi-physics thermo-optical simulations

Once the finite element analysis for the thermal distributions was finished, the subsequent computational waveguide models were transferred to the MATLAB to carry out the optical simulations by using the CN-BPM scheme. An initial Gaussian beam excitation at the input beam was provided to the PMMA waveguide core. The intensity of the input Gaussian beam was normalized to the maximum peak value of one. The different temperature distribution profiles of the PMMA waveguide are imported from the FEATool to further carry out the optical simulations. The Fig. 7.9 shows the beam intensity distribution profiles within the waveguide for the selected microheater temperature range between $60 - 180°C$, respectively. The decrease in the output intensity from the PMMA waveguide was not significant until the temperature of the microheater reached to 60°C. So, the beam intensity distributions profiles for the waveguide are provided from the temperature 60°C onwards of the microheater. The decrease in the output intensity became more prominent after 60°C. The localized maximum intensity points, also known as primary eyes, tend to move within the waveguide as light beam propagates through them indicating good light guiding properties.

We have observed back and forth movements of primary eyes within the PMMA core when the microheater was at selected temperature of 60°C, 80°C, 100°C, and 150°C respectively, see Fig. 7.9. In this case, it is an indication of changed beam propagation conditions as the transmitted intensity from the output of the waveguide core decreased continuously. When the microheater

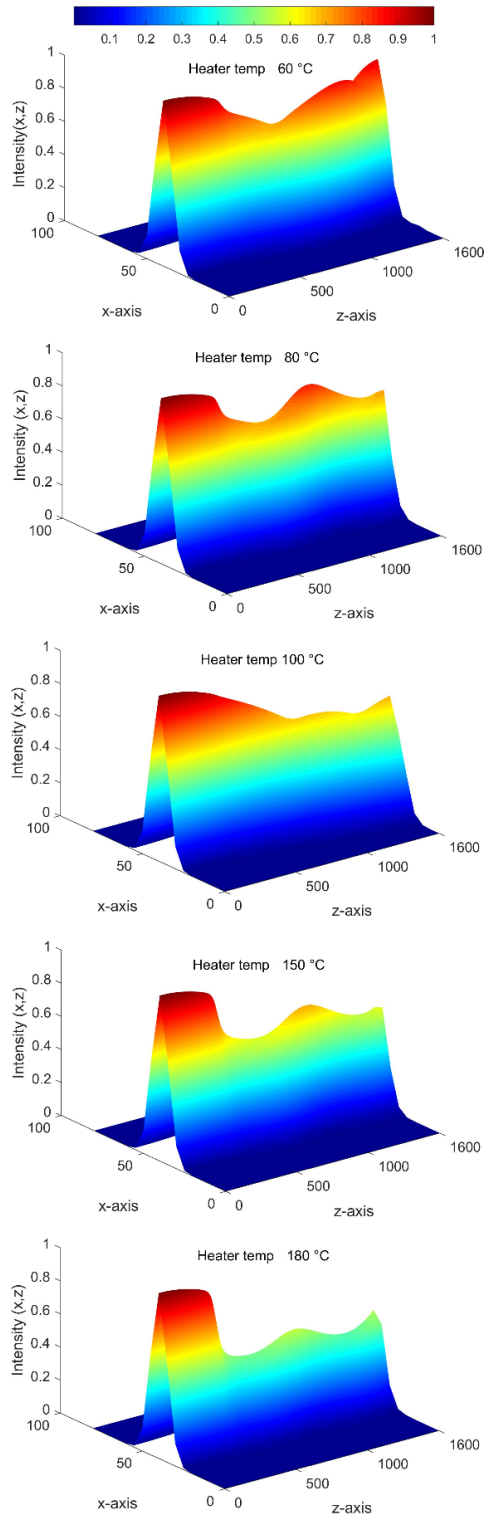

Figure 7.9: *Intensity distribution profiles of the propagating beam within the waveguide at different temperatures for the microheater. Units on the x-axis and z-axis are given in μm. The intensity I(x, z) is normalized to the maximum initial input intensity value of 1. [102]*

temperature was increased to 180°C, the primary eyes almost disappeared from the waveguide core having no localized maximum intensity points for them. For this temperature 180°C, the output intensity from the PMMA waveguide dropped below 50% of the initial beam intensity. The losses induced in the waveguide are because of the change in NA. Also, the residual stress is built up during the heating process which again increased the losses from the waveguides. However, we have assumed that the residual stress build up is less significant due to the small Young's modulus of the polymer material. The accumulated error could be larger than the actual physical process as the current simulation is a multi-step process. The change in refractive index of the material largely depends on its thermo-optic coefficient. In addition, the change in refractive index is very much influenced by the size of the microheater and the size of the wave-guiding element. The $\frac{\mathrm{d}n}{\mathrm{d}T}$ value of the PMMA was considered for cladding and core part of the waveguide in the current simulations. The thermo-optic coefficient could be different for different materials and could vary in actual physical processes.

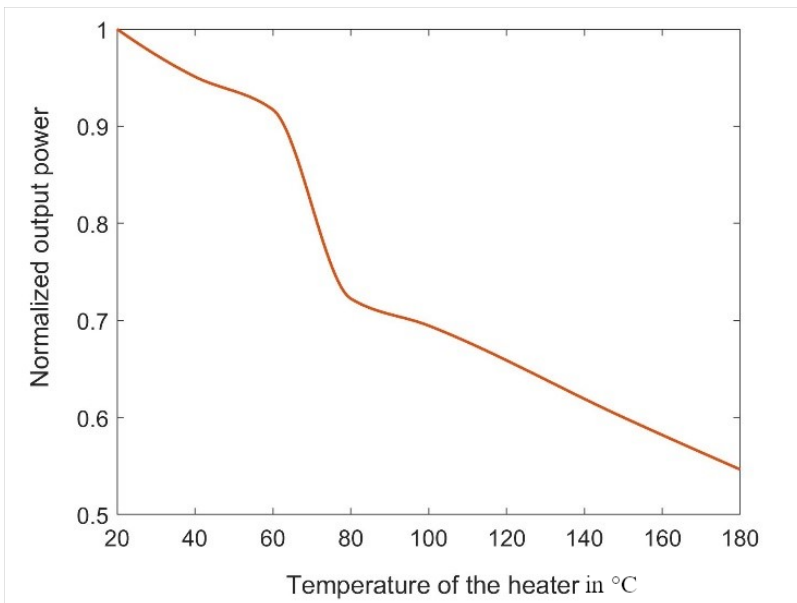

Figure 7.10: *Normalized output power from the exit port of the PMMA waveguide [102].*

In the next step, the output power from the exit port of the PMMA waveguide core was calculated for different selected temperature settings of the microheater. The last slice from the waveguide was taken out for each case and then the intensity value over the area was integrated to obtain the output power

at the exit port. The output power from the exit port of the waveguide was normalized and the loss in the intensity during the transmission was calculated. The calculated output power from the exit port is shown in the Fig. 7.10. As the heating of the waveguide by the microheater was increased, the normalized output power from the exit port of the waveguide was subsequently decreased, see Fig. 7.10. A sharper decrease in the output power was observed between $60 - 80°$C. For this temperature range, the PMMA material approaches the glass transition temperature [104]. The output power continued to decrease further and at 80°C the $P_{output} = 0.54 \times P_{input}$. When the temperature of the microheater continued to increase further to a higher temperature range, it caused a larger decrease in the refractive indices of the core and cladding and finally it was not possible to confine the beam to the waveguide core anymore. It was then diffusing to the surrounding medium.

7.5 Stress and deformation analysis

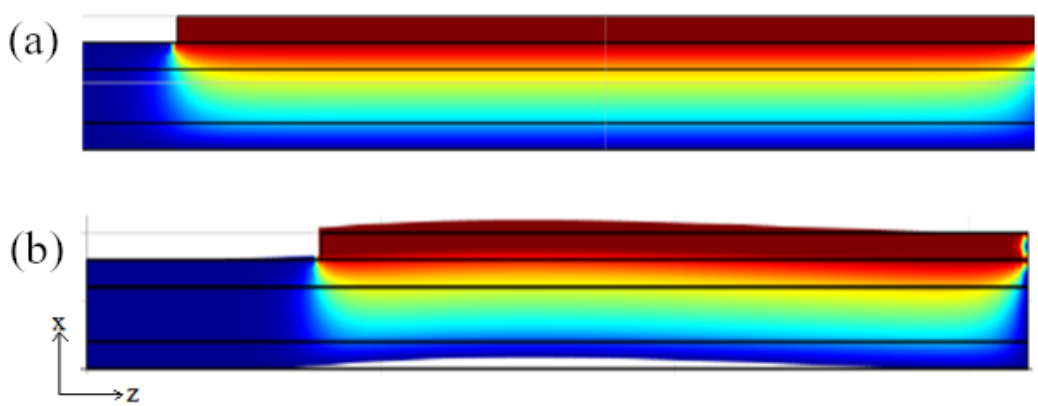

Figure 7.11: *(a) Initial PMMA waveguide at* $40°C$*, (b) deformed PMMA waveguide at* $200°C$ *[102].*

To access the performance of polymer materials in varying environmental conditions, it is very important to consider the elongations or deformations produced in the polymer-based integrated photonic devices. Thus for the integrity of performance, a link was established between the conductive heat analysis module for thermal distributions and the stress analysis module in the FEATool. Then the stress analysis was carried out for the same PMMA waveguide models. The corresponding elongations/deformations generated in the waveguide are quantified.

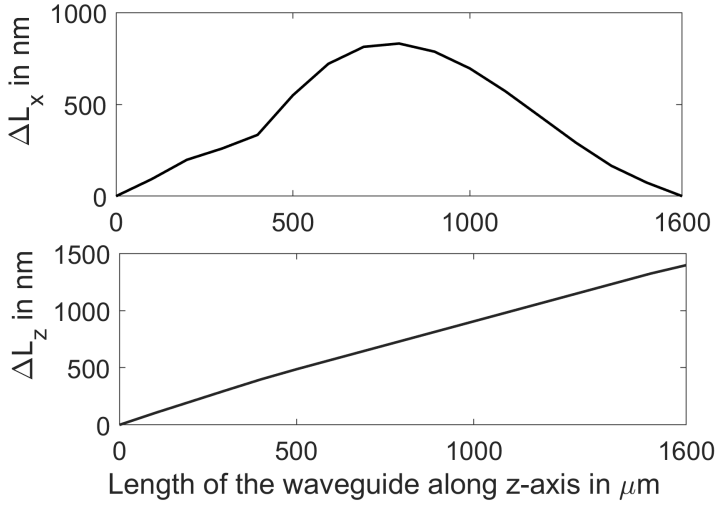

Figure 7.12: *Deformation in the PMMA waveguide when the heater was at* $200°C$ *(a) Displacement of the line L1 along the transverse x-axis:* $\Delta L_x = 831$ *nm, (b) displacement of the line L1 along the z-axis (propagation direction of the beam):* $\Delta L_z = 1397$ *nm [102].*

The finite element analysis solver of the multi-physics FEATool was used to perform the deformation and stress analysis. The plane stress module in particular was selected and proper boundary conditions were employed as well for the deformation analysis of PMMA waveguides. The left side and right side extremities were fixed in the design models, see Fig. 7.2(a). The boundary conditions such as fixing one end or both ends of the waveguide during the deformation analysis is crucial. We considered to fix both extremities of the optical waveguide during the stress and deformation analysis as it provided a better practical approach. Usually the optical waveguides or interconnects are placed between two fixed active components such as between laser diodes LDs or between waveguides in integrated photonic circuits. The heat transfer module was coupled to the plane stress module of the FEATool to perform the thermo-mechanical multi-physics simulations. The initial temperature of the waveguide was considered as 20°C, the same as for the earlier thermal simulations for deformation analysis. The parameter values utilized to conduct the stress analysis is provided in the TABLE 7.2.

Here, E is the Young's modulus, ν is Poisson's ratio that signifies the ratio between the transverse contraction strain to the longitudinal extension strain in the direction of stretching force and ρ is the material density, as provided in

Material	E [GPa]	ν	αK^{-1}
Monomer	3.3	0.40	$72.22 * e^{-6}$
PMMA	2.76	0.37	$22.25 * e^{-6}$
Polysilicon	160	0.22	$2.6 * e^{-6}$

Table 7.2: *Model parameter values for stress analysis.*

Table 7.2. α is the thermal expansion coefficient.

As can be expected, the maximum deformation was induced in the waveguide when the microheater was at a temperature of 200°C. There was no deformation at the initial stage when the microheater was at 40°C, as shown in Fig. 7.11(a). Fig. 7.11(b) shows the deformed waveguide when the microheater was at 200°C. The elongations produced in the design model during the deformation analysis due to the heating by the microheater at 200°C is presented in the Fig. 7.12. The elongation produced along the transverse x axis is shown in the Fig. 7.12(a). A maximum elongation $\Delta L_x = 831\,\text{nm}$ is produced along the transverse x direction when the microheater was at the maximum temperature of 200°C. The elongation generated along the propagation beam direction z axis is shown in Fig. 7.12(b). A maximum elongation $\Delta L_z = 1397\,\text{nm}$ was induced due to the maximum heating by the microheater. Compared to the original dimensions of the waveguide, the elongations along x and z axis are small. The residual stress that built up in the waveguide was considered less severe due to the small Young's modulus of polymer material. The effect of the residual stress was thus not included in the BPM simulations.

The combined influence on the waveguide geometry, numerical aperture and refractive index was studied. Furthermore, the mechanical stress generated due to induced thermal loads along the axial and transverse beam directions were determined. In general, a relatively simple model was investigated where the change in refractive index of the polymer waveguide was induced by the change in temperature setting of the microheater. This leads to the variation in the carried beam intensities, which in turn, resulted in the built up of the mechanical stress due to the heat producing elongations in the dimensions of the waveguide.

Chapter 8

Summary and Outlook

8.1 Summary

In the scope of this PhD thesis, extensive research on polymer photonic devices was performed. The aim was to develop a multi-scale and multi-physics simulation approach to simulate the formation of polymer-based photonic components and their optical properties as function of ambient parameters such as temperature. In particular the interaction of the monomer/polymer material with light, the induced polymerization process and the influence of temperature on the optical properties were investigated. At first, various numerical methods were implemented to build a customized research code to simulate polymer waveguides. In this context, a CN-BPM scheme (along with TBC) in 2D was implemented to compute the light intensity distributions for photonic structures. The implemented code was validated against a commercial software tool RSOFT by simulating and comparing the corresponding results for some bench-marking photonic components, such as, Y-branches, straight waveguides, bent waveguides and Mach-Zehnder interferometers.

Systematic parameter studies, such as on the mode-mismatch loss, power attenuation, number of guided modes and the effective refractive indices for the mentioned bench-marking photonic components were carried out by using self-developed Matlab scripts. Experimentally, waveguide fabrication based on self-writing was exploited to create polymer-based waveguides in the samples. This is a very promising technique to fabricate a waveguide by the self-action of the light that incorporates self-focusing and self-trapping effects.

To obtain the dynamic value of the refractive index modulation, two kinds of material models named phenomenological model and diffusion material model, were implemented. A comparative study on the theoretical predictions from the

two kinds of material models for simulating a straight SWWs and a bent SWWs was discussed. The results from the simple phenomenological model 1 nearly match with the results obtained from the more complex diffusion based material model 2, with a few exceptions noticed in the uniformity and the bending of the SWWs [86]. The SWWs created using the diffusion based material model show smoother, more uniform surfaces and show more bending compared to the SWWs created using the phenomenological model. The curing time of bent SWWs is provided for both models showing that model 1 yields a faster increase in refractive index in comparison to model 2. Also, the self-written structures become filamentous when the nearby region starts to polymerize as the evolution in refractive index is near to the maximum or saturation value.

In further studies, various numerical investigations on bent SWW couplers were performed by using the diffusion material model. The bent SWW was created by two opposing laser beams when propagated into the photo-polymer mixture having an offset along their transverse x direction. The diffraction or spreading of light was compensated due to the modulation in refractive index that originated because of the self-focusing effect of the laser beams. A numerical study was also carried out to find the optimal exposure time that was essential to form a SWW which also links to the optimal refractive index change.

In addition, a numerical study was carried out to find the optimal refractive index modulation of a SWW which leads to best light guiding. The optimum modulation in the refractive index $\Delta n = 0.001$ and $\Delta n = 0.005$ were determined for the material which was necessary to form a SWW. A non-continuous intensity distribution for the bent SWW evolved when the refractive index modulation was increased beyond 0.005. Similar effects were also observed when the separation distance between the counter-propagating beams increased beyond a certain value. However, these two cases are demonstrated as limiting cases to obtain the optimum refractive index modulation value and also to obtain the maximum possible propagation distance z for the specific input beam profiles.

The refractive index modulation and the dynamics of corresponding intensity distribution profiles were studied. It was found that the quality of light guidance is related to the formation of intensity maxima inside the SWW, also referred to as primary eyes. An interesting investigation was accomplished to limit the vertical offset tolerance for counter-propagating identical beams, each having beam diameters of 20 µm and a lateral offset of 20 µm between them. It was demonstrated in the offset tolerance study that the bent SWW coupler was only created when the propagation distance between the sources was increased from 1,000 µm to 5,000 µm. Further simulations were carried out for more

offset values ranging from 15 µm to 30 µm to obtain the minimum coupling length of the SWWs. The width and the curvature of these bent SWWs were influenced because of the impact of the divergence of Gaussian beams. The width decreased and the curvature of the bent SWWs increased as the propagation distance between the opposing beams is increased. This was validated during the simulations by considering different coupling lengths of the bent SWWs. Also, one study was carried out to determine the curing time of the bent SWW that was largely influenced by control parameters, such as rate constant and component concentrations of the photo-polymer in the photo-polymer mixture during the simulation process. These numerical investigations enhanced the understanding on the refractive index modulation, shape i.e, width as well as curvature, offset compensation and the curing time during the formation of bent SWWs.

The relevant effects of the self-writing process for optical interconnects inside a single photo-polymer resin were investigated theoretically and as well as experimentally. The self-focusing and self-trapping phenomenon was observed during the fabrication process of the SWWs in experiment and also in simulation. The transmitted power during the fabrication of the SWW was recorded in experiment for a time duration of 10 min which is then later compared to the obtained transmitted power in simulation of the same SWW using a diffusion material model. Various optical interconnects with lengths between 0-1,000 µm are fabricated and their losses were measured in experiment. We find an attenuation coefficient $\alpha_{experiment} = (8.43 \pm 0.3) \times 10^{-5}$ dB/ µm which is in good agreement with the predicted attenuation coefficient of $\alpha_{simulation} = 7.93 \times 10^{-5}$ dB/ µm. The dB losses are calculated from the measured data for the case of an air-gap between the multi-mode fibers. The obtained attenuation coefficient α_{air} was at 10^{-3} dB/ µm which is 11 times higher than the attenuation of the SWWs.

Another study focused on the thermo-mechanical and optical study of polymer waveguide structures, that defines a combined simulation approach. Two models were designed where a polysilicon microheater was incorporated into the waveguide. Either the microheater was located at the top or inside of the upper cladding of the polymer PMMA waveguide. The FEATool box was used to perform finite element analysis to obtain mechanical deformations and heat distributions within the waveguides. The finite difference approach with the CN-BPM scheme was adapted in MATLAB to carry out the optical simulations.

The simulation results obtained from the FEATool box were coupled back with the MATLAB module. The light beam distributions of the PMMA waveguides were affected significantly due to the modulation in heat distribution

by the microheater. The polymer material is very much sensitive to the external environmental changes. The influence of the thermo-optic coefficient on the thermal distributions was considered and the refractive indices of the core and cladding of polymer waveguide calculated. The NA of the polymer PMMA waveguide was decreased from 0.471 to 0.457 during the heating process. The beam intensity profiles within the PMMA waveguides at different microheater temperature settings are determined. When the microheater was increased beyond 180°C, the primary eyes or maximum intensity localized points were no longer visible. The movement of primary eyes signifies the good beam carrying capabilities of the waveguide. At this point, the normalized power from the exit port of the waveguide decreased to $0.54 * P_{input}$. No significant change in the output power was observed till the microheater temperature reached 60°C. Afterwards, the normalized output power from the exit port of the waveguide also decreased consequently due to heating. Furthermore, the deformations were computed and maximum deformations along transverse x and propagation z directions was obtained for the waveguide models by keeping the end facets tight at fixed points.

8.2 Outlook

The conducted study provides a firm ground to clearly understand the underlying effects in polymer-based photonic components in integrated photonic circuits for next generation of telecommunication networks or sensors. One such example for a highly functional photonic sensor network in thin polymer foils is shown in Fig. 8.1. The work presented here paves the way for many further research perspectives. The simplest scenario was adapted to implement a 2-dimensional finite difference base CN-BPM scheme to simulate the intensity distributions for optical waveguides in the presented research. However, it is surely advisable to implement a 3-dimensional full vectorial CN-BPM scheme along with proper boundary conditions that would describe the optical simulations for real world photonic components more precisely.

One could also adapt FFT-BPM or wide-angle BPM schemes for the optics simulation and could perform a comparison study among the mentioned schemes with the CN-BPM approach. That will give a confirmation on a method that best suits for optical simulations of polymer photonic components. Multi-beam propagation by using the CN-BPM scheme along with the material model is an interesting approach that can be used to simulate more than two SWWs. Three and five beam propagation in the computational domain was carried out to create 3 to 5 SWWs within the material sample, as shown in chapter 4.

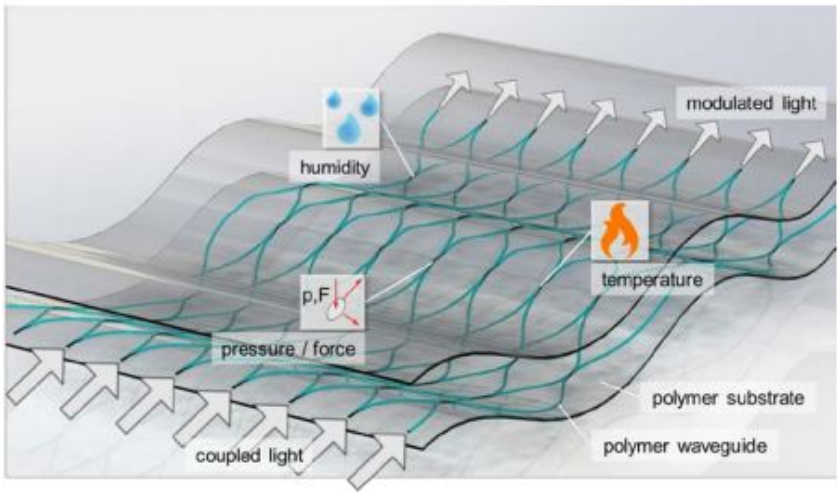

Figure 8.1: *Visionary example for a planar polymer-optical sensor network for 2D distributed measurement of quantities such as pressure/force, humidity and temperature. The quantities to be detected are converted into optical signals thereby omitting electronic components as far as possible. In future, such sensors networks could be manufactured in an R2R process, for example, featuring high multiplexing capabilities and spatial resolution [105].*

However, the research work was limited to simulate straight or bent SWWs. It would be intersting to extend the multi beam propagation technique further to simulate complicated advanced photonic structures such as X, Y-junctions and resonators for the photonic chips. Fig. 8.2 shows the experimental results by colliding two self-written waveguides [22]. The merging of beams was controlled by the collision angle, beam power and time delays between them to create structure like Y-branch.

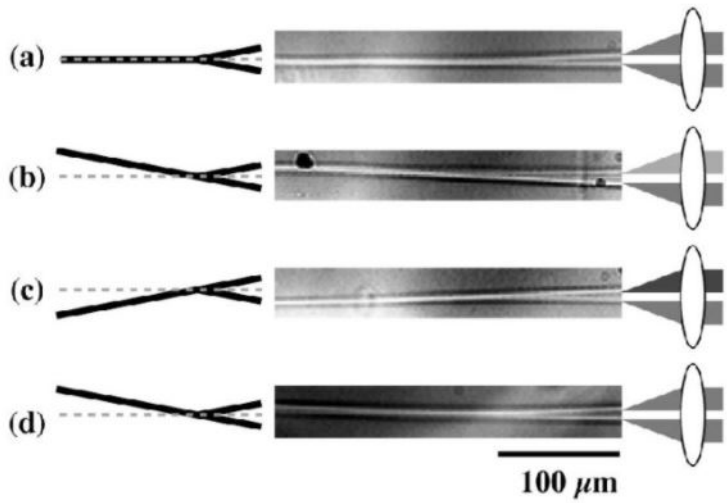

Figure 8.2: *Experimental data showing collisions between two self-written waveguides. The power of the lower beam is 0.1 mW; the power of the upper beam is (a) and (d) 0.1 mW, (b) 0.07 mW, and (c) 0.13 mW. The time delay between the lower and upper beams is (a)-(c) 0 s, and (d) 2 s [22]*

All experiments presented in chapter 6 were carried out in the HOT lab by using the one-polymer approach with an epoxy-based acrylate SynIII material. In the one-polymer approach, only one polymer sample material was used to cure both the core and cladding parts of the polymer SWW during its fabrication process. Further research is required to try out other promising available polymer materials by adopting one-polymer or two-polymer approaches. Of-course it is possible to tweak the implemented material models as per the requirements from the two-polymer approach. Then the new experimentally validated model of the writing process will enable to study the fabrication of optimized SWW interconnects in future that is crucial for achieving high performance interconnects.

The influence of temperature load and stress on the dynamics of refractive

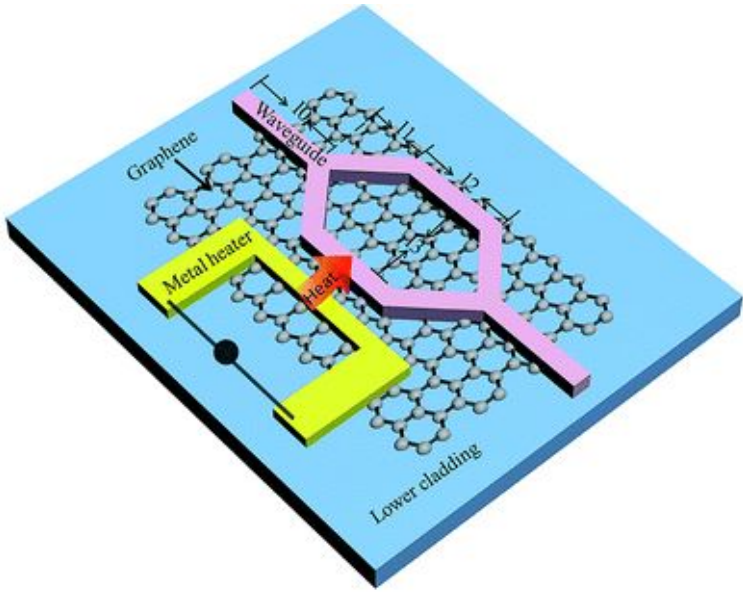

Figure 8.3: *The structure of the polymer thermal optical switch with a graphene-assisted heating layer[106]*

index modulation of polymer waveguide is very crucial in understanding the corresponding relevant effects related to operating environmental stability conditions, specially for thermo-optical switches and polymer base planar sensor networks. A hybrid thermo-optical switch based on a Mach–Zehnder interferometer structure which consists of a polymer-based waveguide core, metal electrodes and graphene assisted heating layer is shown in the Fig. 8.3. The study was performed by Sun et al. to optimize the switching power consumption and switching time to realize a switching function through the thermo-optic effect. The current research work was limited to opto-mechanical analysis for planar PMMA wave-guides. Further interesting research work could be carried forward on performing thermal, optical and deformation/stress analysis on other 3D complex waveguide geometries consisting of promising hybrid polymer material samples. Simultaneously, the experimental validation for the thermo-mechanical simulations could be performed. One should make note of the dimension of the components, e.g. the size of the microheater and width of the core and cladding part of the waveguide during thermo-mechanical-optical simulations, as they tend to influence the simulation results to large extent.

List of Figures

1.1 Photonics integration: (a) In 2008: IBM's former No. 1 supercomputer ROADRUNNER with optics (AOCs) at the board edge only. (b) In 2011: IBM's HPC system POWER 775 with many optical transceivers assembled on carriers and a huge number of fibers connected with the board edge. (c) Current research: optical polymer waveguides connecting photonics chips assembled on carriers with the carrier edge, other carriers, and board edge. [2] 2

1.2 Emerging photonic market by products over a forecast period, see Ref. [7] 3

1.3 Schematic diagrams of the fully embedded board-level optical interconnection system. (a) 3-D cross-sectional view of an optical layer-interposed PCB. (b) 12-channel optical waveguide film layer with an integrated thin-film VCSEL and p-i-n photodiode arrays. [10] 4

1.4 Schematic of different photonic components, used in photonic integrated circuits. For more information, see Ref. [11] 5

2.1 (a) Planar optical 2D waveguide, 1d transverse optical confinement (b) channel waveguide 3D with 2-d transverse x, y confinement, taken from Ref. [28]. 9

2.2 Some types of channel waveguides (a) raised, (b) graded-index embedded, and (c) buried. [29] 9

2.3 Various optical components using modified channel waveguides. TE, transverse electric; TM, transverse magnetic. [30] 10

2.4 The basic structure and refractive index profile of a optical planar step-index waveguide [32]. 11

3.1 Fast optical field amplitude variation along the propagation z axis and slowly varying envelope amplitude (dashed line), taken from [66] 22
3.2 The BPM algorithm is applied to determine the field at the $z + \Delta z$ plane when the discretized field at the transversal plane at position z is known already [66]. 23
3.3 The field along the transverse direction (x), for a fixed longitudinal coordinate z on a linear grid for the 2D FD-BPM. u_j is the optical field at position x_j. The x-axis is discretized into N discrete points and Δx is the step size. 24
3.4 Input Gaussian beam excitation to the straight waveguide. . . 29
3.5 Gradient refractive index profile of the straight waveguide. . . 29
3.6 Beam intensity while propagating the Gaussian beam through the straight waveguide using CN-BPM scheme. 30
3.7 Beam intensity profile while propagating a Gaussian beam through the straight waveguide in RSOFT. 31
3.8 Output intensity amplitudes are compared between CN-BPM scheme and RSOFT tool for simulating of a straight waveguide. 32
3.9 The input Gaussian beam excitation to the bent waveguide. . 33
3.10 The refractive index profile for the cosine bent and the corresponding beam intensity profile while propagating the Gaussian beam by using the CN-BPM scheme. 33
3.11 Beam intensity profile while propagating a Gaussian beam through the cosine bent waveguide in RSOFT. The panel on the right side is the pathway monitor in RSOFT that shows the compressive calculation of monitored transmitted power of the propagating mode (green line). The normalized power is 1, shown by the blue line. 34
3.12 Output intensity amplitudes are compared between the CN-BPM scheme and RSOFT tool while simulating a cosine bent waveguide. 34
3.13 The monitored normalized power by propagating a Gaussian beam through the bent waveguide from the CN-BPM simulations. 35
3.14 The refractive index profile of the Y-branch. 36
3.15 The input Gaussian beam excitation along the transverse x-axis to the Y-branch. 36
3.16 The beam intensity profile of the Y-branch from the CN-BPM simulation. 37

3.17 The RSOFT simulation results for the Y-branch. The intensity beam profile and the corresponding monitored normalized power during simulation. The panel on the right side is the pathway monitor in RSOFT that shows the compressive calculation of monitored transmitted power of the propagating mode (green line). The normalized power is 1, shown by the blue line. . . . 38
3.18 The comparison between the obtained output modes in the beam intensity profiles from the CN-BPM and RSOFT simulations for the Y-branch. 38
3.19 The 1D Gaussian input beam excitation along the transverse x axis to the Mach-Zehnder interferometer. 39
3.20 The refractive index profile of the Mach-Zehnder interferometer in the (x, z) plane. 40
3.21 The obtained intensity distribution after simulating the Mach-Zehnder interferometer using the CN-BPM scheme. 41
3.22 The Mach-Zehnder interferometer was simulated using the RSOFT tool. The left side panel shows the beam intensity profile. The panel on the right side is the pathway monitor in RSOFT that shows the compressive calculation of monitored transmitted power of the propagating mode (green line). The normalized power is 1, shown by the blue line. 42

4.1 The beam self clean-up in long distance propagation by using the phenomenological model. A Gaussian beam with a diameter of 250 µm propagated for a distance of 100 mm. (a) Input beam excitation, (b) A lot of diffraction with slight refractive index modulation at the beginning, (c) self-focusing of the beam, (d) complete beam self clean up happened and a permanent SWW is evolved. 45
4.2 The refractive index modulation during the beam clean-up process, that is shown in the Fig. 4.1. A Gaussian beam with a diameter of 250 µm was propagated for a distance of 100 mm. The simulation was performed for total of 3,000 time steps till complete evolution of the SWW. 47
4.3 The dynamics of the evolution of the monomer concentration profile in a temporal loop during numerical simulation. The temporal behaviour of the monomer concentration reflects the formation of a self-written waveguide in the region exposed to the writing light beam. 49

4.4 The dynamics of evolution of polymer concentration profile in a temporal loop during the numerical simulation. The temporal behaviour of the polymer concentration reflects the formation of a self-written waveguide in the region exposed to the writing light beam. 50
4.5 The temporal dynamics of the refractive index modulation during numerical simulation (conducted for 100 s) in the diffusion model. 51
4.6 Simulated bent SWW using the phenomenological material model. The refractive index modulation of the evolving core of the SWW is on the left side, the corresponding intensity distributions are on the right side. The intensity was normalized to the maximum intensity of the Gaussian input beam [86]. . . 55
4.7 Simulated bent SWW using the diffusion based material model. The refractive index modulation of the evolving core of the SWW is on the left side, the corresponding intensity distributions are on the right side. The intensity was normalized to the maximum intensity of the Gaussian input beam [86]. 56
4.8 The change in refractive index with the curing/writing time for a bent SWW obtained using model 1 and model 2, respectively. 57
4.9 Numerical simulation of a straight SWW within the given material mixture using the phenomenological model. (a) initial normalized light intensity distribution, (b) light intensity distribution after self-focusing of the Gaussian beam, and (c) light intensity distribution when the Gaussian beam is self-trapped [86] 58
4.10 Numerical simulation of a straight SWW within the given material mixture using the diffusion based material model. (a) initial normalized light intensity distribution, (b) light intensity distribution after self-focusing of the Gaussian beam, and (c) light intensity distribution when the Gaussian beam is self-trapped [86]. 58
4.11 Filamentous nature of a bent SWW when the nearby region started to polymerize. The result is obtained from the diffusion model [86]. 59
4.12 3 Gaussian beams are propagated in the photo-polymer material. 60
4.13 5 beams are propagated in the photo-polymer material. 61

5.1 Schematic diagram of the writing process of a bent SWW. . . 64
5.2 Temporal dynamics of the refractive index change $\triangle n$ of 0.001, 0.005, 0.01 and 0.02 (from top to bottom) (a) and corresponding normalized intensity profiles (normalized I) at times t = 14 s, 34 s, 53 s and 98 s, respectively (b). [45]. 66

5.3 Refractive index modulation on the left and normalized intensity profile (normalized I) on the right column. (a) Offset is 20 µm, coupling length is 1,000 µm (b) Offset is 20 µm, coupling length is 5,000 µm. [45] 69
5.4 Minimum separation distance between the sources along the z axis required to compensate the lateral offset along the transverse x axis. [45] 71
5.5 Refractive index modulation $\triangle n$ (on top) and normalized beam intensity I (on bottom) when the misalignment between counter propagating beams is 30 µm. [45] 72
5.6 Normalized intensity profiles for bent SWWs having a coupling length of 1 mm, 5 mm and 10 mm, respectively (left to right). [45] 74
5.7 Temporal dynamics of change in refractive index Δn values for component concentration ratios (m:p:a) within the photopolymer mixture of 95 : 2 : 3, 55 : 42 : 3 and 25 : 72 : 3, respectively. Here, m, p, and a stand for monomer, polymer, and photoinitiator, respectively. [45] 75
5.8 Temporal dynamics of the change in refractive index Δn for rate constant k_r values 0.005, 0.001, 0.01 and 0.02, respectively. [45] 76

6.1 Schematic of the experimental set-up for fabrication of SWWs. CCD : Charged Coupled Device, PD : Power Detector. 79
6.2 Process steps involved to write the SWWs. Images were captured after the polymer and lasers are applied. 79
6.3 Characterization experimental set-up. 80
6.4 (a) An SWW with a length 1800 µm is created by a laser beam at 638 nm with 15 mW power from a MM fiber having a 50 µm core diameter, (b) the traced path remained in the sample after the removal of excitation source. [46]. 81
6.5 (a) A 235 µm SWW created between MM fibers (different diameters) at a wavelength of 406 nm and a power of 800 µW. (b) A beam at 638 nm propagates in the existing SWW channel.[46] 82
6.6 Evolution of a straight waveguide in experiment. The panels show the evolution process of the waveguide as function of time [46] 82
6.7 Evolution of a straight waveguide in the simulation. Vertical length is from 0 to 2 mm, and the horizontal length is from 0 to 100 µm. [46] 83

6.8 Transmitted power during the writing process. (a) Transmitted power as recorded by the power detector for a 340 µm long SWW in experiment. (b) Normalized output power for a 340 µm long SWW in the simulation [46]. 86
6.9 Loss measurements at 638 nm for polymer SWWs from experiment and simulation. [46] 88
6.10 Loss measurements at 638 nm for the case of an air gap between the fibers in experiment. [46] 90

7.1 A prototype design of an polymer optical PCB with optoelectronic VLSI circuitry [92]. 92
7.2 Schematics of the planar PMMA waveguide geometry. (a) Microheater placed at the top of the upper cladding, (b) microheater buried within the upper cladding. The numbers relate to different boundary conditions as explained in the text. [102] 96
7.3 Contour maps for the temperature distribution within the waveguides. (a) Microheater is at the top of the upper cladding, (b) microheater is buried inside the middle region of the upper cladding. [102] 97
7.4 The change in temperature distribution along the line L1 (central core axis along beam propagation direction) for the maximum microheater temperature at 200 ℃. (a) Upper heater, (b) buried heater. The heating time was 7ms. [102] 98
7.5 Temperature modulation along the central beam propagation axis L1 when the temperature of the top microheater was varied between 20℃ to 200℃.[102] 98
7.6 Temperature modulation along the central beam propagation axis L1 when the temperature of the buried microheater was varied between 20°C to 200°C. [102] 99
7.7 Change in refractive index of the core and cladding of the polymer waveguide as the temperature of the microheater was varied between 200°C. [102] 100
7.8 Change in numerical aperture (NA) of the polymer waveguide as the temperature of the microheater was varied between 200°C. 101
7.9 Intensity distribution profiles of the propagating beam within the waveguide at different temperatures for the microheater. Units on the x-axis and z-axis are given in µm. The intensity I(x, z) is normalized to the maximum initial input intensity value of 1. [102] 103

7.10 Normalized output power from the exit port of the PMMA waveguide [102]. 104
7.11 (a) Initial PMMA waveguide at 40°C, (b) deformed PMMA waveguide at 200°C [102]. 105
7.12 Deformation in the PMMA waveguide when the heater was at 200°C (a) Displacement of the line L1 along the transverse x-axis: $\Delta L_x = 831$ nm, (b) displacement of the line L1 along the z-axis (propagation direction of the beam): $\Delta L_z = 1397$ nm [102]. . . 106

8.1 Visionary example for a planar polymer-optical sensor network for 2D distributed measurement of quantities such as pressure/force, humidity and temperature. The quantities to be detected are converted into optical signals thereby omitting electronic components as far as possible. In future, such sensors networks could be manufactured in an R2R process, for example, featuring high multiplexing capabilities and spatial resolution [105]. 112
8.2 Experimental data showing collisions between two self-written waveguides. The power of the lower beam is 0.1 mW; the power of the upper beam is (a) and (d) 0.1 mW, (b) 0.07 mW, and (c) 0.13 mW. The time delay between the lower and upper beams is (a)-(c) 0 s, and (d) 2 s [22] 113
8.3 The structure of the polymer thermal optical switch with a graphene-assisted heating layer[106] 114

List of Tables

2.1 Comparison between polymer and glass wave-guides 18

7.1 Model parameter values for the thermal simulation. 97
7.2 Model parameter values for stress analysis. 107

Bibliography

[1] D.A.B. Miller. Physical Reasons for Optical Interconnection. *Int. J. Optoelectron*, 11:155–168, 1997.

[2] R. Dangel, J. Hofrichter, F. Horst, D. Jubin, A. La Porta, N. Meier, I. Soganci, J. Weiss, and B. Offrein. Polymer waveguides for electro-optical integration in data centers and high-performance computers. *Opt. Express*, pages 4736–4750, 2015.

[3] B. J. Offrein, C. Berger, R. Beyeler, R. Dangel, L. Dellmann, F. Horst, T. Lamprecht, N. Meier, R. Budd, F. Libsch, and J. Kash. Parallel optical interconnects in printed circuit boards. *Proc. SPIE 5990*, 2005.

[4] F. E. Doany, C. L. Schow, C. W. Baks, D. M. Kuchta, P. Pepeljugoski, L. Schares, R. Budd, F. Libsch, R. Dangel, F. Horst, B. J. Offrein, and J. A. Kash. 160 Gb/s bidirectional polymer-waveguide board-level optical interconnects using CMOS-based transceivers. *IEEE Trans. Adv. Packag.*, page 345–359, 2009.

[5] M. A. Taubenblatt. Optical interconnects for high-performance computing. *J. Lightwave Technol.*, page 448–457, 2012.

[6] F.A.P. Tooley. Challenges in optically interconnecting electronics. *IEEE Journal of Selected Topics in Quantum Electronics*, 2:3–13, 1996.

[7] Photonics market analysis by product (waveguides, optical modulators, optical interconnects, leds, wavelength division multiplexer filters, photo detectors, lasers, amplifier), by application (consumer electronics, displays, safety defense technology, communication, metrology, sensing, medical healthcare, high-performance computing) and segment forecasts to 2024. `https://www.grandviewresearch.com/industry-analysis/photonics-market`, 2016.

[8] Mikko Karppinen. *High bit-rate optical interconnects on printed wiring board. Micro-optics and hybrid integration: Dissertation.* PhD thesis, 2008.

[9] Xingcun Colin Tong. *Advanced Materials for Integrated Optical Waveguide.* Springer International Publishing, 2013.

[10] J. H. Choi, L. Wang, H. Bi, and R. T. Chen. Effects of Thermal-Via Structures on Thin-Film VCSELs for Fully Embedded Board-Level Optical Interconnection System. *IEEE J. Sel. Top. Quantum Electron.*, pages 1060–1065, 2006.

[11] Bahaa E A Saleh and Malvin Carl Teich. *Fundamentals of photonics; 2nd ed.* Wiley series in pure and applied optics. Wiley, New York, NY, 2007.

[12] W.M. Pätzold, C. Reinhardt, A. Demircan, and U. Morgner. Cascaded-focus laser writing of low-loss waveguides in polymers. *Opt. Lett.*, 41:1269–1272, 2016.

[13] K. Tung, W. Wong, E. Pun. Polymeric optical waveguides using direct ultraviolet photolithography process. *Appl. Phys.*, 80:621–626, 2005.

[14] S. Zakariyah, P. Conway, D. Hutt, D. Selviah, K. Wang, J. Rygate, J. Calver, and W. Kandulski. Fabrication of polymer waveguides by laser ablation using a 355nm wavelength Nd:YAG laser. *J. Lightwave Technol.*, 29:3566–3576, 2011.

[15] M. Rezem, A. Günther, M. Rahlves, B. Roth, E. Reithmeier. Fabrication and sensing applications of multilayer polymer optical waveguides. *Procedia Technology*, 15:517–523, 2016.

[16] S. Frisken. Light-induced optical waveguide uptapers. *Opt. Lett.*, 18:1035–1037, 1993.

[17] A. Kewitsch, and A. Yariv. "Self-focusing and self-trapping of optical beams upon photopolymerization. *Opt. Lett.*, 21:24–26, 1996.

[18] T.M. Monro, L. Poladian, and C.M. De Sterke. Analysis of self-written waveguides in photopolymers and photosensitive materials. *Phys. Rev. E*, 57:1104–1113, 1998.

[19] H. Li, Y. Dong, P. Xu, Y. Qi, C. Guo, and J. Sheridan. Beam self-cleanup by use of self-written waveguide generated by photopolymerization. *Opt. Lett.*, 40:2981–2984, 2015.

[20] T. Yoshimura, D. Takeda, T. Sato, Y. Kinugasa and H. Nawata. Polymer waveguides self-organized by two-photon photochemistry for self-aligned optical couplings with wide misalignment tolerances. *Opt. Communications*, 362:81–86, 2015.

[21] K.Dorkenoo, O.Crégut, L.Mager, F.Gillot, C.Carre, and A.Fort. Quasi-solitonic behavior of self-written waveguides created by photopolymerization. *Opt. Lett.*, 27:1782–1784, 2002.

[22] A.A. Sukhorukov, S. Shoji, Y.S. Kivshar. Self-written waveguides in photosensitive materials. *Journal of Nonlinear Optical Physics & Materials*, 11:391–407, 2002.

[23] K.D. Dorkenoo, F. Gillot, O. Cregut, Y. Sonnefraud, A. Fort, and H. Leblond. Control of the refractive index in photopolymerizable materials for (2 + 1) d solitary wave guide formation. *Phys. Rev. Lett.*, 93:143905(4), 2004.

[24] H. Ma, A.K.-Y. Jenn, and L.R. Dalton. *Polymer-Based Optical Waveguides: Materials, Processing, and Devices.* Adv. Mater.

[25] H. Kim, and S. Yoo. Large mode area inverse index fiber with a graded index profile for high power single mode operation. *Opt. Express*, 25:21935–21946, 2017.

[26] B.E.A. Saleh and M.C. Teich. *Fundamentals of Photonics, 2nd ed.* Wiley, 2007.

[27] R. Paschotta. *Field Guide to Lasers.* WA: SPIE Press, 2008. ISBN: 9780819469618.

[28] S.K. Selvaraja, and P. Sethi. *Review on Optical Waveguides in Emerging Waveguide Technology.* IntechOpen, London, 2018.

[29] F. Agulló-López, J. M. Cabrera, F. Agulló-Rueda. Electrooptics and Integrated Optics. *Electrooptics, Academic Press*, pages 219–249, 1994.

[30] Yogesh B. Gianchandani, Osamu Tabata, and Hans Zappe. 3.05 - Integrated Optics. *Comprehensive Microsystems, Elsevier*, pages 165–199, 2008.

[31] O. Ziemann, J. Krauser, P. E. Zamzow, and W. Daum. *POF Handbook Optical Short Range Transmission Systems*. Springer-Verlag Berlin Heidelberg, 2008.

[32] K. Okamoto. *Fundamentals of Optical Waveguides (Second Edition)*. Academic Press, 2006.

[33] G. Z. Mashanovich, G. T. Reed, B. D. Timotijevic, and S. P. Chan. *Silicon Photonic Waveguides*. John Wiley Sons, Ltd, 2008.

[34] SY. Gang. Polymer based optical waveguides. master's degree thesis, universiti teknologi malaysia, johor bahru, 2005.

[35] JP. Donohoe. Ece 3323 electromagnetics ii, mississippi state university,[online]. `http://www.ece.msstate.edu/~donohoe/`.

[36] G. Zimmerl. *Electromagnetic Field Theory*, fachhochschule frankfurt am main
. `https://www.frankfurt-university.de/fileadmin/standard/Hochschule/Fachbereich_2/Labore/Hoechstfrequenztechnik/Electromagnetic_Field_Theory.pdf`.

[37] N. Litchinitser and V. Iakhnine. *Optical waveguides: numerical modeling*, 2012. http://optical-waveguides-modeling.net.

[38] M. Koshiba. *Optical Waveguide Theory by the Finite Element Method*. Springer Netherlands, 1992.

[39] N. Kassim, A. Mohammad, A. Supaat, M. Ibrahim and S. Gang. Polymer material for optical devices application. *RF and Microwave Conference (IEEE Cat. No.04EX924)*, pages 277–280, 2004.

[40] R. G. Hunsperger. *Integrated Optics: Theory and Technology*. Springer-Verlag Berlin Heidelberg, 1984.

[41] L. A. Eldada. Advances in telecom and datacom optical components. *Optical Engg.*, pages 1165–1178, 2001.

[42] C. Jang and R. Chen. Polymer-Based 1×6 Thermooptic Switch Incorporating an Elliptic TIR Waveguide Mirror. *J. Lightwave Technol.*, 21:1053–, 2003.

[43] R. Hauffe, U. Siebel, J. Bruns, and K. Petemann. Digital Optical Circuit Switches and Switching Matrices in Polymers. *Photonics Technol. Lett.*, 55:305–312, 2001.

[44] S. Ahn, W. Steier, Y. Kuo, M. Oh, H. Lee, C. Zhang, and H. Fetterman. Integration of electro-optic polymer modulators with low-loss fluorinated polymer waveguides. *Opt. Lett.*, 27:2109–2111, 2002.

[45] M. Suar, M. Rahlves, E. Reithmeier, and B. Roth. Numerical investigations on polymer-based bent couplers. *J. Opt. Soc. Am. B*, 35:1896–1904, 2018.

[46] M. Suar, O. Melchert, M. Rahlves, and B. Roth. Experimental and theoretical study of the formation process of photopolymer based self-written waveguides. *Opt. Express*, 27:38326–38336, 2019.

[47] Y. Noh, C. Lee, J. Kim, W. Hwang, Y. Won, H. Lee, S. Han, and M. Oh. Polymer waveguide variable optical attenuator and its reliability. *Opt. Commun.*, 242:533–540, 2004.

[48] Y. Lu, H. Guo, H. Wang, and S. Chi. Polymer-based S-shaped waveguide VOA for applications in the broadband DWDM network. *Microw Opt Techn Lett*, 39:1–4, 2003.

[49] C. Ma, H. Zhang, Da. Zhang, Z. Cui, and S. Liu. Effects of trapezoid core cross-sections on transmission characteristics of polymer arrayed waveguide grating multiplexers. *Opt. Commun.*, 241:321–331, 2004.

[50] N. Keil, H. Yao, C. Zawadzki. Athermal polarisation-independent arrayed-waveguide grating (AWG) multiplexer using an all-polymer approach. *Appl. Phys. B*, 73:619–622, 2001.

[51] M. Rahlves, A. Günther, M. Rezem, and B. Roth. Polymer-based transmission path for communication and sensing applications. *J. Light. Technol.*, 37:729–735, 2008.

[52] D. de Felipe, M. Kleinert, C. Zawadzki, A. Polatynski, G. Irmscher, W. Brinker, M. Moehrle, H. Bach, N. Keil, and M. Schell. Recent developments in polymer-based photonic components for disruptive capacity upgrade in data centers. *Journal of Lightwave Technology*, 35(4):683–689, 2017.

[53] M. Rezem, A. Günther, M. Rahlves, B. Roth, and E. Reithmeier. Hot embossing of polymer optical waveguides for sensing applications. *Procedia Technol.*, 15:514–520, 2014.

[54] M. Rezem, A. Günther, B. Roth, E. Reithmeier, and M. Rahlves. Low-cost fabrication of all-polymer components for integrated photonics. *J. Lightwave Technol*, 35:299–308, 2017.

[55] R. Horvath, H. C Pedersen, N. Skivesen, C. Svanberg, N. B Larsen. Fabrication of reverse symmetry polymer waveguide sensor chips on nanoporous substrates using dip-floating. *J. Micromech. Microeng.*, 15:1260–4, 2005.

[56] C. Kelb, W. Pätzold, U. Morgner, M. Rahlves, E. Reithmeier, and B. Roth. Characterization of femtosecond laser written gratings in PMMA using a phase-retrieval approach. *Opt. Mater. Express.*, 6:3202–3209, 2016.

[57] M. Kihara, M. Matsumoto, T. Haibara, and S. Tomita. Characteristics of thermally expanded core fiber. *Journal of Lightwave Technology*, pages 2209–2214, 1996.

[58] A. Tagaya, Y. Koike. Compensation and control of the birefringence of polymers for photonics. *Polym J.*, pages 306–314, 2012.

[59] R. A. Norwood, R. Gao, J. Sharma, and C. Teng. Sources of loss in single-mode polymer optical waveguides. *Proc. SPIE - The International Society for Optical Engineering*, pages 19–28, 2001.

[60] C. T. Sullivan, B. L. Booth, and A. Husain. Polymeric waveguides. *IEEE Circuits and Devices Magazine*, pages 27–31, 1992.

[61] L. Eldada. Advances in polymeric integrated optical componentry. *OSA Trends in Optics and Photonics Series*, 2001.

[62] L. Shacklette, R. Blomquist, J. Deng, P. Ferm, M. Maxfield, J. Mato, P. Jiang, K. Killian, K. Beeson, and H. Zou. Polymer Waveguides and Device Applications. *Optical Fiber Communication Conference, OSA*, 2003.

[63] O. Kashin, E. Tolstik, V. Matusevich, and R. Kowarschik. Numerical investigation of the (1+1)d self-trapping of laser beams in polymeric films based on polymethylmethacrylate and phenanthrenequinone. *J. Opt. Soc. Am. B*, 26:2152–2156, 2009.

[64] R. Malallah, I. Muniraj, H. Li, D. Cassidy and J. Sheridan. Interactions of two counter-propagating waveguides in the dry photopolymer material using fiber optics. *Frontiers in Optics*, pages JTh2A–146, 2016.

[65] A. Günther, S. Schneider, M. Rezem, Y. Wang, U. Gleissner, T. Hanemann, L. Overmeyer, E. Reithmeier, M. Rahlves, and B. Roth. Automated misalignment compensating interconnects based on self-written waveguides. *J. Lightwave Technol.*, 35:2678–2684, 2017.

[66] Ginés Lifante Pedrola. *Beam Propagation Method for Design of Optical Waveguide Devices.* John Wiley & Sons, 2015.

[67] M. Feit, and J. Fleck. Calculation of dispersion in graded-index multimode fibers by a propagating-beam method. *Appl. Opt.*, 18:2843–2851, 1979.

[68] W. Huang, C. Xu, S. Chu, S.K. Chaudhuri. The finite-difference vector beam propagation method:analysis and assessment. *Journal of Lightwave Technology*, 10:295–305, 1992.

[69] E. Montanari, S. Selleri, L. Vincetti, M. Zoboli. Finite-element full-vectorial propagation analysis for three-dimensional z-varying optical waveguides. *J. Lightwave Technol*, 16:703–714, 1998.

[70] M. Koshiba K. Saitoh. Full-vectorial finite element beam propagation method with perfectly matched layers for anisotropic optical waveguides. *J. Lightwave Technol.*, 19:405, 2001.

[71] W. Huang, C. Xu, S. Chu, S.K. Chaudhuri. A full-vectorial beam propagation method for anisotropic waveguides. *J. Lightwave Technol.*, 12:1926–1931, 1994.

[72] G. R. Hadley. Transparent boundary condition for the beam propagation method. *IEEE Journal of Quantum Electronics*, 28(1):363–370, 1992.

[73] P. Hertel. Dielectric waveguides, lectures delivered at teda applied physics school, nankai university, tianjin, prc, 2009.

[74] W.S.Brocklesby, S.J.Field, D.C. Hanna, A.C.Large, J.R.Lincoln, D.P.Shepherd, A.C.Trooper, P.J.Chandler, P.D.Townsend, L.Zhang, X.Q.Feng, and Q.Hu. Optically written waveguides in ion implanted Bi4Ge3O12. *Opt. Mat.*, 1:177–184.

[75] A.M.Ljungstrom, and T.M.Monro. Light-induced self-writing effects in bulk chalcogenide glass. *J. Lightwave Technol.*, 20:78–85, 2002.

[76] A. Günther, A. Petermann, U. Gleissner, T. Hanemann, E. Reithmeier, M. Rahlves, M. Meinhardt-Wollweber, U. Morgner, and B. Roth. Cladded self-written multimode step-index waveguides using a one-polymer approach. *Opt. Letter*, 40:1830–1833, 2015.

[77] H.Li, Y.Qi, R.Malallah, J.P.Ryle, and J.T.Sheridan. Self-trapping of optical beams in a self-written channel in a solid bulk photopolymer material. *Proc.SPIE*, 9508:9508–7, 2015.

[78] H. Li, Y. Qi, J. Ryle and J. Sheridan. Self-written waveguides in a dry acrylamide/polyvinyl alcohol photopolymer material. *Appl. Opt.*, 53:8086–8094, 2014.

[79] G.Zhao, and P. Mouroulis. Diffusion model of hologram formation in dry photopolymer materials. *J. of Modern Opt.*, 41:1929–1939, 1994.

[80] D. Engin, A. S. Kewitsch, and A. Yariv. Holographic characterization of chain photopolymerization. *J. Opt. Soc. Am. B*, 16:1213–1219, 1999.

[81] M. Ben Belgacem, S. Kamoun, M. Gargouri, K. Honorat Dorkenoo, A. Barsella, and L. Mager. Light induced self-written waveguides interactions in photopolymer media. *Opt. Express*, 23:20841–20848, 2015.

[82] W. Heller. Remarks on refractive index mixture rules. *The J. Physical Chemistry*, 69:1123–1129, 1965.

[83] T. Babeva, I. Naydenova, D. Mackey, S. Martin, and V. Toal. Two-way diffusion model for short-exposure holographic grating formation in acrylamide-based photopolymer. *J. Opt. Soc. Am. B*, 27:197–203, 2010.

[84] T. Babeva, D. Mackey, I. Naydenova, S. Martin, V. Toal. Study of the photoinduced surface relief modulation in photopolymers caused by illumination with a gaussian beam of light. *J. of Opt.*, 12:124011, 2010.

[85] S.Gallego, A.Márquez, M.Ortuño, J.Francés, S. Marini, A.Beléndez, and I.Pascual. Surface relief model for photopolymers without cover plating. *Opt. Express*, 19:10896–10906, 2011.

[86] M. Suar, M. Rahlves, E. Reithmeier, and B. Rothl. Simulation of straight and bent self-written waveguides in photopolymer mixture using phenomenological and diffusion models. *Proc.SPIE*, 10690, 2018.

[87] N. Lindenmann, G. Balthasar, D. Hillerkuss, R. Schmogrow, M. Jordan, J. Leuthold, W. Freude, and C. Koos. Photonic wire bonding: a novel concept for chip-scale interconnects. *Opt. Express*, 20:17667–17677, 2012.

[88] J. Missinne, S. Beri, M. Dash, S. Samal, P. Dubruel, J. Watté, and G. Van Steenbergee. Curing kinetics of step-index and graded-index single mode polymer self-written waveguides. *Opt. Mater. Express*, 4:1324–1335, 2014.

[89] M. Kagami, T. Yamashita, M. Yonemura, and A. Kawasaki. Light-Induced self-written optical waveguides. *IEICE Trans Electron*, E90-C:1061–1070, 2007.

[90] N. Ioannides, E. B. Chunga, A. Bachmatiuk, I. Gonzalez-Martinez, B. Trzebicka, D. B. Adebimpe, D. Kalymnios, M. Rümmeli. Approaches to mitigate polymer-core loss in plastic optical fibers: a review. *Materials Research Express*, pages 2053–1591, 2014.

[91] J. Missinne, S. Beri, M. Dash, S. Samal, P. Dubruel, J. Watté, and G. Van Steenberge. Curing kinetics of step-index and graded-index single mode polymer self-written waveguides. *Opt. Mater. Express.*, 4:1324–1335, 2004.

[92] S. G. Lee, B.H.O, S.G. Park, K. H. Kim1, J. K. Kang, Y. W. Choi. Integration of Polymer-based Optical Waveguide Arrays and Micro/Nano-Photonic Devices for Optical Printed Circuit Board (O-PCB) Application. *Proc. of SPIE. (Optoelectronic Integrated Circuits VII)*, pages 118–129, 2005.

[93] H. Li, Y. Qi, R. Malallah, and J. Sheridan. Modeling the Nonlinear Photoabsorptive Behavior during Self-Written Waveguide Formation in a Photopolymer. *J. Opt. Soc. Am. B*, 32:912–922, 2015.

[94] Z. Zhang, P. Zhao, P. Lin, and F. Sun. Thermo-optic coefficients of polymers for optical waveguide applications. *Polymer*, 47:4893–4896, 2006.

[95] R. Hauffe, and K. Petermann. *Thermo-optic switching Optical Switching ed T S El-Bawab.* Boston, MA: Springer, 2006.

[96] S. N. Kasarova, N. G. Sultanova, I. D. Nikolov. Temperature dependence of refractive characteristics of optical plastics. *J. Phys.: Conf. Ser.*, 253:012018, 2010.

[97] M. Rahman, and M. Hossain. Thermal performance analysis of polymer optical waveguides for thermo-optic applications. *International Forum on Strategic Technology (IFOST)*, pages 65–68, 2014.

[98] A. Liu, Z. Zhang, D. Liu, N. Keil, and N. Grote . Thermo-optic simulations of silicon nitride / polymer hybrid waveguides. *Proc. SPIE 8781, Integrated Optics: Physics and Simulations*, page 878105, 2013.

[99] R. Aronow et al. Multiple Scale Modeling for Predictive Material Deformation Analysis. *Mathematics and Statistics Newsletter, University of Massachusetts Amherst*, 33:4–6, 2017-2018.

[100] J. Shewchuk. Triangle: Engineering a 2D Quality Mesh Generator and Delaunay Triangulator. *Applied Computational Geometry: Towards Geometric Engineering*, 1148:203–222, 1970.

[101] Abu Samah. Design and fabrication of a polymer based directional coupler thermooptic switch. *PhD thesis, University Teknologi Malaysia, Faculty of Electrical Engineering*, 2004.

[102] M. Suar, M. Bharan, A. Günther, and B. Roth. Combined thermomechanical and optical simulations of planar-optical polymer waveguides. *Journal of Optics*, 22:125801 (9pp), 2020.

[103] M. Diemeer, J. Brons, and E. Trommel. Polymeric optical waveguide switch using the thermooptic effect. *J. of Light. Technol.*, 7:449–453, 1989.

[104] M. Dixit, V. Mathur, S. Gupta, M. Baboo, K. Sharma, and N. Saxena. Morphology, miscibility and mechanical properties of PMMA/PC blends. *Phase Transit. Multinational J.*, 82:866–878, 2009.

[105] M. Rahlves, M. Rezem, A. Günther, C. Kelb, M. Khan, E. Reithmeierb, B. Roth. Towards fabrication and application of polymer based photonics networks and sensors. *SPIE OPTO*, pages 1054502–1, 2018.

[106] Y. Sun, Y. Cao, Y. Yi, L. Tian, Y. Zheng, J. Zheng, F. Wang and D. Zhang. A low-power consumption MZI thermal optical switch with a graphene-assisted heating layer and air trench. *RSC Adv.*, pages 39922–39927, 2017.

Publications originating from this thesis

[A1] *Numerical investigations on polymer-based bent couplers*, M. Suar M. Rahlves, E. Reithmeier and B. Roth, Journal of the Optical Society of America B **35**, 1896-1904 (2018), DOI:10.1364/JOSAB.35.001896.

[A2] *Experimental and theoretical study of the formation process of photopolymer based self-written waveguides*, M. Suar, O. Melchert, M. Rahlves, and B. Roth, Optics Express **27**, 38326-38336 (2019), DOI:10.1364/OE.27.038326.

[A3] *Combined thermomechanical and optical simulations of planar-optical polymer waveguides*, M. Suar, M. Bharan, A. Günther, and B. Roth, Journal of Optics **22**, 125801(9pp) (2020), DOI:10.1088/2040-8986/abc087.

Proceeding contributions originating from this thesis

[P1] *Simulation of straight and bent self-written waveguides in photopolymer mixture using phenomenological and diffusion models*, M. Suar, M. Rahlves, E. Reithmeier and B. Roth, Proc. SPIE 10690, 106900D (2018), DOI:10.1117/12.2312507.

Conference contributions originating from this thesis

[P1] *Simulation of straight and bent self-written waveguides in photopolymer mixture using phenomenological and diffusion models*, M. Suar, M. Rahlves, E. Reithmeier and B. Roth, SPIE Optical Systems Design, Frankfurt, Germany (2018) (Talk)

[T2] *Numerical Investigations on Polymer-Based Optical Waveguide Couplers*, M. Suar, M. Rahlves, E. Reithmeier, P. Wriggers, B. Roth, RCM - Research Challenges in Mechanics, Hannover (2019) (Poster)

[T3] *Multi-physics simulation and experimental validation of self written polymer-optical waveguide formation*, M. Suar, O. Melchert, M. Rahlves, and B. Roth, Internationales Symposium "Future Optics", Hannover (2019) (Poster)

[T4] *Hymnos(Project 2): Optical simulation of self written waveguides*, M. Suar, M. Rahlves, and B. Roth, Hymnos Symposium, PZH (Produktionstechnisches Zentrum Hannover), Hannover (2018) (Talk)

Curriculum Vitae

2021 - present	Data Scientist (Home Office) at Schwarz-Group. Neckarsulm, Germany
2017 - 2020	Doctoral student and research fellow at the Hanover Centre for Optical Technology. Leibniz University Hanover. Hanover, Germany.
2015 - 2016	Student Assistant at Theoretical Electrical Engineering at Paderborn University. Paderborn, Germany.
2013 - 2016	Master of Science in Electrical System Engineering at Paderborn University. Paderborn, Germany
2012 -2013	Software Analyst at Xerox, India.
2010-2012	Software Engineer at HCL Technologies Ltd, India
2006-2010	Bachelor of Technology in Electrical Engineering at KIIT University, India
2005	Completed Schooling from Central School, Kharagpur, India